POLISH ACADEMY OF SCIENCES

THERMODYNAMICS AND COMBUSTION COMMITTEE

archives of thermodynamics

Wydawnictwo IMP
Gdańsk

QUARTERLY
Vol. 37
2016
No. 3

Editorial Office

Archives of Thermodynamics
The Szewalski Institute of Fluid Flow Machinery, Fiszera 14, 80-231 Gdańsk, Poland, Tel.: (+48) 58-341-12-71 int. 141, E-mail: redakcja@imp.gda.pl
http://www.imp.gda.pl/archives-of-thermodynamics/
http://at.czasopisma.pan.pl/

Publication funding of this journal is provided by resources of the Polish Academy of Sciences and the Szewalski Institute of Fluid-Flow Machinery PASci

Terms of subscription outside Poland
Annual subscription rate outside Poland (2016) is 120 EUR. Price of single issue is 30 EUR. Back of previously published volumes are available on request. Subscription orders should be sent directly to **IMP PAN Publishers, The Szewalski Institute of Fluid-Flow Machinery PASci, ul. Fiszera 14, 80-231 Gdansk, Poland**; fax: (+48) 58-341-61-44; e-mail: now@imp.gda.pl. Payments should be transferred to the bank account of IMP PAN: IBAN 28 1130 1121 0006 5498 9520 0011 at Bank Gospodarstwa Krajowego; Code SWIFT: GOSKPLPW

Warunki prenumeraty w Polsce
Roczna prenumerata (2016 r.) wynosi 168 PLN. Cena pojedynczego numeru wynosi 42 PLN. Osiągalne są również wydania archiwalne. Zamówienia z określeniem okresu prenumeraty, nazwiskiem i adresem odbiorcy należy kierować bezpośrednio do Wydawcy (Instytut Maszyn Przepływowych im. R. Szewalskiego PAN, ul. Fiszera 14, 80-231 Gdańsk, Aleksandra Nowaczewska, e-mail: now@imp.gda.pl). Wpłaty prosimy kierować na konto Instytutu Maszyn Przepływowych PAN nr 28 1130 1121 0006 5498 9520 0011 w Banku Gospodarstwa Krajowego

Articles in *Archives of Thermodynamics* are abstracted and indexed within:

Applied Mechanics Reviews • BazTech • Arianta • Baidu Scholar • Cabell's Directory • Celdes • Chemical Abstracts Service (CAS) - CAplus • CNKI Scholar (China National Knowledge Infrastucture) • CNPIEC • DOAJ • EBSCO (relevant databases) • EBSCO Discovery Service • Elsevier - SCOPUS • Genamics JournalSeek • Google Scholar • Inspec • Index Copernicus • J-Gate • Journal TOCs • Naviga (Softweco) • Paperbase • Pirabase • POL-index • Polymer Library • Primo Central (ExLibris) • ProQuest (relevant databases) • ReadCube • Referativnyi Zhurnal (VINITI) • SCImago (SJR) • Summon (Serials Solutions/ProQuest) • TDOne (TDNet) • TEMA Technik und Management • Ulrich's Periodicals Directory/ulrichsweb • WorldCat (OCLC)

Online ISSN 2083-6023
DE GRUYTER – http://www.degruyter.com/view/j/aoter

Typeset in LaTeX

archives
of thermodynamics
Vol. **37**(2016), No. 3, 3–18
DOI: 10.1515/aoter-2016-0016

Effect of hall currents on thermal instability of dusty couple stress fluid

AMRISH KUMAR AGGARWAL*
ANUSHRI VERMA

Department of Mathematics, Jaypee Institute of Information Technology, A-10, Sector-62, Noida (UP) - 201307, India

Abstract In this paper, effect of Hall currents on the thermal instability of couple-stress fluid permeated with dust particles has been considered. Following the linearized stability theory and normal mode analysis, the dispersion relation is obtained. For the case of stationary convection, dust particles and Hall currents are found to have destabilizing effect while couple stresses have stabilizing effect on the system. Magnetic field induced by Hall currents has stabilizing/destabilizing effect under certain conditions. It is found that due to the presence of Hall currents (hence magnetic field), oscillatory modes are produced which were non-existent in their absence.

Keywords: Couple-stress fluid; Dust particles; Hall currents; Stationary convection; Oscillatory modes; Magnetic field

Nomenclature

C	–	concentration of the fluid
C_{pt}	–	heat capacity of particles, $\mathrm{J\,kg^{-1}K^{-1}}$
C_v	–	heat capacity of fluid at constant volume, $\mathrm{J\,kg^{-1}K^{-1}}$
D	–	derivative with respect to z $(= d/dz)$
d	–	depth of layer, m
e	–	charge of an electron
F	–	couple-stress parameter $(= \mu'/\rho d^2)$
i	–	imaginary unit
$\vec{g}(0, 0, -g)$	–	gravity field, $\mathrm{m\,s^{-2}}$
g	–	gravitational acceleration, $\mathrm{m\,s^{-2}}$

*Corresponding Author. E-mail: amrish.aggarwal@jiit.ac.in

$\vec{H}\,(0,0,H)$	–	magnetic field, G
$\vec{h}(h_x,h_y,h_z)$	–	perturbation in magnetic field
K	–	Stokes' drag coefficient, $\mathrm{kg\,s^{-1}}$
k	–	wave number, $\mathrm{m^{-1}}$
k_T	–	thermal diffusivity, $\mathrm{m^2 s^{-1}}$
k_x, k_y	–	components of wave number k along x-axis, y-axis, $\mathrm{m^{-1}}$
M	–	Hall current parameter $= (H/4\pi N' e\eta)$
m	–	mass of single particle, kg
N	–	perturbation in suspended particle number density N_0
N_0	–	suspended particles number density
N'_0	–	electron number density
n	–	growth rate, $\mathrm{s^{-1}}$
p	–	pressure, Pa
Pr_1	–	Prandtl number
Pr_m	–	magnetic Prandtl number
Q	–	Chandrasekhar number $(= \mu_e H^2 d^2/4\pi\rho_0\nu\eta)$
$\vec{q}(u,v,w)$	–	velocity of fluid with components u, v, w, $\mathrm{m\,s^{-1}}$
$\vec{q}_d\,(l,r,s)$	–	velocity of suspended particles with components l, r, s, $\mathrm{m\,s^{-1}}$
R	–	Rayleigh number $(= g\alpha\beta d^4/\nu\kappa)$
R_1	–	modified Rayleigh number
T	–	temperature, K
t	–	time, s
x	–	dimensionless wave number
$\vec{x}\,(x,y,z)$	–	space coordinate
x,y,z	–	Cartesian coordinates

Greek symbols

α	–	coefficient of thermal expansion, $\mathrm{K^{-1}}$
β	–	uniform temperature gradient, $\mathrm{K\,m^{-1}}$
η	–	electrical resistivity, $\mathrm{m^2 s^{-1}}$
η'	–	suspended particle radius, m
δp	–	perturbation in pressure
$\delta\rho$	–	perturbation in density
θ	–	perturbation in temperature, K
μ	–	dynamic viscosity, $\mathrm{kg\,m^{-1} s^{-1}}$
μ'	–	couple-stress viscosity
μ_e	–	magnetic permeability
ν	–	kinematic viscosity, $\mathrm{m^2 s^{-1}}$
ν'	–	kinematic viscoelasticity, $\mathrm{m^2 s^{-1}}$
ρ	–	fluid density, $\mathrm{kg\,m^{-3}}$
ζ	–	z component of vorticity
η	–	z electrical resistivity
ξ	–	z component of current density
∇	–	nabla operator

Subscripts and superscripts

d – upper surface
0 – botom surface
$*$ – complex conjugate

1 Introduction

Chandrasekhar [1] has given the theory of Benard convection in a viscous, Newtonian fluid layer heated from below. Chandra [2] observed that in an air layer, convection occur at much lower gradients than predicted if the layer depth was less than 7 mm, and called this motion, 'Columnar instability'. However, for layers deeper than 10 mm, a Benard type cellular convection was observed. Thus, there is a contradiction between the theory and the experiment. The use of Boussinesq approximation has been made through out which states that the density changes are disregarded in all other terms in the equation of motion except the external force term. Sharma [3] has considered the effect of rotation and magnetic field on the thermal instability in compressible fluids. The fluid has been considered to be Newtonian in all the above studies while Scanlon and Segel [4] have considered the effect of suspended particles on the onset of Benard convection and found that the critical Rayleigh number was reduced solely because of the heat capacity of the pure fluid.

With the growing importance of non-Newtonian fluids in modern technology and industries, the investigations on such fluids are desirable. The theory of couple-stress fluids is proposed by Stokes' [5]. One of the applications of the couple-stress fluid is its use to the study of the mechanism of lubrication of synovial joints, which has become the object of scientific research. A human joint is a dynamically loaded bearing which has articular cartilage as the bearing and synovial fluid as the lubricant. When a fluid film is generated, squeeze film action is capable of providing considerable protection to the cartilage surface. The shoulder, knee, hip and ankle joints are the loaded bearing synovial joints of the human body and these joints have a low friction coefficient and negligible wear. Normal synovial fluid is clear or yellowish and is a viscous, non-Newtonian fluid. According to the theory of Stokes [5], couple stresses are found to appear in noticeable magnitude in fluids with very large molecules. Since the long chain hylauronic acid molecules are found as additives in synovial fluid. Walicki and Walicka [6] modeled synovial fluid as a couple-stress fluids in human joints. Goel *et. al.* [7] has studied the hydromagnetic stability of

an unbounded couple stress binary fluid mixture having vertical temperature and concentration gradients with rotation. An electrically conducting couple-stress fluid heated from below in a porous medium in the presence of uniform horizontal magnetic field has also been submitted by Sharma and Sharma [8]. The use of magnetic field is being made for the clinically purposes in detection and cure of certain diseases with the help of magnetic field devices/instruments. The problem of a couple-stress fluid heated from below in a porous medium is considered by Sharma and Sharma [9] and Sharma and Thakur [10].

Recent space craft observations have confirmed that the dust particles play a significant role in the dynamics of the atmosphere as well as in the diurnal and surface variations in the temperature of the Martian weather. Further, environmental pollution is the main cause of dust to enter the human body. The metal dust which filters into the blood stream of those working near furnace causes extensive damage to the chromosomes and genetic mutation so observed are likely to breed cancer as malformations in the coming progeny. Therefore, it is very essential to study the blood flow with dust particles. Considering blood as couple-stress fluid and dust particles as microorganisms, Rathod and Thippeswamy [11] have studied the gravity flow of pulsatile blood through closed regular inclined channel with microorganisms. Sunil *et. al.* [12] have studied the effect of suspended particles on couple-stress fluid heated and soluted from below in a porous medium and found that suspended particles have destabilizing effect on the system.

If an electric field is applied at right angles to the magnetic field, the whole currents will not flow along the electric field. The tendency of electric current to flow across an electric field in the presence of magnetic field is called Hall effect. The Hall currents are likely to be important in flows of laboratory plasmas as well as in many geophysical and astrophysical situations. Sharma and Sharma [13] have studied the effect of suspended particles on couple-stress fluid heated from below in the presence of rotation and magnetic field. Gupta [14] has seen the effect of Hall currents on the thermal instability of electrically conducting fluid in the presence of uniform vertical magnetic field.

Singh and Dixit [15] have studied the effect of Hall currents on the thermal instability of a compressible couple-stress fluid with suspended particles while Kumar and Kumar [16] have seen the combined effect of dust particles, magnetic field and rotation on a couple-stress fluid heated from below.

Aggarwal and Makhija [17] have studied the combined effect of magnetic field and rotation on couple-stress fluid heated from below in the presence of suspended particles. The effect of suspended particles, magnetic field and rotation on the thermal stability of a ferromagnetic fluid has been studied by Aggarwal and Verma [18]. The effect of compressibility and suspended particles on thermal convection in Walters' B' elastico-viscous fluid in hydromagnetics has been considered by Sharma and Aggarwal [19]. Postrzednik [20] has studied the influence of the heat transfer on the specific thermal capacity of the flowing compressible fluid. The unsteady natural convection in micropolar nanofluids has been studied by Rup and Nering [21].

In this paper, the effect of Hall currents on thermal instability of couple-stress fluid in the presence of dust particles is considered.

2 Mathematical formulation

Consider a static state in which an incompressible, Stokes' [5] couple-stress fluid layer of thickness d heated from below so that a uniform temperature and density at the bottom surface $z = 0$, are T_0, ρ_0, respectively, and at the upper surface $z = d$, are T_d, ρ_d, and a uniform adverse temperature gradient $\beta = \left|\frac{dT}{dz}\right|$ is maintained and the layer is acted upon by the gravity field $\vec{g}(0, 0, -g)$ and uniform magnetic field $\vec{H}\,(0, 0, H)$.

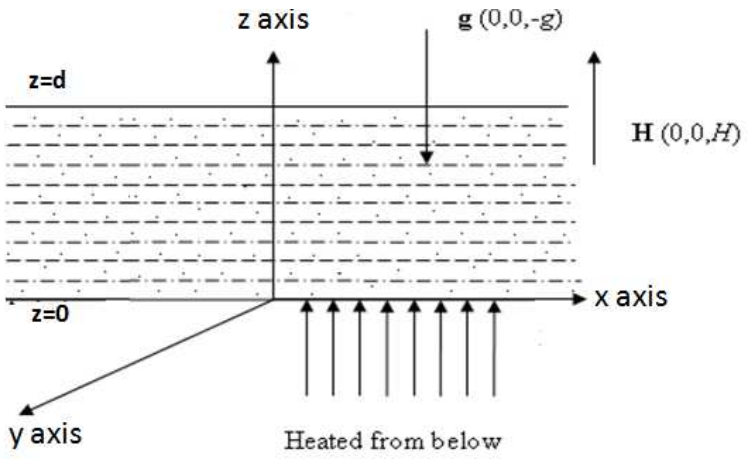

Figure 1: Schematic sketch of the problem studied.

Let p, ρ, T, α, ν, μ', μ_e, k_T, and $\vec{q}(u,v,w)$ denote respectively pressure, density, temperature, coefficient of thermal expansion, kinematic viscosity, couple-stress viscosity, magnetic permeability, thermal diffusivity and fluid velocity. $\vec{q}_d\,(l,r,s)$ and N_0 denote the velocity and number density of suspended particles, respectively. $K = 6\pi\mu\eta'$, where η' is the particle radius, is a constant and $\vec{x} = (x,y,z)$. Then the equation of motion and continuity of couple-stress fluid are

$$\begin{aligned}\frac{\partial \vec{q}}{\partial t} &= -\frac{1}{\rho_0}\nabla p + \vec{g}\alpha\theta - \left(\nu - \frac{\mu'}{\rho_0}\nabla^2\right)\vec{q} \\ &\quad + \frac{KN_0}{\rho_0}\left(\vec{q}_d - \vec{q}\right) + \frac{\mu_e}{4\pi\rho_0}\left[\left(\nabla\times\vec{h}\right)\times\vec{H}\right]\,, \end{aligned} \tag{1}$$

$$\nabla\cdot\vec{q} = 0\,. \tag{2}$$

Assuming uniform particles size, spherical shape and small relative velocities between the fluid and particles, the presence of particles adds an extra force term, in the equation of motion (1), proportional to the velocity difference between particles and fluid. Since the force exerted by the fluid on the particles is equal and opposite to that exerted by the particles on the fluid, there must be an extra force term, equal in magnitude but opposite in sign, in the equations of motion for the particles. The distances between particles are assumed to be so large compared with their diameter that interparticle reactions need not be accounted for. The effect of pressure, gravity and magnetic field on suspended particles, assuming large distances apart, are negligibly small and therefore ignored. If mN is the mass of the particles per unit volume, then the equations of motion and continuity for the particles, under the above assumptions, are

$$mN_0\frac{\partial \vec{q}_d}{\partial t} = KN_0\left(\vec{q} - \vec{q}_d\right)\,, \tag{3}$$

$$\frac{\partial N}{\partial t} + \nabla\cdot\left(N\vec{q}_d\right) = 0\,. \tag{4}$$

Let C_v and C_{pt} denote the heat capacity of fluid at constant volume and heat capacity of the particles, respectively. Assuming that the particles and the fluid are in thermal equilibrium, the equation of energy yields

$$\frac{\partial T}{\partial t} + \frac{mNC_{pt}}{\rho_0 C_v}\left(\frac{\partial}{\partial t} + \vec{q}_d\cdot\nabla\right)T = k_T\nabla^2 T\,. \tag{5}$$

The kinematic viscosity, ν, couple-stress viscosity, μ', thermal diffusivity, k_T, and coefficient of thermal expansion, α, are all assumed to be constants. The Maxwell's equations in the presence of Hall currents yield

$$\frac{\partial \vec{h}}{\partial t} = \nabla \times \left(\vec{q} \times \vec{H}\right) + \eta \nabla^2 \vec{h} - \frac{C}{4\pi N' e} \nabla \times \left[\left(\nabla \times \vec{h}\right) \times \vec{H}\right] , \tag{6}$$

$$\nabla \cdot \vec{h} = 0 , \tag{7}$$

where η, N', and e stands for the electrical resistivity, electron number density, and the charge of an electron, respectively.

The equation of state for the fluid can be express as

$$\rho = \rho_0 \left[1 - \alpha \left(T - T_0\right)\right] . \tag{8}$$

The basic motionless solution is

$$\begin{aligned} \vec{q} = (0,0,0) \ , \quad \vec{q}_d = (0,0,0) \ , \quad T = T_0 - \beta z \ , \\ \rho = \rho_0 \left(1 + \alpha \beta \, z\right) \ , \quad N = N_0 = \text{const.} \end{aligned} \tag{9}$$

Assume small perturbations around the basic solution and let δp, $\delta \rho$, θ, $\vec{h}(h_x, h_y, h_z)$, $\vec{q}(u, v, w)$, and $\vec{q}_d\,(l, r, s)$ denote, respectively, the perturbations in fluid pressure, p, density, ρ, temperature, T, magnetic field, $\vec{H}(0, 0, H)$, fluid velocity, $(0, 0, 0)$, and suspended particles velocity, $(0, 0, 0)$. The change in density $\delta\rho$ caused mainly by the perturbation θ in temperature is given by

$$\delta \rho = -\alpha \rho_0 \theta \, . \tag{10}$$

Then the linearized perturbation equations of couple-stress fluid become

$$\begin{aligned} \frac{\partial \vec{q}}{\partial t} = -\frac{1}{\rho_0} \nabla \delta p + \overrightarrow{g} \alpha \theta - \left(\nu - \frac{\mu'}{\rho_0} \nabla^2\right) \vec{q} \\ + \frac{K N_0}{\rho_0} \left(\vec{q}_d - \vec{q}\right) + \frac{\mu_e}{4\pi \rho_0} \left[\left(\nabla \times \vec{h}\right) \times \vec{H}\right] , \end{aligned} \tag{11}$$

$$\nabla \cdot \vec{q} = 0 , \tag{12}$$

$$m N_0 \frac{\partial \vec{q}_d}{\partial t} = K N_0 \left(\vec{q} - \vec{q}_d\right) \ , \tag{13}$$

$$\left(1 + h_1\right) \frac{\partial \theta}{\partial t} = \beta \left(w + h_1 s\right) + \kappa \nabla^2 \theta \, , \tag{14}$$

$$\nabla \cdot \vec{h} = 0 , \tag{15}$$

$$\frac{\partial \vec{h}}{\partial t} = \nabla \times \left(\vec{q} \times \vec{H}\right) + \eta \nabla^2 \vec{h} - \frac{C}{4\pi N' e} \nabla \times \left[\left(\nabla \times \vec{h}\right) \times \vec{H}\right] , \tag{16}$$

where $\kappa = \frac{q}{\rho_0 C_v}$ and $h_1 = \frac{mN_0 C_{pt}}{\rho_0 C_v}$.

Eliminating $\vec{q}_d$ in Eq. (11) using Eq. (13) as dusty particles velocity is not very slow ($(q - q_d)$ is not very large) and writing the scalar components of resulting equations and eliminating $u,\ v,\ h_x,\ h_y$, and δp between them, by using Eqs. (12) and (15), we obtain

$$\left(\frac{m}{K}\frac{\partial}{\partial t} + 1\right)\left[\frac{\partial}{\partial t}\nabla^2 w - g\alpha\left(\frac{\partial^2 \theta}{\partial x^2} + \frac{\partial^2 \theta}{\partial y^2}\right) - \frac{\mu_e H}{4\pi\rho_0}\frac{\partial}{\partial z}\nabla^2 h_z\right] + \frac{mN_0}{\rho_0}\frac{\partial}{\partial t}\nabla^2 w$$
$$= \left(\frac{m}{K}\frac{\partial}{\partial t} + 1\right)\left(\nu - \frac{\mu'}{\rho_0}\nabla^2\right)\nabla^2 w , \tag{17}$$

$$\left\{\frac{\partial}{\partial t}\left[1 + \frac{mN_0}{\rho_0\left(\frac{m}{k}\frac{\partial}{\partial t} + 1\right)}\right] - \left(\nu - \frac{\mu'}{\rho_0}\nabla^2\right)\right\}\zeta = \frac{\mu_e H}{4\pi\rho_0}\frac{\partial \xi}{\partial z} , \tag{18}$$

$$\left(H_1\frac{\partial}{\partial t} - \kappa\nabla^2\right)\theta = \beta\left(\frac{m}{k}\frac{\partial}{\partial t} + H_1\right) w , \tag{19}$$

$$\left(\frac{\partial}{\partial t} - \eta\nabla^2\right) h_z = H\frac{\partial w}{\partial z} - \frac{CH}{4\pi N' e}\frac{\partial \xi}{\partial z} , \tag{20}$$

$$\left(\frac{\partial}{\partial t} - \eta\nabla^2\right)\xi = H\frac{\partial}{\partial z}\zeta + \frac{CH}{4\pi N' e}\frac{\partial}{\partial z}h_z , \tag{21}$$

where $H_1 = 1 + h_1$, $\zeta = \frac{\partial v}{\partial x} - \frac{\partial u}{\partial y}$ is z-component of vorticity and $\xi = \frac{\partial h_y}{\partial x} - \frac{\partial h_x}{\partial y}$ is z-component of current density.

3 Normal mode analysis

Analyzing the disturbances into normal modes and assume that the perturbation quantities are of the form

$$[w, h_z, \theta, \zeta, \xi] = \left[W(z), K(z), \Theta(z), Z(z), X(z)\right] \exp\left(ik_x x + ik_y y + nt\right) , \tag{22}$$

where k_x, k_y are wave numbers along x and y directions, respectively, $k = \sqrt{(k_x^2 + k_y^2)}$ is the resultant wave number of the disturbances and n

is the growth rate, $W(z)$, $K(z)$, $\Theta(z)$, $Z(z)$, $X(z)$ are defined by Chandrasekhar [1].

Using expression (22), Eqs. (17)–(20) in nondimensional form become

$$\left[\sigma' + F\left(D^2 - a^2\right) - 1\right]\left(D^2 - a^2\right) W = -\frac{g\alpha a^2 d^2}{\nu}\Theta + \frac{\mu_e H d}{4\pi\rho_0\nu}\left(D^2 - a^2\right) DK \,, \tag{23}$$

$$\left\{\sigma' - d^2\left[1 - F\left(D^2 - a^2\right)\right]\right\} Z = \frac{\mu_e H d}{4\pi\rho_0\nu} DX \,, \tag{24}$$

$$\left(D^2 - a^2 - H_1 \mathrm{Pr}_1\sigma\right)\Theta = \frac{\beta d^2}{\kappa}\left(H_1 + \frac{\tau_1\nu}{\kappa}\sigma\right) W \,, \tag{25}$$

$$\left(D^2 - a^2 - \mathrm{Pr}_m\sigma\right) K = -\frac{Hd}{\eta} DW + \frac{cHd}{4\pi N' e\eta} DX \,, \tag{26}$$

$$\left(D^2 - a^2 - \mathrm{Pr}_m\sigma\right) X = -\frac{Hd}{\eta} DZ + \frac{cH}{4\pi N' e\eta d}\left(D^2 - a^2\right) DK \,, \tag{27}$$

where we have nondimensionalized various parameters as follows:

$$a = kd, \quad \sigma = \frac{nd^2}{\nu}, \quad \tau_1 = \frac{\tau\nu}{d^2}, \quad \mathrm{Pr}_1 = \frac{\nu}{\kappa}, \quad \mathrm{Pr}_m = \frac{\nu}{\eta}, \quad D = \frac{d}{dz},$$

$$F = \frac{\mu'}{\nu\rho_0 d^2}, \quad \sigma' = \frac{n' d^2}{\nu}, \quad H_1 = 1 + h_1, \quad n' = n\left(1 + \frac{mN_0 K/\rho_0}{mn + K}\right).$$

After eliminating Θ, Z, X, and K from Eqs. (23)–(27), we obtain

$$\left\{\left[\sigma' - d^2\left[1 - F(D^2 - a^2)\right]\right\}(D^2 - a^2) W + \frac{\mathrm{R}a^2}{(D^2 - a^2 - H_1\mathrm{Pr}_1\sigma}\left(H_1 + \frac{\tau_1\nu}{\kappa}\sigma\right) W + \mathrm{Q}\left[\frac{(D^2 - a^2 - \mathrm{Pr}_m\sigma)\left\{\left[\sigma' - d^2 1 - F(D^2 - a^2)\right]\right\} + \mathrm{Q}D^2}{(D^2 - a^2 - \mathrm{Pr}_m\sigma)^2\left\{\sigma' - d^2\left[1 - F(D^2 - a^2)\right]\right\} + \mathrm{Q}(D^2 - a^2 - \mathrm{Pr}_m\sigma) D^2}\right.$$
$$\left. - \mathrm{M}\left\{\sigma' - d^2\left[1 - F(D^2 - a^2)\right]\right\}(D^2 - a^2) D^2\right] DW = 0 \,, \tag{28}$$

where $\mathrm{Q} = \frac{\mu_e H^2 d^2}{4\pi\rho_0\nu\eta}$ is Chandrasekhar number, $\mathrm{R} = \frac{g\alpha\beta d^4}{\nu\kappa}$ is thermal Rayleigh number, and $\mathrm{M} = \left(\frac{H}{4\pi N' e\eta}\right)$ is the nondimensional number accounting for Hall currents.

Consider the case in which both the boundaries are free, the medium adjoining the fluid is perfectly conducting and temperatures at the boundaries are kept fixed. The boundary conditions, appropriate for the problem, are

$$W = 0\,, Z = 0\,, \Theta = 0 \text{ and } D^2W = 0\,, D^4W = 0 \text{ at } z = 0 \text{ and } z = 1. \quad (29)$$

The proper solution of Eq. (29) characterizing the lowest mode is

$$W = W_0 \sin \pi\, z\ , \quad (30)$$

where W_0 is a constant. Substituting the proper solution, Eq. (30), in Eq. (28), we obtain the dispersion relation

$$\begin{aligned}
&\frac{R_1 x}{(1+x+iH_1 \mathrm{Pr}_1\sigma_1)}\left(H_1+\frac{\tau_1 v}{\kappa}\sigma\right)\\
&= Q_1\Bigg[\frac{(1+x+i\mathrm{Pr}_m\sigma_1)\left\{i\sigma'+[1+F_1(1+x)]\right\}+Q_1}{(1+x+i\mathrm{Pr}_m\sigma)^2\left\{i\sigma'+[1+F_1(1+x)]\right\}+Q_1(1+x+i\mathrm{Pr}_m\sigma_1)}\\
&- M\big\{i\sigma'+[1+F_1(1+x)]\big\}(1+x)-\big\{i\sigma'+[1+F_1(1+x)]\big\}(1+x)\Bigg]\ , \quad (31)
\end{aligned}$$

where: $R_1 = \frac{\mathrm{R}}{\pi^4}$, $i\sigma_1 = \frac{\sigma}{\pi^2}$, $Q_1 = \frac{Q}{\pi^2}$, and $F_1 = \pi^2 F$.

4 Stationary convection

At stationary convection, when the instability sets, the marginal state will be characterized by $\sigma = 0$. Thus, putting $\sigma = 0$ in Eq. (31), we get

$$\begin{aligned}
R_1 = \frac{Q_1}{xH_1}&\left[\frac{(1+x)\left[1+F_1\left(1+x\right)\right]+Q_1}{(1+x)\left[1+F_1\left(1+x\right)\right]+Q_1-\mathrm{M}\left[1+F_1\left(1+x\right)\right]}\right]\\
&+\frac{(1+x)^2\left[1+F_1\left(1+x\right)\right]}{xH_1}\ . \quad (32)
\end{aligned}$$

The above relation expresses the modified Rayleigh number R_1 as a function of the parameters Q_1, H_1, F_1, M, and dimensionless wave number x. To study the effect of magnetic field, dust particles, couple stresses and Hall currents, we examine the nature of $\frac{dR_1}{dQ_1}$, $\frac{dR_1}{dH_1}$, $\frac{dR_1}{dF_1}$, and $\frac{dR_1}{dM}$ analytically. Equation (32) gives:

$$\begin{aligned}
\frac{dR_1}{dQ_1} = \frac{1}{xH_1}&\left[\frac{(1+x)\left[1+F_1\left(1+x\right)\right]+Q_1}{(1+x)\left[1+F_1\left(1+x\right)\right]+Q_1-\mathrm{M}\left[1+F_1\left(1+x\right)\right]}\right]\\
&-\frac{1}{xH_1}\frac{\mathrm{M}Q_1\left[1+F_1\left(1+x\right)\right]}{\left\{(1+x)\left[1+F_1\left(1+x\right)\right]+Q_1-\mathrm{M}\left[1+F_1\left(1+x\right)\right]\right\}^2}\ , \quad (33)
\end{aligned}$$

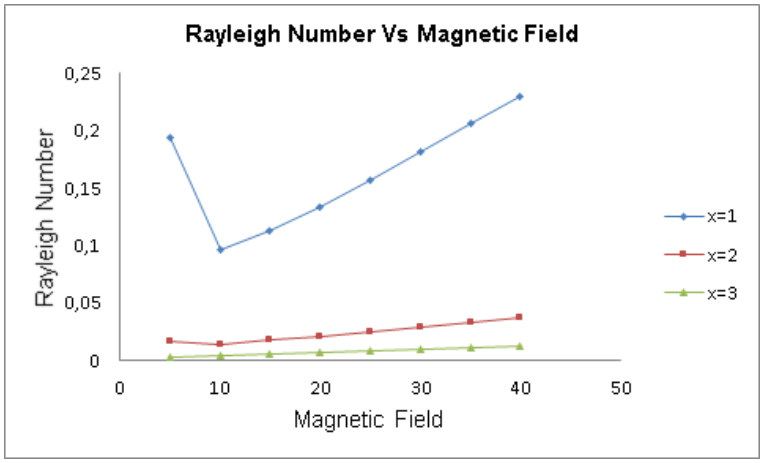

Figure 2: Variation of Rayleigh number, R_1, and magnetic field, Q_1, for a fixed $H_1 = 0.1$, $F_1 = 0.1$, M $= 6$ for different values of wave numbers and magnetic field parameter.

which shows that magnetic field has a stabilizing or destabilizing effect according to $(1+x)\,[1+F_1\,(1+x)]+Q_1$ is greater or less than $\mathrm{M}\,[1+F_1\,(1+x)]$. This result, illustrated in Fig. 2, is in agreement with the result obtained by Aggarwal and Makhija [17], Kumar and Kumar [16].

$$\frac{dR_1}{dH_1} = -\frac{Q_1}{xH_1^2}\left\{\frac{(1+x)\,[1+F_1\,(1+x)]+Q_1}{(1+x)\,[1+F_1\,(1+x)]+Q_1-\mathrm{M}\,[1+F_1\,(1+x)]}\right\} - \frac{(1+x)^2\,[1+F_1\,(1+x)]}{xH_1^2}\,, \tag{34}$$

which clearly shows that dust particles have destabilizing effect on thermal instability in a couple-stress fluid. This result is also evident from Fig. 3 and is same as observed by Aggarwal and Makhija [17], Kumar and Kumar [16].

$$\frac{dR_1}{dF_1} = \frac{Q_1\,(1+x)}{xH_1} \times\left\{(1+x)\left[(1+x)\,[1+F_1\,(1+x)]+Q_1-\mathrm{M}\,[1+F_1\,(1+x)]\right] - \frac{\Big[(1+x)\,[1+F_1\,(1+x)]+Q_1\Big]\Big[1+x-\mathrm{M}\Big]}{\Big[(1+x)\,[1+F_1\,(1+x)]+Q_1-\mathrm{M}\,[1+F_1\,(1+x)]\Big]^2}+1\right\}. \tag{35}$$

From Eq. (35), it follows that couple stresses have stabilizing effect on the system which is clear from Fig. 4.

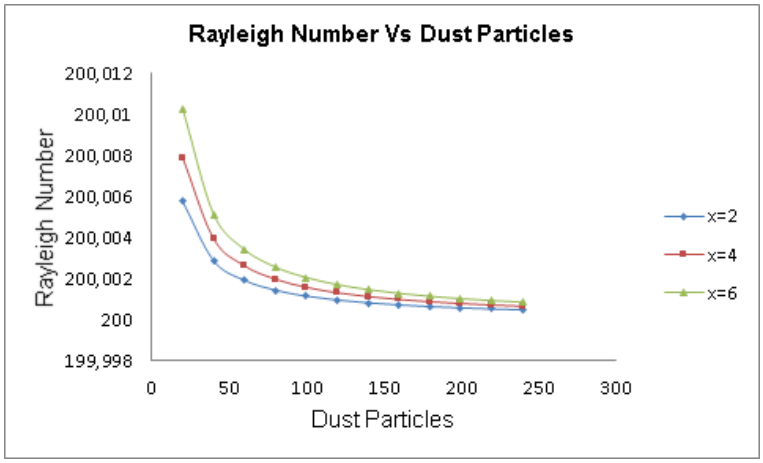

Figure 3: Variation of Rayleigh number, R_1, and dust particles, H_1, for a fixed $Q_1 = 1$, $F_1 = 1$, M $= 10$ for different values of wave numbers and dust particle parameters.

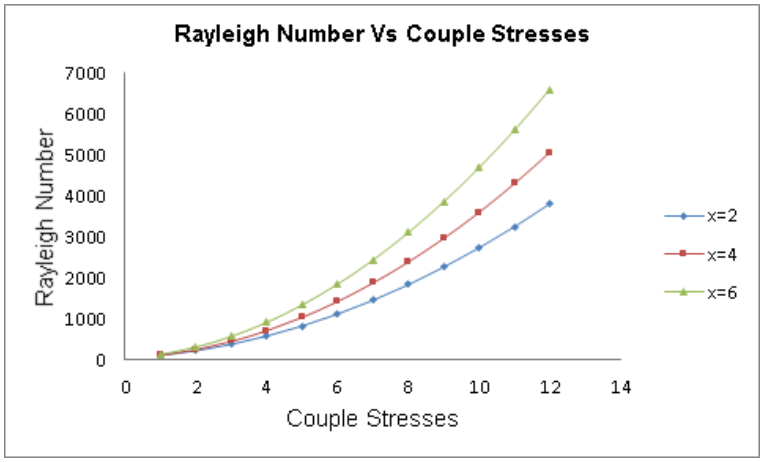

Figure 4: Variation of Rayleigh number, R_1, and couple stresses, F_1, for a fixed $Q_1 = 5$, $H_1 = 1$, M $= 1$ for different values of wave number and couple stresses.

$$\frac{dR_1}{dM} = -\frac{Q_1}{xH_1}\left\{\frac{\left[\,(1+x)\,[1+F_1\,(1+x)]+Q_1\right][1+F_1\,(1+x)\,]}{\left[\,(1+x)\,[1+F_1\,(1+x)]+Q_1-\mathrm{M}\,[1+F_1\,(1+x)]\,\right]^2}\right\}. \tag{36}$$

From Eq. (36) can be observed that Hall currents have destabilizing effect on the system which is in agreement with Fig. 5. This result is same as obtained by Singh and Dixit [15]. The reason for destabilizing effect of Hall currents is accounted by Chandrasekhar [1].

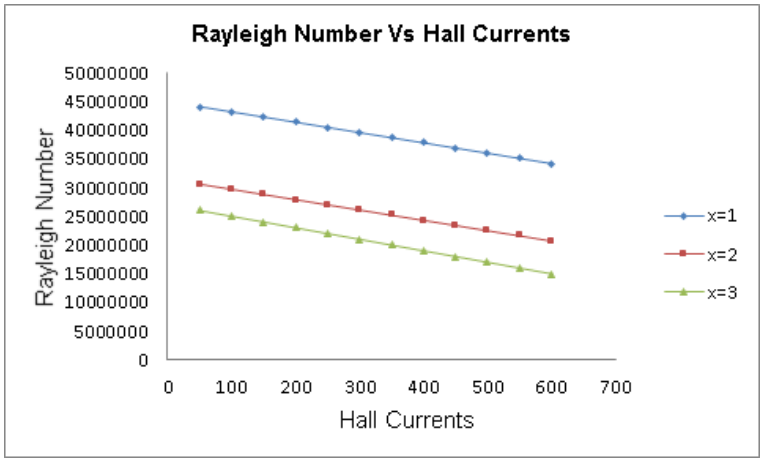

Figure 5: Variation of Rayleigh number, R_1 and Hall currents, M for a fixed $Q_1 = 3000$, $H_1 = 1$, $F_1 = 1$ for different values of wave number and Hall currents.

5 Stability of the system and oscillatory modes

To determine under what conditions the principle of exchange of stabilities (PES) is satisfied (i.e., σ is real and the marginal states are characterized by $\sigma = 0$) and oscillations come into play, we multiply Eq. (23) with W^* (complex conjugate of W) and integrate over the range of $z$and making use of Eqs. (24)–(27) together with the boundary conditions (29) and then we get

$$\begin{aligned}(1-\sigma')\,I_1 - FI_2 + \frac{g\alpha\kappa a^2}{\beta\nu}\left(H_1 + \frac{\tau_1\nu}{\kappa}\sigma^*\right)^{-1}(I_3 + H_1\mathrm{Pr}_1\sigma^* I_4) \\ -\frac{\mu_e\eta}{4\pi\rho_0\nu}\,(I_5 + \mathrm{Pr}_m\sigma^* I_6) + \frac{\mu_e\eta d^2}{4\pi\rho_0\nu}\,(I_7 + \mathrm{Pr}_m\sigma^* I_8) \\ + d^2\left[\,(\sigma'-1)\,I_9 - FI_{10}\right] \;=\; 0\,, \end{aligned} \tag{37}$$

where:

$$I_1 = \int \left(|DW|^2 + a^2 |W|^2\right) dz \,, \qquad I_2 = \int \left(\left|D^2 W\right|^2 + 2a^2 |DW|^2 + a^4 |W|^2\right) dz \,,$$
$$I_3 = \int \left(|D\Theta|^2 + a^2 |\Theta|^2\right) dz \,, \qquad I_4 = \int |\Theta|^2 \, dz \,,$$
$$I_5 = \int \left(\left|D^2 K\right|^2 + 2a^2 |DK|^2 + a^4 |K|^2\right) dz \,, \qquad I_6 = \int \left(|DK|^2 + a^2 |K|^2\right) dz \,,$$
$$I_7 = \int \left(|DX|^2 + a^2 |X|^2\right) dz \,, \qquad I_8 = \int |X|^2 \, dz \,,$$
$$I_9 = \int |Z|^2 \, dz \,, \qquad I_{10} = \int \left(|DZ|^2 + a^2 |Z|^2\right) dz \,,$$

and σ^* is complex conjugate of σ. The integrals $I_1 - I_{10}$ are all positive definite. Putting $\sigma = i\sigma_i \, (\sigma^* = -i\sigma_i)$ in Eq. (37) and equating imaginary parts, we obtain

$$\sigma_i \left[I_1 + \frac{g\alpha\kappa^2 a^2}{\beta\tau_1 \nu^2} I_3 + \frac{g\alpha\kappa a^2}{\beta\nu} \mathrm{Pr}_1 I_4 - \frac{\mu_e \eta}{4\pi\rho_0 \nu} \mathrm{Pr}_m I_6 + \frac{\mu_e \eta d^2}{4\pi\rho_0 \nu} \mathrm{Pr}_m I_8 - d^2 I_9 \right] = 0 \,. \tag{38}$$

It is clear from Eq. (38) that σ_i (growth rate parameter) may be zero or nonzero, which implies that modes may be nonoscillatory or oscillatory. In the absence of magnetic field (hence Hall currents) and dust particles, Eq.(38) reduces to

$$\sigma_i \left[I_1 + \frac{g\alpha\kappa^2 a^2}{\beta\tau_1 \nu^2} I_3 + \frac{g\alpha\kappa a^2}{\beta\nu} \mathrm{Pr}_1 I_4 + \frac{\mu_e \eta d^2}{4\pi\rho_0 \nu} \mathrm{Pr}_m I_8 \right] = 0 \,. \tag{39}$$

The terms in the bracket are positive definite. Thus $\sigma_i = 0$ which means that the oscillatory modes are not allowed and the principle of exchange of stabilities is satisfied in the absence of magnetic field (hence Hall currents) and dust particles.

6 Conclusions

In this paper, the effect of Hall currents and dust particles has been considered on the thermal instability of a couple-stress fluid. The effect of various parameters such as magnetic field, dust particles, couple-stresses and Hall currents has been investigated analytically as well as graphically. The principal conclusions from the analysis are:

1. In order to investigate the effects of magnetic field, dust particles, couple-stresses and Hall currents, we examine the behaviour of $\frac{dR_1}{dQ_1}$, $\frac{dR_1}{dH_1}$, $\frac{dR_1}{dF_1}$, and $\frac{dR_1}{dM}$ analytically.

2. It is found that magnetic field has a stabilizing or destabilizing effect according to $(1+x)\left[1+F_1\left(1+x\right)\right]+Q_1$ is greater or less than $\mathrm{M}\left[1+F_1\left(1+x\right)\right]$. This result is also verified from Fig. 2.
3. The dust particles and Hall currents have destabilizing effect on the system. The reason for destabilizing effect of Hall currents is accounted by Chandrasekhar [1].
4. The couple-stresses have stabilizing effect on the system.
5. The principle of exchange of stabilities is satisfied in the absence of magnetic field (hence Hall currents) and dust particles.

Received 5 June 2013

References

[1] Chandrasekhar S.: *Hydrodynamic and Hydromagnetic Stability*. Dover, New York 1981.

[2] Chandra K.: *Instability of fluid heated from below*. Proc. Roy. Soc. London. **164(A)** (1938), 231–258.

[3] Sharma R.C.: *Thermal instability in compressible fluids in the presence of rotation and magnetic field*. J. Math. Anal. Appl. **60**(1977), 1, 227–235.

[4] Scanlon J.W., Segel L.A.: *Some effects of suspended particles on the onset of Bénard convection*. Phys. Fluids. **16**(1973), 10, 573–578.

[5] Stokes V.K.: *Couple-stresses in fluids*. Phys. Fluids. **9**(1966), 9, 1709–1715.

[6] Walicki E., Walicka A.: *Inertia effecting the squeeze film of a couple-stress fluid in biological bearings*. Int. J. Appl. Mech. Engg. **4**(1999), 2, 363–373.

[7] Goel A.K., Agrawal S.C., Agrawal G.S.: *Hydromagnetic stability of an unbounded couple-stress binary fluid mixture having temperature and concentration gradients with rotation*. Indian J. Pure Appl. Math. **30**(1999), 10, 991–1001.

[8] Sharma R.C., Sharma S.: *On couple stress fluid heated from below in porous medium*. Indian J. Phys. **75B**(2001), 59–61.

[9] Sharma R.C., Sharma S.: *On electrically conducting couple stress fluid heated from below in porous medium in presence of uniform horizontal magnetic field*. Int. J. Appl. Mech. Engg. **6**(2001), 2, 251–263.

[10] Sharma R.C., Thakur D.: *On couple stress fluid heated from below in porous medium in hydromagnetics*. Czech. J. Phys. **50**(2000), 6, 753–758.

[11] Rathod V.P., Thippeswami G.: *Gravity flow of pulsatile blood through closed rectangular inclined channel with micro-organisms*. Math. Educ. **33**(1999), 1, 40–49.

[12] Sunil, Sharma R.C., Chandel R.S.: *Effect of suspended particles on couple stress fluid heated and soluted from below in porous medium*. J. Porous Media **7**(2004), 1, 9–18.

[13] Sharma R.C., Sharma M.: *Effect of suspended particles on couple stress fluid heated from below in the presence of rotation and magnetic field*. Indian J. Pure Appl. Math. **35**(2004), 8, 973–989.

[14] Gupta A.S.: *Hall effects on thermal instability*. Rev. Roum. Math. Pure Appl. **12**(1967), 665–677.

[15] Singh V., Dixit S.: *Hall effect on thermal instability of compressible couple stress fluid in presence of suspended particles*. Int. J. Math. Arch. **3**(2012), 4, 1701–1711.

[16] Kumar V., Kumar S.: *On a couple stress fluid heated from below in hydromagnetics*. Appl. Appl. Math. Inter. J. **5**(2010), 10, 1529–1542.

[17] Aggarwal A.K., Makhija S.: *Combined effect of magnetic field and rotation on couple-stress fluid heated from below in the presence of suspended particles*. Int. J. Appl. Mech. Engg. **16**(2011), 4, 931–942.

[18] Aggarwal A.K., Verma A.: *Effect of suspended particles, magnetic field and rotation on the thermal stability of a ferromagnetic fluid*. Int J. Appl. Mech. Engg. **17**(2012), 4, 1109–1122.

[19] Sharma R.C., Aggarwal A.K.: *Effect of compressibility and suspended particles on thermal convection in a Walters' B' elastico-viscous fluid in hydromagnetics*. Int J. Appl. Mech. Engg. **11**(2006), 2, 391–399.

[20] Postrzednik S.: *Influence of the heat transfer on the specific thermal capacity of the flowing compressible fluid*. Arch. Thermodyn. **25**(2004), 2, 95–106.

[21] Rup K., Nering K.: *Unsteady natural convection in micropolar nanofluids*. Arch. Thermodyn. **35**(2015), 3, 155–170, DOI: 10.2478/aoter-2014-0027.

archives
of thermodynamics
Vol. **37**(2016), No. 3, 19–29
DOI: 10.1515/aoter-2016-0017

Heat transfer in plate heat exchanger channels: Experimental validation of selected correlation equations

JANUSZ T. CIEŚLIŃSKI[a] *
ARTUR FIUK[b]
KRZYSZTOF TYPIŃSKI[b]
BARTŁOMIEJ SIEMIEŃCZUK[b]

[a] Gdańsk University of Technology, Narutowicza 11/12, 80-233 Gdańsk, Poland

[b] SECESPOL Ltd., Warszawska 50, 82-100 Nowy Dwór Gdański, Poland

Abstract This study is focused on experimental investigation of selected type of brazed plate heat exchanger (PHEx). The Wilson plot approach was applied in order to estimate heat transfer coefficients for the PHEx passages. The main aim of the paper was to experimentally check ability of several correlations published in the literature to predict heat transfer coefficients by comparison experimentally obtained data with appropriate predictions. The results obtained revealed that Hausen and Dittus-Boelter correlations underestimated heat transfer coefficient for the tested PHEx by an order of magnitude. The Aspen Plate code overestimated heat transfer coefficient by about 50%, while Muley-Manglik correlation overestimated it from 1% to 25%, dependent on the value of Reynolds number and hot or cold liquid side.

Keywords: PHEx; Wilson method; Correlations

Nomenclature

A	–	heat transfer area, m^2
c	–	specific heat, kJ/(kg K)
C	–	constant in the Wilson plot approach

*Corresponding Author. E-mail: jcieslin@pg.gda.pl

d – diameter, m
G – width of a plate, m
Gz – Graetz number
k – overall heat transfer coeffcient, W/(m^{2}K)
L – height of a plate, m
$\dot{m}$ – mass flow rate, kg/s
n – exponent in the Wilson plot approach
N – number of plates
Nu – Nusselt number
Pr – Prandtl number
$\dot{Q}$ – heat flow rate, W
Re – Reynolds number
s – distance between plates, m
t – temperature, °C
$\dot{V}$ – volume flow rate, m^3/s
w – velocity, m/s

Greek symbols

α – heat transfer coefficient, W/(m^{2}K)
β – chevron or corrugation angle, deg
δ – thickness of a plate, m
λ – thermal conductivity, W/(mK)
ρ – density, kg/m^3
η – dynamic viscosity, m Pa s
Δt – temperature difference, K

Subscripts

1 – hot fluid
2 – cold fluid
’ – inlet
” – outlet
exp – experimental
h – hydraulic
log – logarithmic
pl – plates
w – wall

1 Introduction

A plate heat exchanger (PHEx) is a compact heat exchanger which provides many advantages and unique application features. These include flexible thermal sizing, easy cleaning for sustaining hygienic conditions, achievement of close approach temperatures due to their pure counter flow operation, and enhanced heat transfer performance.

The brazed plate heat exchanger consists of a pack of pressed plates

brazed together, completely eliminating the use of gaskets, end frames, and bolts from the design. Instead, the plates are held together by brazing with copper under vacuum. This results in a much less complicated, lighter weight and more compact heat exchanger. Brazing of the corrugated, gasket-free plates together causes the two fluids to be directed through alternating channels between the plates. Their simple design also results in greatly reduced shipping and installation cost.

Apart from the above features, the brazed plate heat exchangers also have exceptional strength and durability. This is due to the fact that, in addition to sealing around the periphery of the plates, the internal contact points are also brazed together at thousands of contact points in each unit which admits them to operate at higher pressures and temperatures than gasketed units. The operating temperature of brazed heat exchangers ranges from $-195\,^{\circ}\mathrm{C}$ to $350\,^{\circ}\mathrm{C}$, and their maximum operating pressure is 4.5 MPa [1]. However, today's new testing methods allow brazed units to operate up to 6 MPa pressure conditions [2,3]. Recently, plate heat exchangers have found application in high temperature power system with solid oxide fuel cells [4].

The thermal-hydraulic performance of plate heat exchangers is strongly influenced by the plate surface corrugation patterns in the plate pack they are fitted with. Heat transfer plates are normally produced by stamping specially designed corrugations on the surface of thin metallic sheets. The corrugated plates used in plate heat exchangers can be manufactured from any metal or alloy that can be pressed, cold formed or welded.

When the plates are assembled in a stack, the corrugations on the adjoining plates form interrupted flow passages, and these intercorrugation flow paths promote enhanced convective heat transfer coefficients and decreased fouling characteristics. The corrugations also increase the effective surface area for heat transfer as well as plate rigidity, and the multiple metal-to-metal contact points between adjacent plates lend greater mechanical support to the stack.

The thermal-hydraulic design of plate heat exchangers is essentially similar to the general methodology employed for designing any other type of exchanger. The major design considerations may include:

- process/design or problem specifications;
- thermal and hydraulic design;
- mechanical/structural design, and operation and maintenance constraints;

- manufacturing considerations and cost;
- trade-off factors and system-based optimization.

Extensive effort has been made in the past to experimentally investigate the heat transfer characteristics of plate heat exchangers. Data have been published for different types of chevron, herringbone and wash board plate heat exchangers [5–8]. However, the heat transfer enhancement characteristics of plate heat exchangers could be fully utilized in the industrial applications only if accurate correlations are available for Nusselt number and frictional pressure drop with all the necessary details. Although several single phase heat transfer correlations are available in the literature on plate heat exchangers [6,9–10], lack of data is still a kind of barrier in the use of plate heat exchangers in industry.

This study is focused on experimental investigation of selected type of brazed plate heat exchanger. The Wilson plot approach was applied in order to estimate heat transfer coefficients for the PHEx passages. The main aim of the paper was to experimentally validate Hausen [11], Dittus-Boelter [11] and Muley-Manglik [5] correlations by comparison experimentally obtained heat transfer coefficients with appropriate predictions. Additionally, commercial Aspen Plate code was used to determine heat transfer coefficients inside the PHEx channels [12].

2 Experimental apparatus and procedure

2.1 Experimental facility

The test stand – shown in Fig. 1, consists of four main systems: tested PHEx, heating water loop, cooling water loop and data acquisition system. Heating water flow rate was measured by Coriolis mass flowmeter of the type MASS2100 having an accuracy of ±0.15% of the actual flow rate. Cooling water flow rates were controlled by a regulating valve and were measured by the Danfoss MAG 1100 magnetic flowmeter, which is accurate to ±0.25%. The average temperatures of the heating and cooling water at the inlets and outlets of the PHEx were measured using the Pt100 resistance temperature gauging device with an accuracy of ±0.1°C. The pressure drop of both cooling and heating water was measured by PELTRON of the type NPXD 1 pressure transducers accurate to ±0.3%. The volume flow rate of the cold water and hot water varied from 0.6 m^3/h to 1 m^3/h. The

temperature of the cold water and hot water varied from 40 °C to 64 °C and from 48 °C to 72 °C, respectively.

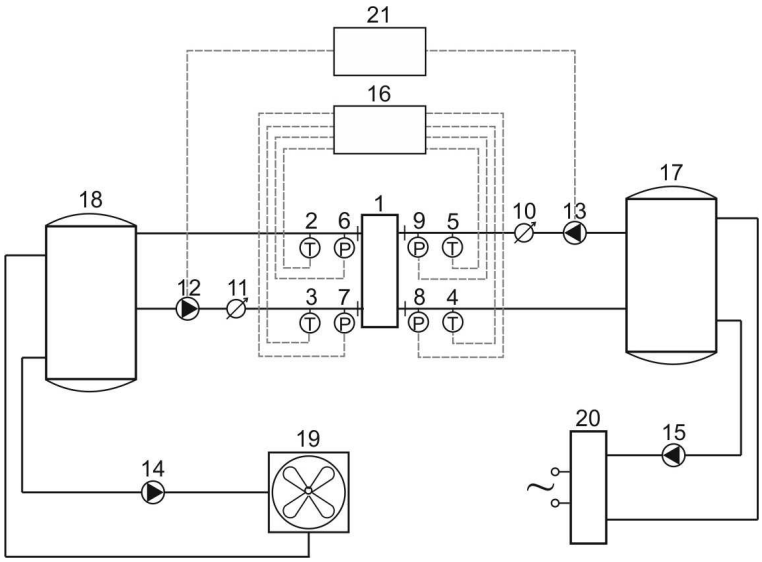

Figure 1: Scheme of the experimental setup: 1 – plate heat exchanger; 2,3,4,5 – thermoelements; 6,7,8,9 – pressure transducers; 10,11 – magnetic flowmeters; 12,13,14,15 – pumps; 16 – set of gauges; 17 – hot water tank; 18 – cold water tank; 19 – cooler; 20 – heating system; 21- set of inverters; T – thermoelement; P – pressure transducer.

2.2 Tested plate heat exchanger

Experiments were carried out using a brazed plate heat exchanger (Fig. 2) type LA22-20 with commercial chevron plates made of stainless steel with chevron angle, β, of 61° [13]. The characteristic dimensions of the plates were $0.08 \times 0.3 \times 0.0003$ m with the distance between the plates, δ, 0.002 m. The surface area of the tested PHEx was equal to $A = 0.418$ m^2 while the surface enlargement factor for all the plates was equal to 1.117. Plates were installed, providing two fluid streams in counter flow arrangement as shown in Fig. 2.

2.3 Wilson plot method

In order to estimate heat transfer coefficients on both sides of the wall separating fluid exchanging heat installation of thermocouples for measurement

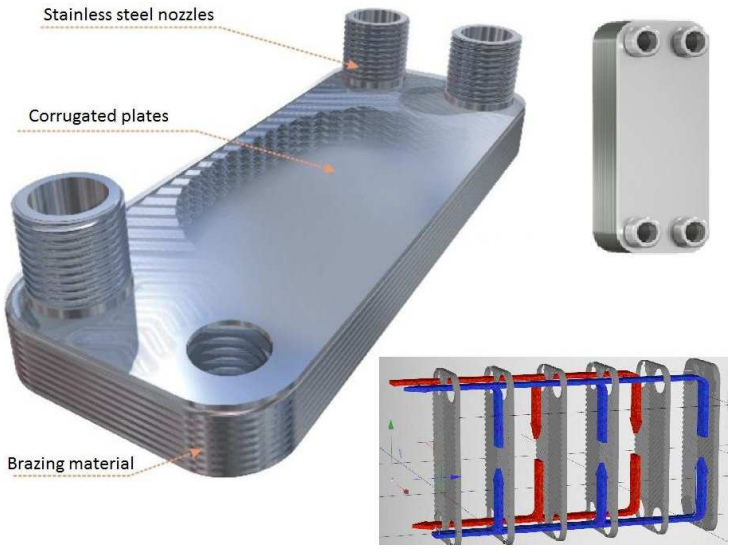

Figure 2: View of tested heat exchanger.

of wall temperature separating two fluids is required. If the recuperator has a complex geometry or as in present study is designed as a set of plates that are hermetically closed, then accurate measurement of the wall temperature faces significant difficulties. In such cases heat transfer coefficients can be predicted if the method due to Wilson plot is applied [14]. The method is simple and has a wide potential for applications of different types of heat exchangers [15–17]. The classical Wilson method, as well as its modifications, requires only determination of the overall resistance in the heat exchanger and hence an accurate energy balance, based on measurement of flow rates of fluids exchanging heat and their mean temperature at inlet and outlet from heat exchanger.

Assuming that the overall heat transfer coefficient is known and determined from the energy balance in the form

$$k_{\mathrm{exp}} = \frac{\dot{Q}}{A\Delta t_{\log}} \,, \tag{1}$$

where heat flow rate reads

$$\dot{Q}_1 = \dot{m}_1 c_1 \left(t_1^{'} - t_1^{''}\right) = \dot{Q}_2 = \dot{m}_2 c_2 \left(t_2^{''} - t_2^{'}\right) \,. \tag{2}$$

The logarithmic mean temperature difference is calculated as

$$\Delta t_{\log} = \frac{\left(t_1' - t_2''\right) - \left(t_1'' - t_2'\right)}{\ln \frac{\left(t_1' - t_2''\right)}{\left(t_1'' - t_2'\right)}} , \tag{3}$$

and mass flow rate is equal to

$$\dot{m}_1 = \rho_1 \dot{V}_1 , \quad \text{and} \quad \dot{m}_2 = \rho_2 \dot{V}_2 . \tag{4}$$

The heat transfer coefficients for $\dot{m}_1 = \text{const.}$ and $\dot{m}_2 = \text{var}$ can be calculated as

$$\alpha_1 = \text{const.}, \qquad \alpha_2 = C_2 w_2^{n_2} , \tag{5}$$

where α_1 and α_2 are heat transfer coefficients for hot and cold water at relevant mass flow rate, respectively, w_2 is the cold water velocity and n_2 – coefficient depending on the convective heat transfer regime. In the case of turbulent flow inside passages $n = 0.8$. For the case when $\dot{m}_1 = \text{var}$ and $\dot{m}_2 = \text{const.}$ heat transfer coefficients can be calculated as

$$\alpha_1 = C_1 w_1^n, \qquad \alpha_2 = \text{const} . \tag{6}$$

Constants C_1 and C_2 are determined using the linear regression method of the least squares method, where the squares of vertical distances between experimental points and a regression line are considered to find minimum value of squares. Knowledge of constants C_1 and C_2 enables determination, for the same series of investigations, of a one value of heat transfer coefficient α_1 as well as a sequence of values for the heat transfer coefficient α_2. The minimum value of the correlation coefficient was equal to 0.89514.

2.4 Methods of heat transfer coefficient calculation

In [9] two correlations have been proposed for calculation of an average heat transfer coefficient in PHEx passages:

- Hausen correlation

$$\text{Nu} = 3.66 + \frac{0.0668\text{Gz}}{1 + 0.04\text{Gz}^{2/3}} , \tag{7}$$

  where Graetz number is defined as

$$\text{Gz} = \text{RePr}\frac{d_h}{L} , \tag{8}$$

- Dittus-Boelter correlation

$$\mathrm{Nu} = 0.023\mathrm{Re}^{0.8}\mathrm{Pr}^{n} \,, \tag{9}$$

where exponent $n = 0.4$ for fluid heating and $n = 0.3$ for fluid cooling.

In this paper Muley and Manglik correlation [5]

$$\mathrm{Nu} = C\left(\beta\right)\left(\mathrm{Re}^{0.728+0.0543\sin[(2\pi\beta/90)+3.7]}\mathrm{Pr}^{1/3}\left(\eta/\eta_w\right)^{0.14}\right. \,, \tag{10}$$

where

$$C\left(\beta\right) = 0.2668 - 0.006967\beta + 7.244\times10^{-5}\beta^2 \tag{11}$$

was tested as well, where β represents chevron angle. Reynolds number is calculated as

$$\mathrm{Re} = \frac{wd_h\rho}{\eta} \,, \tag{12}$$

where hydraulic diameter $d_h = s_{pl}$, and s_{pl} is the distance between plates. Average velocity in PHEx passages reads

$$w = \frac{\dot{m}}{Gs_{pl}\rho N_z} \,, \tag{13}$$

where N_z is the number of cold or hot passages.

3 Results and discussion

Figure 3 shows the comparison of the average heat transfer coefficient for hot water passages, for the case when $\dot{m}_1$ = const. and $\dot{m}_2$ = var. It is seen in Fig. 3 that Hausen correlation and Dittus-Boelter correlation dramatically underpredict values of the average heat transfer coefficient, while the Aspen Plate code overestimates heat transfer coefficient by about 50%. Only Muley and Manglik correlation Eq. (10) predicts the heat transfer coefficient reasonably well. The discrepancy between the predictions and experimental results obtained by use of Wilson method does not exceed 10%.

Figure 4, in turn, shows the comparison of the average heat transfer coefficient for cold water passages, for the case when $\dot{m}_1$ = var and $\dot{m}_2$ = const. Similarly as for hot water side, Hausen and Dittus-Boelter correlations dramatically underpredict values of the average heat transfer coefficient – even by an order of magnitude, while the commercial Aspen Plate code overestimates heat transfer coefficient by about 10%. Again,

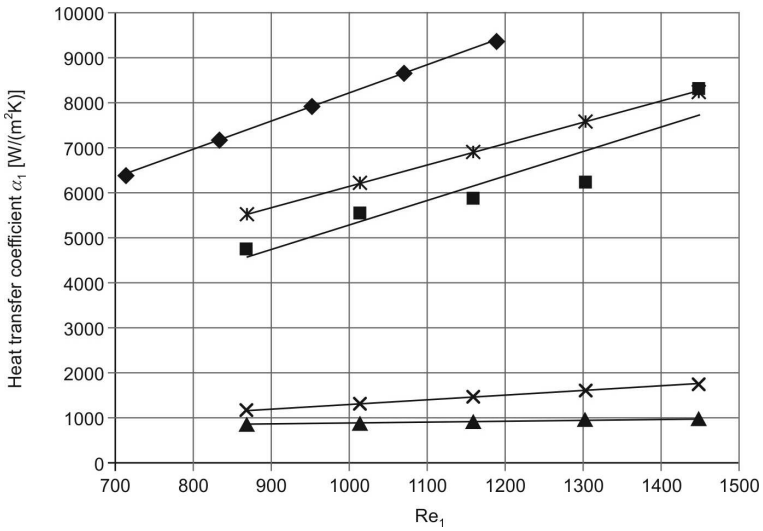

Figure 3: Hot water side heat transfer coefficient; ▲ – Eq. (7), x – Eq. (9), * – Eq. (10), ♦ – Aspen Plate code, ■ – Wilson approach.

only Muley and Manglik correlation Eq. (10) predicts the heat transfer coefficient reasonably well. The discrepancy between the predictions and experimental results obtained by use of Wilson method does not exceed 30%.

4 Conclusions

The study revealed that proper selection of the correlation equation for heat transfer coefficient estimation in hot and cold passages of the PHEx is of primary importance in correct choice of plate heat exchanger. Particularly:

- Hausen and Dittus-Boelter correlations are not recommended to be used in calculation of heat transfer coefficient in passages of PHEx. It is necessary to remember, that Hausen and Dittus-Boelter correlations have been originally developed for forced convection in straight smooth tubes. It is possible to use both correlations for channels with different cross sections using equivalent (hydraulic) diameter. However heat transfer in small passages between plates is enhanced by strong local turbulence resulting from corrugations. Therefore both correlations dramatically underestimate values of heat transfer coefficients in passages between corrugated plates.

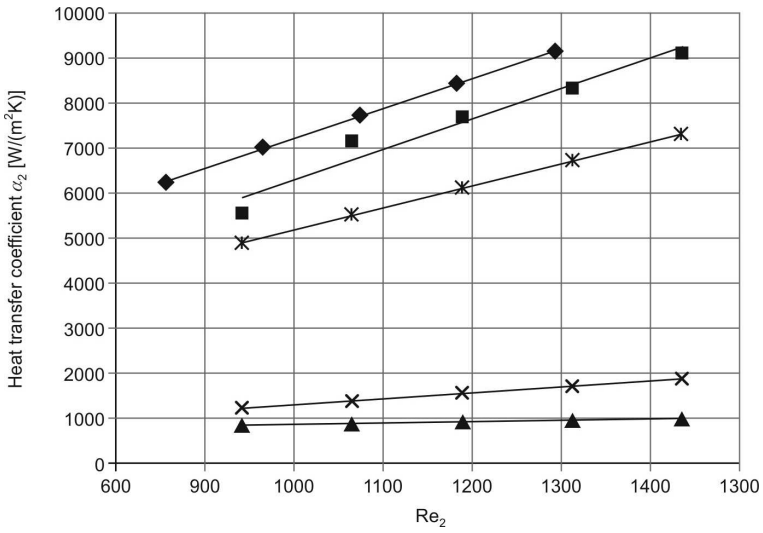

Figure 4: Cold water side heat transfer coefficient; ▲ – Eq. (7), x – Eq. 9), * – Eq. (10), ♦ – Aspen Plate code, ■ – Wilson approach.

- Present data show that in order to accurately estimate heat transfer coefficient in passages of PHEx, correlation equation specially dedicated for such sophisticated geometry should be applied. Particularly, such correlation equation should contain details of the plate geometry, like chevron or corrugation angle, corrugation depth, mean channel spacing or corrugation pitch.
- Wilson plot method seems to be a reliable tool in examination of plate heat exchangers.

Received 25 June 2015

References

[1] Wang L., Sunden B. and Manglik R.M.: *Plate Heat Exchangers: Design, Applications and Performance*. WIT Press, Southampton 2007.

[2] *Alfa Laval, Product Catalogue*, Sweden (http://www.alfalaval.com).

[3] *SWEP International, Product Catalogue*, Sweden (http://www.swep.net).

[4] Motyliński K., Kupecki J.: *Modeling the dynamic operation of a small fin plate heat exchanger – parametric analysis*. Arch. Thermodyn. **36**(2015), 3, 85–103, 2083-6023. DOI: 10.1515/aoter-2015-0023

[5] Mulley A., Manglik R.M.: *Enhanced thermal-hydraulic performance optimization of chevron plate heat exchangers*. Int. J. Heat Exchangers **1**(2000), 3–18.

[6] Khan T.S. *et al.*: *Experimental investigation of single phase convective heat transfer coefficient in a corrugated plate heat exchanger for multiple plate configurations*. Appl. Thermal Eng. **30**(2010), 8–9, 1058–1065.

[7] Jogi Nikhil G., Lawankar Shailendra M.: *Heat transfer analysis of corrugated plate heat exchanger of different plate geometry: A Review*. Int. J. Emerging Technol. Adv. Eng. **2**(2012), 10, 110–115.

[8] Wajs J., Mikielewicz D.: *Effect of surface roughness on thermal-hydraulic characteristics of plate heat exchanger*. Key Eng. Materials **597**(2014), 63–74.

[9] Lin D.T.W. *et al.*: *The otimal design process of the plate heat exchanger*. In: Proc. Int. Symp. Computer, Communication, Control and Automation, 2010, 978-1-4244-5567-6/10/©2010 IEEE.

[10] Niezgoda Żelasko B., Zalewski W.: *Plate heat exchangers, Part I*. Technika Chłodnicza i Klimatyzacyjna **170**(2010), 4, 130–136 (in Polish).

[11] Wiśniewski S., Wiśniewski T.: *Heat Transfer*. WNT, Warszawa 1994 (in Polish).

[12] http://www.aspentech.com/products/aspen-plateplus.aspx

[13] http://www.secespol.cz/en/produkty/vymeniky/deskove-pajene/la22-2/la22-20-2/

[14] Mikielewicz J.: *Determination of heat transfer coefficients for recuperators by use of the Wilson method*. Technika Chłodnicza i Klimatyzacyjna **10**(2001), 387–388 (in Polish).

[15] Mikielewicz D., Wajs J., Mikielewicz J.: *Determination of heat transfer coefficient in evaporator of the ORC using the Wilson method*. In: Proc. 17th Int. Conf. Heat Transfer and Renewable Sources of Energy, Szczecin-Miedzyzdroje 2008, 489–496.

[16] Shokouhmand H., Salimpour M.R., Akhavan-Behabadi M.A.: *Experimental investigation of shell and coiled tube heat exchangers using Wilson plots*. Int. Comm. Heat Mass Transfer **35**(2008), 1, 84–92.

[17] Cieśliński J.T.: *Effect of nanofluid concentration on two-phase thermosyphon heat exchanger performance*. Arch. Thermodyn. **37**(2016), 2, 23–40.

archives
of thermodynamics
Vol. **37**(2016), No. 3, 31–43
DOI: 10.1515/aoter-2016-0018

Influence of nitrogen on thermodynamic properties and plasma composition in discharge tube of CO-laser

GALINA M. GRIGORIAN[a]
ADAM CENIAN[b*]

[a] St. Petersburg State University, 199034 St. Petersburg, Russia

[b] Institute of Fluid Flow Machinery, Polish Academy of Sciences, Fiszera 14, 80-231 Gdansk, Poland

Abstract The role of the addition of nitrogen to the discharge plasma of CO lasers on thermodynamic properties and composition of the laser active medium is discussed here. It is shown that nitrogen addition improves laser characteristics and changes the composition of the laser active medium. The addition of nitrogen significantly decreases CO dissociation level and concentrations of C atoms created in plasma-chemical reactions of laser discharge.

Keywords: CO-laser; Vibrational kinetics; Dissociation; Plasma-chemistry; CN molecules; C_2; Electron kinetics

1 Introduction

The processes of molecular dissociation and following plasma-chemistry, changing the composition of laser active-medium and laser characteristics, determine the long-term and effective operation of molecular sealed-off lasers (working without the gas exchange in the laser discharge tube).

These processes are extremely important for a CO-laser operation. The vibrationally excited $CO(X^1\Sigma,v)$ molecules, involved in the laser-radiation

*Corresponding Author. E-mail: cenian@imp.gda.pl

generation, hardly relax during collisions with initial component of the active mixture, however the ratio of their relaxation could significantly increase when collision partners are some products of the above mentioned plasma-chemical processes [1]. It is well known (see e.g. [2] and the references therein), that sealed-off CO-lasers usually apply mixtures with significant concentrations of nitrogen, which support better energy-characteristics and improve long-life performance of the laser.

Addition of nitrogen molecules to the laser active-mixture results in the increase of population of vibrationally excited CO molecules due to vibrational-vibrational (VV′) relaxation processes, where V′ denotes vibrations of other molecule. However, there are some important indicators pointing to the fact that improvements of CO-laser operation after nitrogen addition does not necessary result from additional mechanism of CO states excitation. An addition of nitrogen to He-CO mixture leads to a significant change in plasma-chemical products. Firstly, some new nitrogen-containing products appear: N atoms, molecules CN, NO, etc. Secondly, the nitrogen and nitrogen-containing products influence plasma composition of initial He-CO mixture.

Up to now the influence of nitrogen on plasma-chemistry of CO laser has rarely been investigated. There is a lack of comprehensive models for plasma-chemistry of He-CO-N_2 mixtures (except some common feature with plasma of CO_2 laser [3–5]), which would help to estimate the level of degradation of the initial laser mixture. However, it has been shown in [5] that a CO_2 laser plasma with a high nitrogen content, $30\% < [N_2] < 50\%$, ensuring proper storage of the vibrational energy in CO_2 lasers, is characterized by a low electron temperature and thus, small chemical reactivity, i.e., a small level of CO_2 dissociation. From the investigations it follows that mixture decomposition decreases with an increase of N_2 content in the CO_2 laser mixtures. In contrast, electron temperature does not decrease after nitrogen additions to He-CO plasma. The temperature is constant or even slightly increases (up to 15%).

However, there is a small amount of experimental data on products of plasma-chemistry in such discharges and on products' dependence on experimental conditions and discharge time-duration. The concentrations of CN molecules have been measured in flowing $He = CO - N_2$ discharges [6–8] and in sealed-off systems, and theoretically determined based on a model of plasma-chemical processes – see [9]. Unfortunately, dependence of other plasma-chemical products in CO-laser medium on experimental

conditions were not studied. In order to proceed with the development of plasma-chemistry models for CO-laser-medium and to estimate how plasma-chemistry products influence CO-vibrational-state populations it is important to determine the parameters of active mixtures including temperatures (gas and vibrational) and CO-vibrational-state populations.

Thus, the aim of this work is to determine the influence of nitrogen additions to He-CO mixtures on thermodynamic characteristics, CO-vibrational-states populations and products of plasma-chemistry in laser tube discharges. The experiments were performed under conditions typical for discharge tubes of CO-laser working in sealed-off and gas flowing regimes.

2 Experimental set-up

Experimental set-up has been described already in a previous work [9]. The water-cooled discharge tube from molybdenum glass, 17 mm in diameter, was used in the experiment. The lengths of discharge zone was 50 cm. Hollow cylindrical electrodes from tantalum were installed in the side branches of the discharge tube at a distance of 4 cm from its axis. A discharge was excited using DC currents of 10–100 mA. The experiment was performed for initial He-CO and He-CO-N_2 mixtures. The relative CO and N_2 concentrations were varied in the range 3–15%. Gas pressure was set at 0.67–2 kPa. The setup can work in sealed-off and gas-flowing regimes (gas velocities 1–3 m/s were applied).

Initially, the gas mixtures used in the experiments were carefully purified by using a system of traps with silica-gel and zeolite. The mixture composition in the discharge tube was analyzed with a MSC-6 time-of-flight mass-spectrometer [7]. Periodically repeated gas probing from the discharge tube enabled the control of time evolution of stable product concentrations in the laser-discharge plasma.

The emission spectra from the discharge positive-column was registered using a spectrometer in the range 300–6000 nm, in order to determine the respective populations of vibrationally excited states of $CO(X^1\Sigma)$ and gas temperature along the symmetry axis of the discharge tube as well as its radial profile. The determination was done by analysing the rotational structure of CO vibrational bands. The emission spectra also enabled the determination of electronically excited particles in the plasma of the gas discharge.

The vibrational distribution of CO molecules in the ground electronic

state ($X^1\Sigma$) was determined from the spectra of IR (infrared) molecular emission at the (v$\rightarrow$ v-1) fundamental frequency, and the first (v$\rightarrow$ v-2) overtone.

The analysis of the emission spectra enabled the determination of the gas and vibrational temperatures as well as the concentrations of the electronically excited particles in the gas-discharge plasma. During the experiment the overtones emission was registered from neighbourhood of symmetry axis ($\sim$ 3 mm) in the discharge positive column. The spectra were studied using a Czerny-Turner monochromator with a diffraction grating of 300 and 1200 lines/mm. Cooled (by liquid nitrogen) photoresistors HgCdTl and uncooled InSb were used as photodetectors.

Lack of cataphoresis significant influence during measurements in systems without gas flows was proved. It was confirmed by registering He line intensities and CO molecular band at various points along the symmetry axis of the discharge tube using an optical waveguide.

The electric field in the discharge was determined by measuring the voltage drops across the discharge gap and the electrode sheaths. The electrode sheath voltages were found from the voltage measurements in experiments with different discharge lengths. A typical electrode sheath voltage was 350–400 V. The estimated value of the reduced electric field E/N (where E is electric field and N is concentration of neutral particles) was (2.1–3.2) 10^{-16} V cm^2.

For determination of absolute emission intensities, etalon lamps SI-8-220U and SR-2-32-RM were used. The plasma radiation was collected from the central region of discharge 2–3 mm in diameter.

The concentration of carbon atoms in the ground state was determined from absolute values of population of electronic excited states [1]. The method is based on knowledge of population of electrically excited states, which under experimental conditions applied here are excited mainly by direct collision from ground state and decay in radiation processes. Thus concentration of carbon in ground state can be determined from the simple balance equation:

$$[M_0] = [M^*]A/(n_e K_1) \ ,$$

where: M^* – a molecule in an excited state, A – Einstein coefficient for excited state, n_e – electron density in plasma discharge, and K_1 is the rate constant for carbon excitation by electron impact. Symbol [...] stand for concentration and asterisk (*) denotes excited state. For carbon atoms we used state $2p3p\,^1P_1$ by measuring 1.45 μm IR line intensity.

The population of CN in ground state was calculated from absorption spectra [9]. We have employed the method of two identical light sources. As a light source we used a discharge identical to the one we were investigating. It allows for a complete overlap of emission and absorption contours of both systems. The line of R-band of $K'' = 9$ transition (0,0) violet system CN($B^2\Sigma \rightarrow X^2\Sigma$) was used as in [2], where K'' is rotational quantum number.

Measurements of discharge concentrations of (CO, CO_2, C, CN, N_2) species and their dependence on experimental conditions were compared with results of calculations. The electron energy distribution functions (EEDF) were calculated for our conditions by Kochetov using the method described in [10].

The values of reduced electric field E/N and gas temperature was assumed in the model from experimental data. Electron density was determined from current and calculated value of electron drift velocity.

The measurements where performed for CO-laser-generation regime and without laser-radiation generation. In order to enforce laser generation a resonator in flat/spherical configuration was applied. A fully reflecting metallic mirror (from steel covered with gold) had 5 m curvature radius. The exit mirror (with transmission 85–95%) was a flat plate from CaF_2 or ZnSe covered by dielectric multilayer. Laser energy characteristics under the gas-flow regime were: power 0.4 W and electro-optic efficiency $\eta = 10\%$; under sealed-off regime 0.2 W and $\eta = 4.8\%$, respectively. The resonator was not optimised for the generation conditions.

3 Results and discussion

Measurements showed that a nitrogen addition to the He-CO laser medium results in substantial increase of CO vibrational temperatures. This should be related to transfer of vibrational energy from nitrogen to carbon oxide due to VV′ exchange. As a result a stationary state is realised in the laser medium, with a high level of vibrational energy in CO molecules.

Table 1 presents results of vibrational temperature (T_1) determination:

$$T_1 = E_1 / \ln(N_0/N_1), \tag{1}$$

where: E_1 – energy of the first excited vibrational state, N_0 and N_1 – populations of the ground and first excited vibrational state of CO molecule. The normal font numbers correspond to measurements in the gas flowing

regime, while numbers in bold font to sealed-off regime. As can be seen, the values for both regimes are relatively close. Reproducibility of the results was estimated as 10%.

Table 1: The CO vibrational temperature under different conditions.

Pressure	0.67 kPa			1.33 kPa		
Mixture/Current	50 mA	60 mA	70 mA	50 mA	60 mA	70 mA
He-CO=95:5	1750/1700	1800	1950	1700/1600	1850	1800
He-CO=91:9	1700	1700	1800	1700	1800	1800
He-CO-N_2 = 95:3:2	2850/2700	2800	2800	2700/2600	2750	2750
He-CO-N_2 = 95:4:1	2450/2400	2400	2500	2500/2400	2650	2650

Nitrogen in the mixture increased populations of CO excited vibrational-states, and this effect grows with the considered nitrogen concentrations. The laser generation was observed in He-CO-N_2 mixtures (at the level 0.4 W) but it wasn't observed when nitrogen was absent in the mixture under any considered experimental conditions.

It was found that a decrease of CO vibrational states-populations in the mixtures containing nitrogen proceeds under much higher energy inputs (currents) than in the mixtures without nitrogen. Figure 1 presents CO vibrational energy distributions for mixtures He-CO and He-CO-N_2 for different currents. It can be seen that populations in the He-CO-N_2 mixture fall with current value significantly slower. The populations fall when current value exceed 20 mA, the optimal current value under considered conditions.

It should be pointed out that the gas temperatures measured (near symmetry axis) in both mixtures He-CO and He-CO-N_2 were similar and vary in the range 360–480 K. These temperatures do not depend on gas flow.
One of the main causes of the smaller decrease of CO vibrational states-populations under increase of current value in the mixtures with nitrogen is probably related to lower CO-dissociation level (measured value) and lower concentrations of plasma-chemical products. Level of dissociation 15 min. after discharge was commenced is shown in Fig. 2. ($\Delta[CO]/[CO]_0$, where $[CO]_0$ is the concentration of CO molecules in initial mixture, and $\Delta[CO]$ is the change of CO concentration in discharge). A significantly lower CO-dissociation level is registered after nitrogen addition. Besides, it can be seen that the experimental values of CO dissociation level are

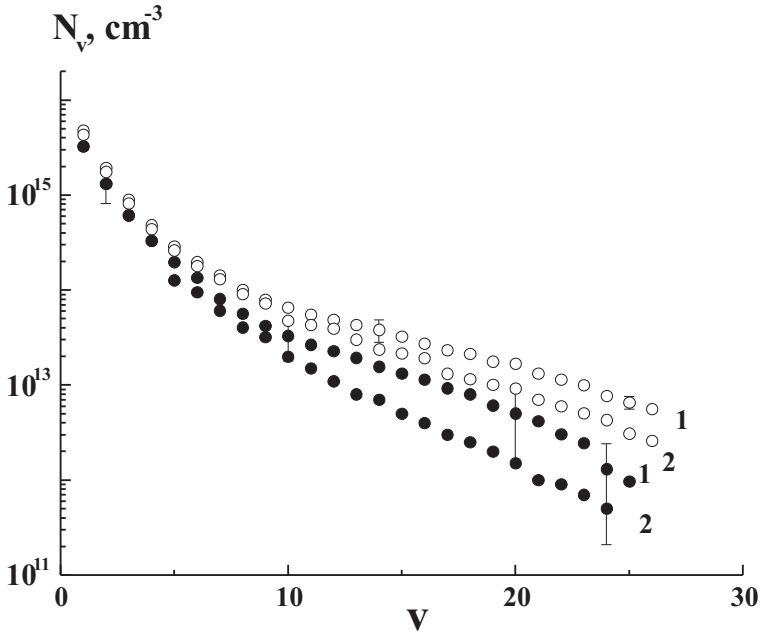

Figure 1: Populations of CO vibrational states in He-CO and He-CO-N_2 mixtures without laser-radiation generation at various discharge currents: black full circles – He:CO = 91:9 mixture; open circles – He:CO:N_2 = 91:4:5 mixture; curves 1 – current I = 25 mA, 2 – I = 40 mA; pressure P = 1.6 kPa.

significantly lower than those determined by calculation. At the same time, the calculated values of CO dissociation level for both mixtures are close to each other (full and dotted curves in Fig. 2). It is well known that the balance of CO concentrations in sealed-off discharge regimes should take into account three basic processes [1]:

- CO dissociation

$$\mathrm{CO} + e \rightarrow \mathrm{C} + \mathrm{O} + e \,, \tag{2}$$

$$\mathrm{CO} + \mathrm{CO}(a^3\Pi) \rightarrow \mathrm{CO_2} + \mathrm{C} \,, \tag{3}$$

- heterogeneous recombination of oxygen and carbon atoms

$$\mathrm{C} + \mathrm{O}^w \rightarrow \mathrm{CO} \quad \text{or} \quad \mathrm{O} + \mathrm{C}^w \rightarrow \mathrm{CO} \,, \tag{4}$$

where index w describes atoms adsorbed at the wall.

The process of CO dissociation in collisions with metastable He states

$$\mathrm{He}(m) + \mathrm{CO} \rightarrow \mathrm{He} + \mathrm{C} + \mathrm{O} \tag{5}$$

could be neglected under our case conditions, as the concentration of He atoms in metastable states is small.

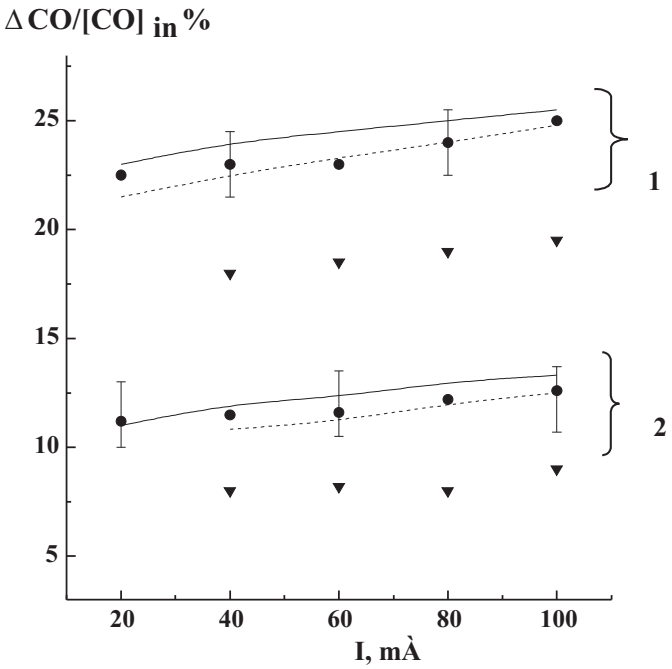

Figure 2: CO dissociation level as function of current 15 min after discharge turned-on: 1 – pressure P = 0.8 kPa, He-CO=95:5 mixture, full black circles – experiment, full curves – calculations; He-CO-N_2 = 95 : 3 : 2 mixture, full black triangles – experiment, dotted curves – calculations; 2 – pressure P = 1.33 kPa, He-NO=91:9 mixture – full black circles – experiment, full curves – calculations; He-CO-N_2 = 91 : 3 : 6 mixture, full black triangles – experiment, dotted curves – calculations.

The rates of dissociation in processes (2) and (3) do not change when nitrogen is added to the mixture, i.e., decrease in the CO dissociation level can be explained by rates for heterogeneous recombination (4). Such change of rates for process (4) could result from change of conditions on discharge-

tube-wall surface under nitrogen addition. It could be related partly to CN-molecules and C_nN_m polymers deposit on the walls.

The concentration of CO_2 molecules, which are created in laser discharge plasma, does not strongly depend on nitrogen addition and under the conditions considered here it was 5–10% of [CO] concentration. The CO_2 molecules in discharge plasmas of He-CO and He-CO-N_2, under the conditions considered here, are created in process (3) and destroyed in dissociation by electron impact

$$CO_2 + e \rightarrow CO + O + e \, . \tag{6}$$

Measurements showed that after nitrogen addition, the concentration of atomic carbon in discharge plasma decreases by 30–50%. They are created during the process (2) and (3) but are removed from plasma by diffusion to the wall.

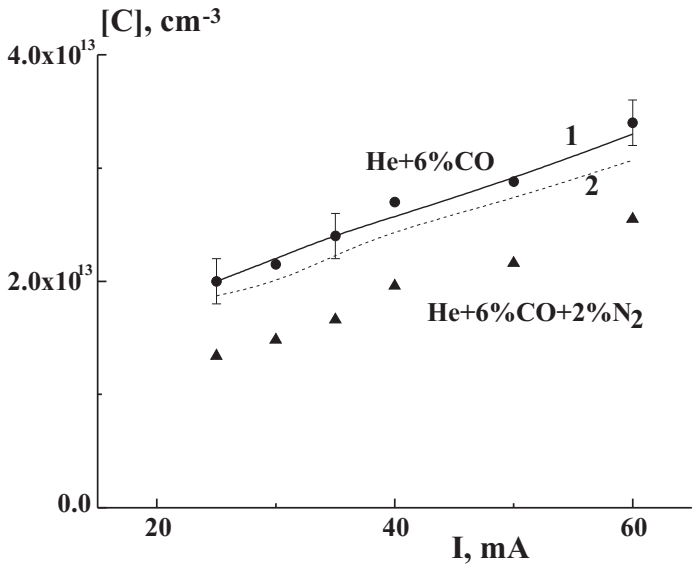

Figure 3: Carbon atom concentration as function of discharge 15 min after discharge turned-on: pressure P =1.6 kPa; symbols – experimental data, curves – calculations.

Figure 3 presents atomic C concentration measured in plasma and calculated using experimental data on concentrations of CO molecules. It is clearly seen that experimental data (points) for nitrogen-free mixtures agree well with calculated values (full curve). For the mixtures containing

nitrogen, experimental data are significantly lower than those calculated (dotted curve). Decrease of atomic carbon concentration after nitrogen additions in the He-CO mixture, can result from existence of additional processes with participation of atoms and carbon molecules. These include the following reactions:

$$C + N_2 + M \rightarrow \text{ products} , \tag{7}$$

$$C + NO \rightarrow \text{products} . \tag{8}$$

The rate constant of reactions (7) and M = Ar equals $K_7 = 3{\times}10^{-33}$ cm^{-6}/c [11]. These values for reaction (7) are large enough to influence the rate of carbon losses in the discharge.

Process (8) has an even more pronounced effect on atomic carbon, as its rate is close to a gasdynamic one (collision rate) [12,13]. In order for reaction (8) to significantly influence carbon losses it is sufficient that the concentration of NO molecules is of the order $5{\times}10^{11}$ cm^{-3}. The NO was not registered in the experiment mass spectra but method sensitivity to NO does not exceed $2{\times}10^{12}$ cm^{-3}, i.e., their existence in large enough quantity could not be excluded.

Besides, in He-CO-N_2 discharge plasmas CN molecules appear. Their concentration varies in the range $8{\times}10^{12}$ – $3{\times}10^{13}$ cm^{-3} under the conditions considered here. Figure 4 presents the measured and calculated values of CN concentrations as a function of discharge current. It can be seen that the measured and calculated values agree very well. Plasma-chemical processes determining CN concentration are described in [9] in detail. It was found that the CN molecules under conditions characteristic for discharge plasma of CO lasers are produced in processes

$$CO(X^1\Sigma) + N_2(A^3\Sigma^+, v \geq 2) \rightarrow CN(X^2\Sigma) + NO(X^2\Pi) , \tag{9}$$

$$CN(A^2\Pi) \rightarrow CN(X^2\Sigma) + h\nu , \tag{10}$$

The $CN(X^2\Sigma)$ molecule is lost due to diffusion and deposition on the wall-surface as well as in reaction with nitrogen atoms:

$$CN(X^2\Sigma) + N \rightarrow C + N_2 . \tag{11}$$

The CN molecules is excited to $A^2\Pi$ state in processes

$$CN(X^2\Sigma) + e \rightarrow CN(A^2\Pi) + e , \tag{12}$$

$$N_2(A^3\Sigma) + CO(X^1\Sigma\,, v \geq 6) \rightarrow CN(A^2\Pi) + NO(X^2\Pi)\,. \qquad (13)$$

In sealed-off systems the influence of heterogeneous processes on [CN] concentration is highly probable but there is a lack of data on their rates. However, the good agreement between experimental and theoretical results related to CN concentrations point to the fact that at the initial phase of discharge the heterogeneous processes do not influence CN concentration in discharge plasma of CO lasers.

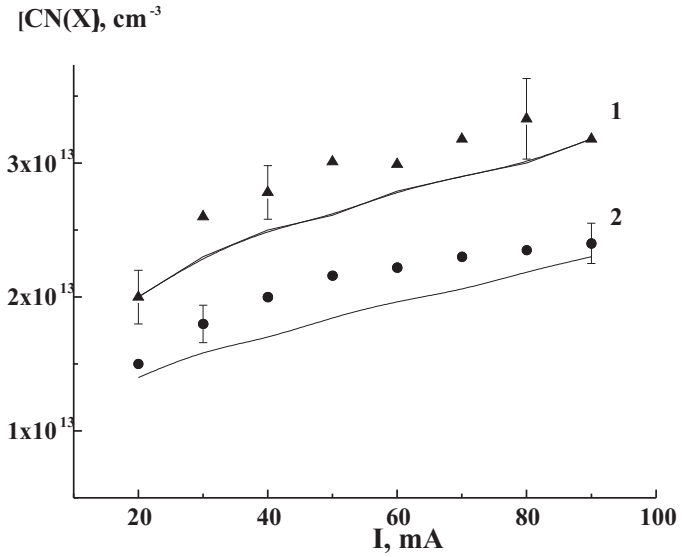

Figure 4: Concentrations of CN molecules as functions of discharge current, 15 min after discharge turned-on: 1 – He:CO:N_2 = 96:2:2, pressure P = 2.13 kPa; 2 – He:CO:N_2 = 91:6:3, pressure P = 0.67 kPa; symbols – experimental data, curves – calculations.

4 Conclusions

The performed measurements under conditions characteristic for discharge plasma in CO laser showed that nitrogen addition to the He-CO mixture leads to:

1. Significant increases in CO vibrational temperature as well as populations of CO excited states. A reduction of CO highly-excited vibrational-states populations with current is smaller in the case of mixtures with nitrogen additions.

2. The CO dissociation level in discharge plasma decreases 20–30%, which could result from changes in heterogeneous recombination of atomic oxygen and carbon and CO production.
3. The C atom concentration decreases 30–50%. This may result from additional channels with participation of nitrogen and possibly NO, which increase [C] losses.
4. The CN molecule concentrations are in the range $8\times10^{12} - 3\times10^{13}\mathrm{cm}^{-3}$ under the considered conditions.

Acknowledgement This work has been supported by St. Petersburg University (grant No. 11.38.203.2014). Authors express special thanks to I.V. Kochetov for precise calculations of EEDF.

Received 4 October 2016

References

[1] Grigorian G.M., Kochetov I.V.: *Balance of CO molecules in the plasma of a sealed-off CO laser*. Plasma Phys. Rep. **30**(2004), 788–796.

[2] Aleinikov V.S., Masychev V.I.: *CO Lasers*. Moscow, Radio i Svyaz' 1990.

[3] Cenian A., Chernukho A., Borodin V., Śliwiński G.: *Modeling of plasma-chemical reactions in gas mixture of CO_2 lasers. 1. Gas decomposition in pure CO2 glow discharge*. Contr. Plasma Phys. **34**(1994), 25–37.

[4] Cenian A., Chernukho A., Borodin V.: *Modeling of plasma-chemical reactions in gas mixture of CO_2 lasers. 2. Theoretical model and its verification*. Contrib. Plasma Phys. **35**(1995), 273–296.

[5] Cenian A., Chernukho A., Kukiełło P., Zaremba R., Borodin V., Śliwiński G.: *The improvement of self-regeneration of gas mixtures in a convection-cooled 1.2 kW CO_2 laser*. J.Phys. D: Appl.Phys. **30**(1997), 1103–1110.

[6] Trubacheev E.A.: *Investigation of physico-chemical characteristics of CO-lasers plasma*. Trudy FIAN **102**(1977), 3–57.

[7] Grigorian G.M., Dymshits B.M., Ionikh Yu.Z.: *Influence of oxygen on the parameters of the active medium in an electric-discharge CO laser*. Sov J Quant Electron **19**(1989), 889–893.

[8] Ochkin V.N., Savinov S.Yu., Sobolev N.N., Trubacheev E.A.: *Concentration of CN radicals in carbon monoxide laser plasma*. Sov.J. Quantum Electron **4**(1974), 319–321.

[9] Grigorian G.M., Cenian A.: *Formation and Excitation of CN Molecules in He-CO-N_2-O_2 Discharge Plasmas*. Plasma Chem Plasma Process **31**(2011), 337–352.

[10] Konev Yu.B., Kochetov I.V., Pevgov V.G., SharkovV. F.: *Analysis of the kinetic processes determining the parameters of CO lasers*. Preprint IAE-2821, Moscow (1977) (in Russian).

[11] Husain D., Kirsh L.J.: *Reactions of atomic carbon C(23PJ) by kinetic absorption spectroscopy in the vacuum ultra-violet*. Trans. Faraday Soc, **67**(1971), 2025–2035.

[12] Paramo A., Canosa A., Le Picard D., Sims I.R.: *An experimental study of the intersystem crossing and reactions of* $C_2(X^1\Sigma_g^+)$ *and* $C_2(a^3\Pi_u)$ *with* O_2 *and NO at very low temperature (24?300 K)*. J. Chem. Phys. **110**(2006), 3121–3127.

[13] Chastaing D., Le Picard D., Sims I.R.: *Direct kinetic measurements on reactions of atomic carbon,* $C(^3P)$*, with* O_2 *and NO at temperatures down to 15 K*. J. Chem. Phys. **112**(2000), 8466–8469.

archives
of thermodynamics
Vol. **37**(2016), No. 3, 45–62
DOI: 10.1515/aoter-2016-0019

Parametric study of fluid flow and heat transfer over louvered fins of air heat pump evaporator

TOMASZ MUSZYŃSKI[a]
SŁAWOMIR MARCIN KOZIEŁ[a,b*]

[a] Gdansk University of Technology, Narutowicza 11/12, 80-233 Gdańsk, Poland

[b] Reykjavik University, Menntavegur 1, 101 Reykjavik, Iceland

Abstract Two-dimensional numerical investigations of the fluid flow and heat transfer have been carried out for the laminar flow of the louvered fin-plate heat exchanger, designed to work as an air-source heat pump evaporator. The transferred heat and the pressure drop predicted by simulation have been compared with the corresponding experimental data taken from the literature. Two dimensional analyses of the louvered fins with varying geometry have been conducted. Simulations have been performed for different geometries with varying louver pitch, louver angle and different louver blade number. Constant inlet air temperature and varying velocity ranging from 2 to 8 m/s was assumed in the numerical experiments. The air-side performance is evaluated by calculating the temperature and the pressure drop ratio. Efficiency curves are obtained that can be used to select optimum louver geometry for the selected inlet parameters. A total of 363 different cases of various fin geometry for 7 different air velocities were investigated. The maximum heat transfer improvement interpreted in terms of the maximum efficiency has been obtained for the louver angle of 16 ° and the louver pitch of 1.35 mm. The presented results indicate that varying louver geometry might be a convenient way of enhancing performance of heat exchangers.

Keywords: Heat exchangers; Heat transfer intensification; CFD, Convection; Air source heat pump

*Corresponding Author. E-mail: koziel@ru.is

Nomenclature

c	–	specific heat, W/kg K
Fp	–	fin pitch, m
Ft	–	fin thickness, m
h	–	heat transfer coefficient, W/m^{2}K
H	–	louver width, m
k	–	conductivity, W/m K
Lp	–	louver pitch, m
ΔP	–	pressure drop, Pa
$\dot{\mathrm{Q}}$	–	heat flux, W
T	–	temperature, °C or K
ΔT	–	temperature drop, K
u, v, w	–	velocity components, m/s
$\dot{\mathrm{V}}$	–	volumetric flow rate, m^3/s
x, y, z	–	Cartesian coordinates

Greek symbols

α	–	louvers angle, deg
ρ	–	density, kg/m^3
η	–	thermal performance index

Subscripts

air	–	air
h	–	hydraulic
i, k	–	vectot components
in	–	inlet
out	–	outlet
p	–	at constant pressure,

1 Introduction

Heat exchangers play an important role in almost every engineering system [1]. Their primary purpose is heat transfer between two working fluids such as air, refrigerants, water, glycols, etc. For example, air-to-refrigerant exchangers are used in refrigeration and air conditioning [2], automotive [3], as well as heat pump industry [4]. One of the most important design challenges for this type of devices is improvement of their efficiency, especially the heat transfer rate [5,6]. In compact heat exchangers, thermal resistance is generally dominant on the air side and may account for over 80% of the total thermal resistance. The air-side heat transfer surface area is up to 10 times larger than the water-side one. However, water-side heat transfer coefficient is approximately 50 times higher than air-side one. Thus, the air-side thermal resistance turns out to be higher by a factor of five. Con-

sequently, any improvement in the heat transfer on the air side improves the overall performance of the heat exchanger. Louvered fins are frequently used on the air side of air conditioning evaporators and other heat exchangers to enhance the overall heat transfer rate. The louvers act to interrupt the air flow and create a series of thin boundary layers which have lower thermal resistance than the thick boundary layers on the plain fins [7]. Optimization of heat exchanger geometry may considerably improve energy savings in these systems [8]. On the other hand, improved efficiency leads to reduced exchanger size, thus significantly reduces its manufacturing cost, and annual energy expenditures related to pumping [9].

Unfortunately, optimization and design improvement of heat exchangers is a very challenging task. Experimental studies aimed at optimizing louvered fin geometries tend to be costly and time-consuming because of a considerable number of geometrical parameters involved (among others, louver angle and length, as well as fin length, pitch, and thickness) and complex relationships between these parameters and device's performance figures [10]. For the sake of accurate evaluation as well as shortening the development cycle, the design processes are nowadays more and more relying on computer models rather than on physical prototypes [11,12]. The fundamental design tools involve computational fluid dynamics (CFD) simulations [13] utilizing numerical solutions of the fluid governing equations. CFD models offer an accurate evaluation of the structure at hand; however, their downside is high computational cost. In particular, CFD-driven design optimization may be impractical when using conventional techniques such as gradient search with numerical derivatives. One of the methods to accelerate the optimization process is by using fewer evaluations or to exploit a simplified computational model. Typically, function-approximation surrogate models are used, i.e., constructed by means of the design of experiments and simulation data acquisition and fitting [14]. Function-approximation models are versatile, however, they normally require a substantial amount of data samples to ensure good accuracy. Typically, these models are set up in the entire design space [15]. More efficient methods involve surrogate-based optimization with physical surrogates, e.g., suitably corrected lower-fidelity simulation models [16]. Utilization of physics-based surrogates is not widespread in the context of CFD modeling of compact heat exchangers of complex geometries.

Enhancement of convective heat transfer can be realized by means of reducing the thickness of a thermal boundary layer, increasing the distur-

bance in a fluid, and increasing the velocity gradient at the solid wall.

The foregoing literature review indicates that in all available studies, the main emphasis was put on studying the effects of geometry parameter adjustment on the average air side heat transfer and the pressure drop characteristics of heat exchangers [7,17–19].

In this study, a two-dimensional numerical simulation of the air-side heat transfer and flow characteristics of the louvered fin-and-plate heat exchanger has been presented. Our investigations are carried out by varying both the louver pitch and the angle while modifying its geometry by changing the number of louvers in a bank. The transferred heat and the pressure drops have been investigated. The heat transfer performance for various fin geometries and dimensions has been obtained. The effects of pitch, angle, and louvers number on temperature and pressure drop have been studied at for the angle range from 10° to 70°. The predictions of the pressure and air temperature drop have been compared with available experimental data.

2 Computational model

Louvered plate fins are frequently used on the air side of air conditioning evaporators and other heat exchangers to enhance the overall heat transfer rate. Figure 1 shows the overview of a multi-louvered plate heat exchanger. The present study focuses on CFD parametric study of louvered fins plate heat exchanger for varying geometry. The following parameters are considered: louver angle, louver pitch and the number of louvers in the bank. Table 1 presents a list of all geometrical parameters used in calculations. The air flow direction is x-direction, the fin spanwise direction is y-direction and fin thickness direction is z-direction. Figure 2 shows the computational domain of the louvered fin. The computation domain was extended two times beyond the fin pitch of the original heat transfer zone for the entrance section to ensure the inlet uniformity, and at the exit, the domain was extended five times fin pitch in order to make sure that the exit flow boundary has no flow recirculation. Similar conditions were considered by many researchers [17,18], and have proven to predict experimental data within acceptable accuracy. Also, numerical simulations in 3D computational domain were carried out [7,19]. The grid system for the computation domain generated by commercial software ANSYS Gambit [20] is shown in Fig. 3, where the upstream and downstream parts of the computation

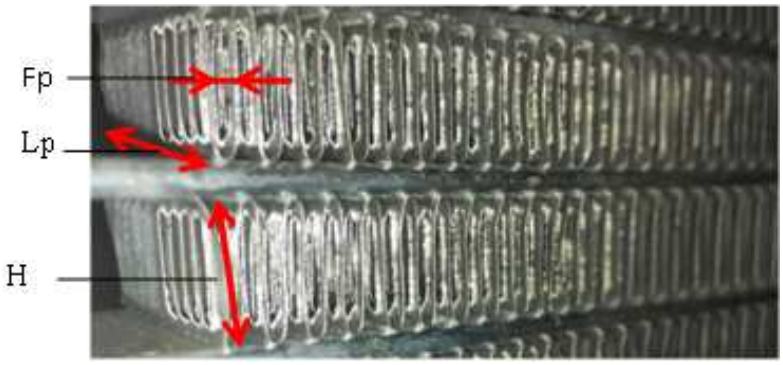

Figure 1: The overview of the multilouvered fin plate heat exchanger.

Table 1: Geometrical and working parameters of the tested evaporator of the air source heat pump.

Parameter	Value and unit
Fin thickness, F_t	0.1 mm
Number of louvers in bank	6–8
Fin pitch, F_p	2 mm
Louver pitch, L_p	0.9–1.4 mm
Louver angle	10–70
Fin length, L	36.6 mm
Louver width, H	6.53 mm
Inlet air temperature	290 K
Fin temperature	280 K
Inlet air velocity	2–8 m/s

domain are not presented in order to save the space. A grid convergence check indicated that the solution for the selected geometry consisting of approximately 400 000 elements results in about 2% offset compared to 1.6 million element grid.

The governing equations, for the forced steady, laminar, incompressible fluid flow and heat transfer in the physical space are as follows [20]: continuity equation

$$\frac{\partial}{\partial x_i}\left(\rho u_i\right) = 0 \,, \tag{1}$$

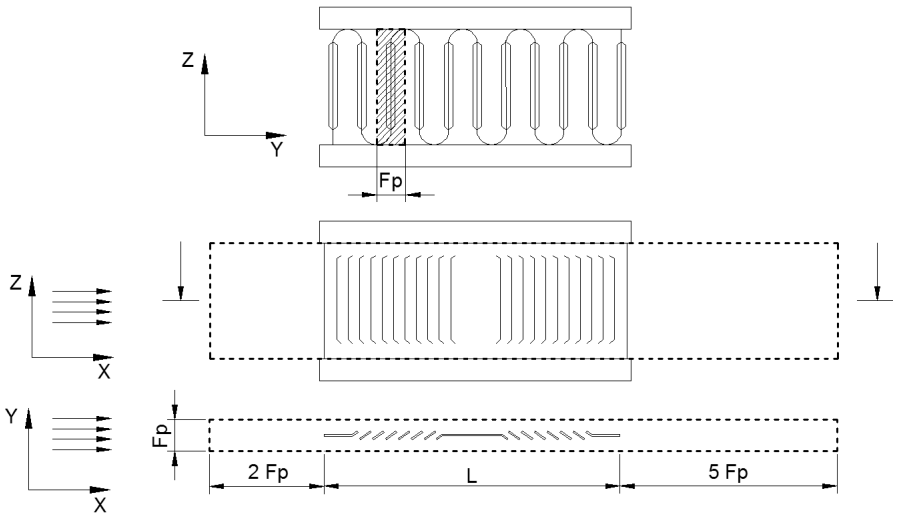

Figure 2: Schematic of louvered fins-plate heat exchanger computational domain.

(a) (b)

Figure 3: Two dimensional grid representation: (a) overview, and (b) close-up.

momentum equation

$$\frac{\partial}{\partial x_i}\left(\rho u_i u_k\right) = \frac{\partial}{\partial x_i}\left(\mu \frac{\partial u_k}{\partial x_i}\right) - \frac{\partial p}{\partial x_k}\,, \tag{2}$$

energy equation

$$\frac{\partial}{\partial x_i}\left(\rho u_i T\right) = \frac{\partial}{\partial x_i}\left(\frac{k}{c_p}\frac{\partial T}{\partial x_i}\right)\,. \tag{3}$$

The fluid is assumed to be incompressible with constant properties and the flow is laminar in a steady state condition. The temperature of the

fin surface is lower than that of the inlet air. The problem is simplified to a two-dimensional geometry, thus regarding velocity in z-direction (as depicted in Fig. 2). The boundary conditions are described for the three regions and are as follows

a) In the upstream extended region (domain inlet):
at the inlet boundary: $u = u_{in} = \text{const}$, $T = T_{in} = \text{const}$, $v = w = 0$;
at the upper and lower boundaries: $\frac{\partial u}{\partial y} = \frac{\partial w}{\partial y} = 0$, $v = 0$, $\frac{\partial T}{\partial y} = 0$.

b) In the downstream extended region (domain outlet):
at the upper and lower boundaries: $\frac{\partial u}{\partial y} = \frac{\partial w}{\partial y} = 0$, $v = 0$, $\frac{\partial T}{\partial y} = 0$;
at the outlet boundary: $\frac{\partial u}{\partial x} = \frac{\partial v}{\partial x} = \frac{\partial w}{\partial x} = 0$, $\frac{\partial T}{\partial x} = 0$.

c) In the fin region:
velocity on fin surface: $u = v = w = 0$;
temperature on fin surface: $T = \text{const}$.

All the procedures, including solver interfaces, modeling algorithms, and design specification scaling techniques were created as stand-alone routines implemented in Matlab environment [21]. Equations presented in previous sections are discretized using the finite volume technique. The equations are integrated over the individual computational cells, for steady state conditions over a domain. First-order upwind spatial discretization scheme is used both in the case of momentum and energy equations. For the pressure field calculations in steady state, the SIMPLE (semi-implicit method for pressure linkede equations) i, k – algorithm [20] is used in the commercial ANSYS FLUENT CFD [20] software toll, which uses a control-volume-based technique to convert the governing equations to algebraic equations that can be solved numerically. This involves subdividing the region in which the flow is to be solved into individual cells or control the volumes so that the equations can be integrated numerically.

3 Numerical results

In order to validate the numerical simulation reliability, geometrical dimensions described by Dong *et al.* [10] have been implemented in the computational domain and the results of numerical calculations were compared with original experimental data. Figure 4 compares experimental data with the simulation results. Calculations were made for varying inlet air velocity as indicated in Tab. 1. Steady state laminar incompressible

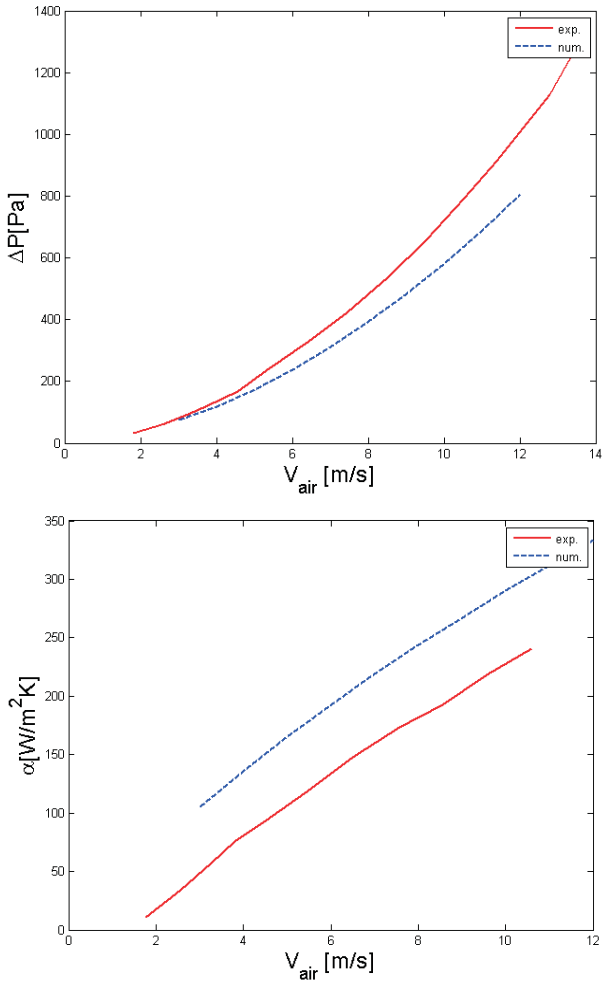

Figure 4: Experimental data by Dong *et al.* [10], compared to corresponding numerical data.

flow simulations exhibit sufficient consistency with the experimental data. The discrepancy between measurements and simulations in terms of the heat transfer is clearly visible as a constant shift between the data sets in the entire range of air velocity. This is because calculations are simplified and assume constant fin temperature, and do not include fin height which is assumed constant. The deviation between the pressure drop is much smaller with both data sets showing similar trends as a function of the air

velocity. Overall, the correlation between experimental and simulation data is sufficient to justify the utilization of computational model in searching for the optimal fin geometry.

Selected numerical results are shown in Figs. 5 through 7. The contours of the pressure, temperature and velocity are presented for the inlet air velocity of 3 m/s. It can be observed that at the low air velocity, most of the air flows through the gap between the fins rather than through the louvers. This can be attributed to the high flow resistance presented by the louvers. Since the air has less kinetic energy, most of it passes through the path of least resistance, i.e., through the fin gaps. The air temperature reaches the fin temperature in the first row of the louvers. Consequently, the heat transfer performance of the fin is poor (see Fig.7). The second half of the fin only accounts for the pressure loss without any significant heat transfer. At higher velocity, the thermal layers around the louvers are thinner and the flow is more aligned with the louvers. In this case, the temperature of the air does not decrease as fast as along the flow direction, and a significant temperature difference is maintained between air and the fin. Hence, the heat transfer rate is increased with the increased air velocity.

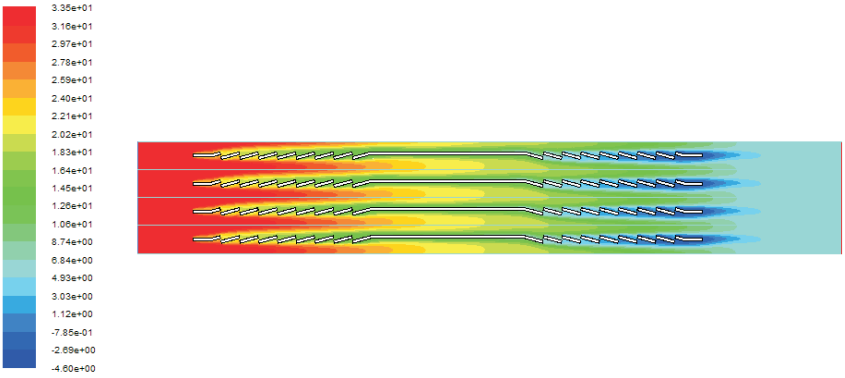

Figure 5: Contours of total pressure in pascals for $v_{air} = 3$ m/s.

Figure 5 show the total pressure distribution across the louvered fin. It can be observed that the low-pressure zone is formed near the louvers due to formation of the boundary layer. The air flowing through the louvers impinges on the flat plate and it is turned. This flow diversion results in a high-pressure zone in the middle plane, and this effect is more pronounced for increasing air velocity. These conjectures are in correspondence with obtained velocity profiles shown in Figs. 6.

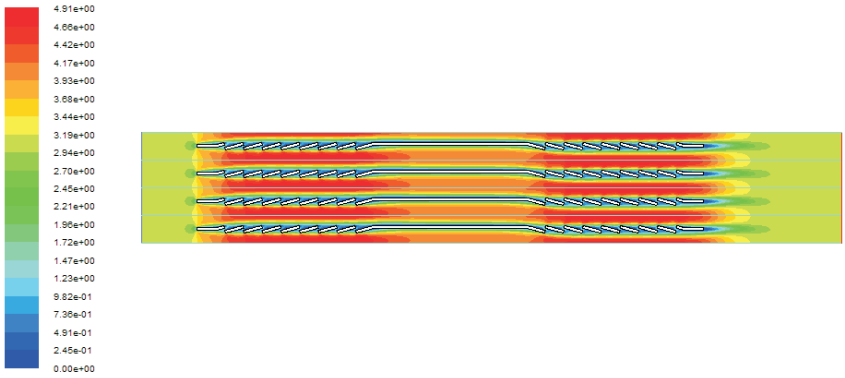

Figure 6: Contours of velocity magnitude in m/s for $v_{air} = 3$ m/s.

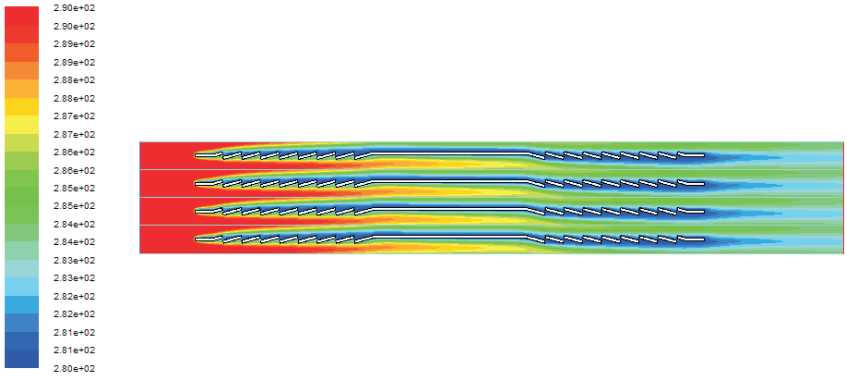

Figure 7: Contours of total temperature in kelvins for $v_{air} = 3$ m/s.

The heat transfer from the ambient air in the gap between the two fins to the refrigerant inside the tube, and the total pressure drop values of air across the heat exchanger were calculated numerically for each geometry model. With assumed constant air properties, i.e., density and specific heat, transferred heat is proportional to the volumetric flow rate and temperature drop. The results are presented in the form of obtained air temperature drop, calculated as a difference between the average temperatures on the inlet and the outlet boundary, for constant air flow rate:

$$\triangle T = \overline{T}_{in} - \overline{T}_{out} \ , \tag{4}$$

where overbar stand for area-averaged value. The pressure drop of air

passing through the fins is also taken into consideration:

$$\triangle P = \overline{P}_{in} - \overline{P}_{out} \ . \tag{5}$$

Figures 8 and 9 show the simulated heat transfer and pressure drop characteristics, presented in terms of the obtained temperature and pressure drops calculated from Eqs. (10) and (11). The values have been calculated using geometry parameters such as the louver pitch, Lp, louver angle, α, and the number of louver blades from configurations presented in Tab. 1 and Fig. 2. The calculated temperature and the pressure drop values for the varying velocities were also provided to compare with variable louver pitch and angles. The total heat transfer rate was normalized in form of ΔT to ensure fair comparison in all cases. It can be observed from the results gathered in plots that the best heat transfer per segment was obtained for the louver angle of 70° and the louver pitch equal to 1.35 mm. The maximum normalized heat transfer enhancement was 14%. The maximum enhancement of the heat transfer is associated with pressure drop per segment that is 10 times higher than for the reference case.

Figure 8 shows the effect of the louver angle and pitch on the pressure drop. It can be observed that the pressure drop increases with the louver angle and reaches its maximum value at 70°. Furthermore, it decreases with the decreased louver pitch for all cases. The pressure drop increases rapidly with the louver angle higher than 40°. This is because at higher velocities – which corresponds to higher Reynolds numbers – the flow is aligned with the louver angle. Larger louver angles increase the flow blockage and enforce more flow through the louver blades. Figure 9 shows the effects of the same geometry parameters on the simulated temperature drop. The rapid drop can be observed in all cases for louver angles below 20°. This drop is more rapid in the case of larger louver pitch values. The relatively flat response can be observed for louver angles between 20° and 40°. The effect of louver pitch on the obtained ΔT is more visible in case of higher louver angles, where it attains its maximum value for $\alpha = 70°$ and $Lp = 1.3$–1.4 mm which corresponds to maximum ΔP.

A simple method of selecting the optimal geometry can be formulated as follows. The pressure drop is a function of the friction factor based on the fin surface condition and position. Thus, an engineer is frequently interested in the pressure drop needed to sustain an internal flow because this parameter determines the fan power requirements. The hydraulic pumping power, W, required to overcome the resistance to the flow associated with this pressure

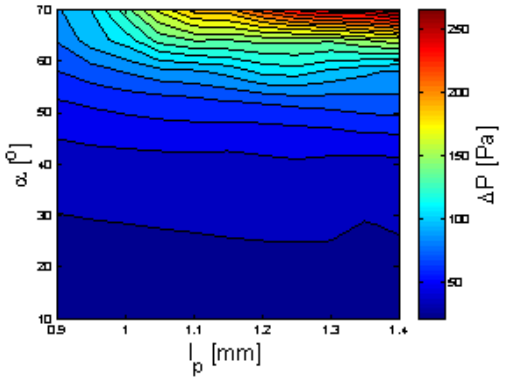

(a)

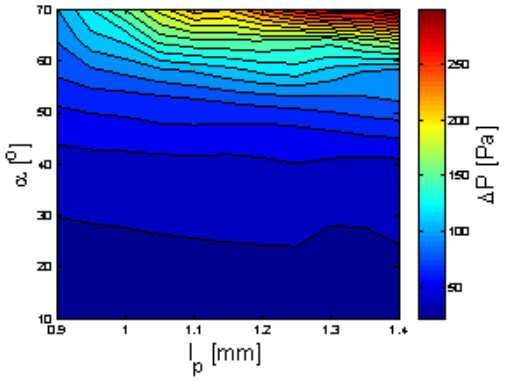

(b)

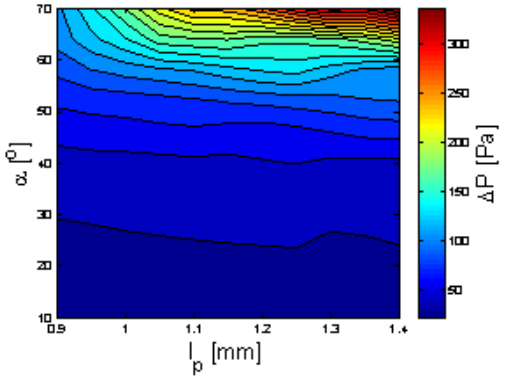

(c)

Figure 8: Numerically predicted pressure drop for air velocity $v_{air} = 3$ m/s, for (a) six, (b) seven, and (c) eight louvers.

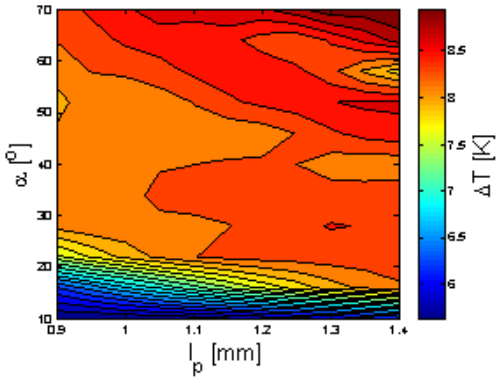

(a)

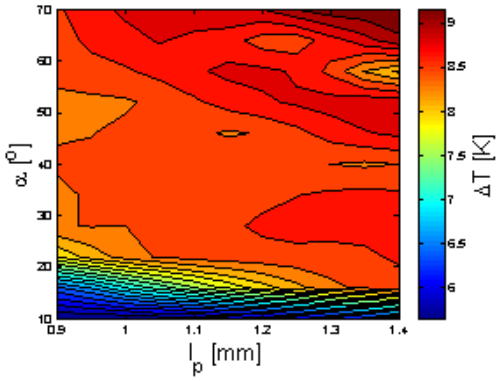

(b)

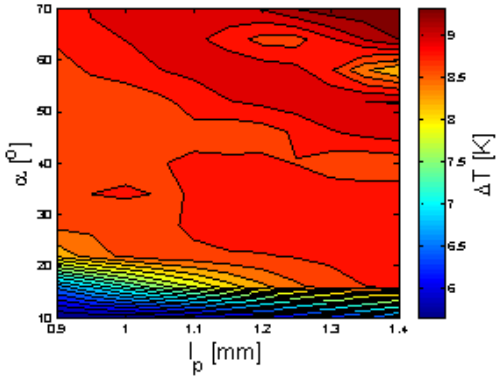

(c)

Figure 9: Numerically predicted temperature gradient for air velocity $v_{air} = 3$ m/s, for (a) six, (b) seven, and (c) eight louvers.

drop ΔP may be expressed as

$$P_h = \triangle P \dot{V} \ , \tag{6}$$

where the volumetric flow rate, $\dot{V}$, may, in turn, be expressed as $\dot{V} = \dot{m}/\rho$, i.e. the ratio of mass flow rate $\dot{m}$ and mass density ρ (kg/m3 for an incompressible fluid. The power required to move the fluid across the bank is often a major operating expense and is directly proportional to the pressure drop. Heat transferred from ambient air to the high pressure evaporator can be calculated as

$$\dot{Q} = \dot{V} \, \rho \, c_p \, \triangle T \ . \tag{7}$$

Overall thermal performance of the heat exchanger can be expressed as a ratio of the pumping power to the transferred heat, as dimensionless index

$$\eta = \frac{\dot{Q}}{P_h} = \frac{\rho \, c_p \, \triangle T}{\triangle P} \ . \tag{8}$$

Figure 10 shows the effect of the geometry parameters on the performance calculated using (8). Rapid performance drop can be observed in all cases for louver angles larger than 40°. Furthermore, a maximum performance region can be identified, for all considered cases, for the louver angle ranging from 16 to 20°. This region is shifted towards the lower louver pitch for the increased number of louver blades. As previously described, the simulations were repeated for air velocities from 3 to 8 m/s. The maximum performance region is shifted towards the higher louver pitch values for the decreased inlet air velocity. The maximum performance for cases from the whole computational domain can be compared to identify the influence of changing the number of the louver blades. The maximum performance in all cases was obtained for the louver angle $\alpha = 16°$. Figure 11 shows a single maximum performance point as a function of air velocity (for variable α and Lp). It can be observed that the performance is higher for lower air velocities. Also, a slight increase of performance can be observed between the compared cases.

As mentioned earlier, the maximum performance was obtained for the louver angle $\alpha = 16°$. Therefore, its influence is not depicted. In all cases, the louver pitch length smaller than $Lp = 1.2$ mm resulted in degraded performance compared to the optimal value. As indicated in Fig. 12, the maximum performance is obtained for different louver blade numbers and pitch. For higher inlet air velocities, the maximum performance is obtained for a smaller length of the louver pitch.

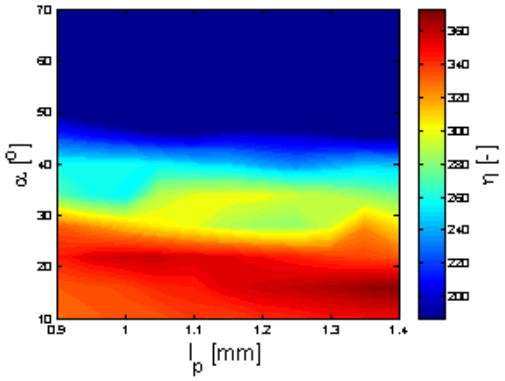

(a)

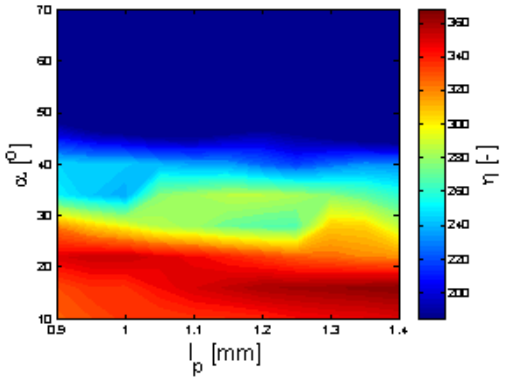

(b)

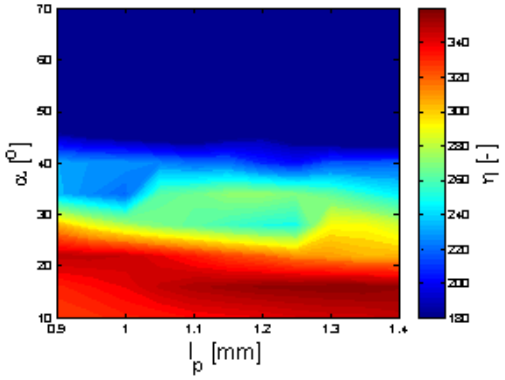

(c)

Figure 10: Numerically predicted temperature gradient for air velocity $v_{air} = 3$ m/s, for (a) six, (b) seven, and (c) eight louvers.

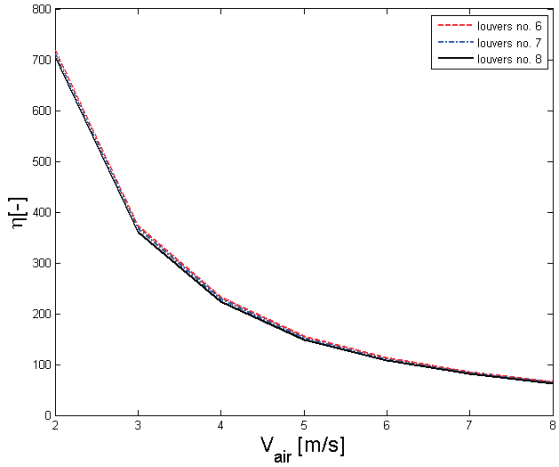

Figure 11: Maximum performance as a function of frontal air velocity for selected geometries.

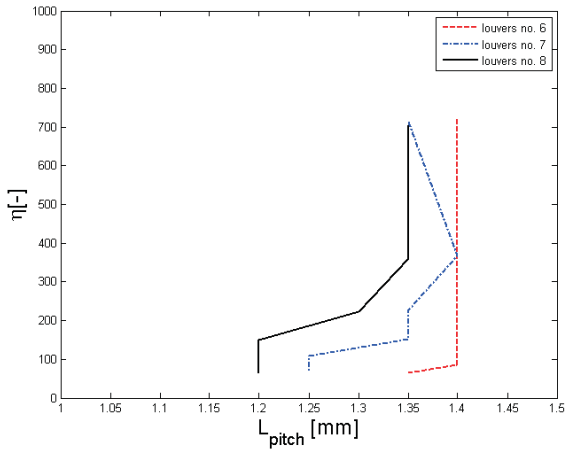

Figure 12: Maximum performance as a function of louver pitch for selected geometries.

4 Conclusion

Numerical simulations of compact louvered fin heat exchangers have been performed in order to determine heat transfer and pressure drop characteristics. A total of 363 different configurations has been studied. For the sake of validation of the computational model, the simulation results have been

compared with experimental data. The computed heat transfer coefficients and pressure drops are found to be in good agreement with the experiment within the considered flow range. A simple procedure for identifying the optimal geometry has been presented. A parametric variation of the geometry provides a map to find the desired configuration for which the heat transfer to the pressure drop ratio attains its maximum. Furthermore, for each louver blade number and air inlet velocity, a region with a local maximum of performance can be found. Among all considered geometry parameters, the louver angle of 16° yields the maximum performance for all considered combinations of the flow rate and the louver pitch. The future work will be focused on the development of numerical optimization techniques for finding the optimum heat exchanges geometry as well as including a heat exchanger size cost factor in the optimization process.

Acknowledgements Calculations were carried out at the Academic Computer Centre TASK in Gdańsk.

Received 16 June 2016

References

[1] Cengel Y.A., Boles M.A.: *Thermodynamics: An Engineering Approach*, McGraw-Hill, 2015.

[2] Kandlikar S.G.: *Two-phase flow patterns, pressure drop, and heat transfer during boiling in minichannel flow passages of compact evaporators*. Heat Trans. Eng. **23**(2002), 5–23.

[3] Taler D.: *Mathematical modeling and control of plate fin and tube heat exchangers*. Energy Convers. Manag. **96**(2015), 452–462 (DOI:10.1016/j.enconman.2015.03.015).

[4] Hepbasli A., Kalinci Y.: *A review of heat pump water heating systems*. Renew. Sustain. Energy Rev. **13**(2009), 1211–1229 (DOI:10.1016/j.rser.2008.08.002).

[5] Mikielewicz D., Muszyński T., Mikielewicz J.: *Model of heat transfer in the stagnation point of rapidly evaporating microjet*. Arch. Thermodyn. **33**(2013), 1, 139–152.

[6] Mikielewicz D., Jakubowska B.: *Prediction of flow boiling heat transfer coefficient for carbon dioxide in minichannels and conventional channels*. Arch. Thermodyn. **37**(2016), 2, 89–106.

[7] Gunnasegaran P., Shuaib N.H., Abdul Jalal M.F., Gunnasegaran P., Shuaib N.H., Abdul Jalal M.F.: *The effect of geometrical parameters on heat transfer characteristics of compact heat exchanger with louvered fins*. ISRN Thermodyn. 2012 (2012) 1–10 (DOI:10.5402/2012/832708).

[8] Wang C.-C. Lee, W.-S., Sheu W.-J.: *A comparative study of compact enhanced fin-and-tube heat exchangers*. Int. J. Heat Mass Transf. **44**(2001), 3565–3573. doi:10.1016/S0017-9310(01)00011-4.

[9] Zhang X., Tafti D.: *Flow efficiency in multi-louvered fins*. Int. J. Heat Mass Transf. **46**(2003), 1737–1750 (DOI:10.1016/S0017-9310(02)00482-9).

[10] Dong J., Chen J., Chen Z., Zhang W., Zhou Y.: *Heat transfer and pressure drop correlations for the multi-louvered fin compact heat exchangers*. Energy Convers. Manag. **48**(2007), 1506–1515 (DOI:10.1016/j.enconman.2006.11.023).

[11] Xia Y., Zhong Y., Hrnjak P.S., Jacobi A.M.: *Frost, defrost, and refrost and its impact on the air-side thermal-hydraulic performance of louvered-fin, flat-tube heat exchangers*. Int. J. Refrig. **29**(2006), 1066–1079 (DOI:10.1016/j.ijrefrig.2006.03.005).

[12] Kim S.Y., Paek J.W., Kang B.H.: *Flow and heat transfer correlations for porous fin in a plate-fin heat exchanger*. J. Heat Transfer. **122**(2000), 572 (DOI:10.1115/1.1287170).

[13] Ameel B., Degroote J., Huisseune H., De Jaeger P., Vierendeels J. et al.: *Numerical optimization of louvered fin heat exchanger with variable louver angles*. J. Phys. Conf. Ser. **395**(2012), 12054 (DOI:10.1088/1742-6596/395/1/012054).

[14] Leifsson L., Koziel S.: *Aerodynamic shape optimization by variable-fidelity computational fluid dynamics models: A review of recent progress*. J. Comput. Sci. **10**(2015), 45–54 (DOI:10.1016/j.jocs.2015.01.003).

[15] Koziel S., Ciaurri D.E., Leifsson L.: *Surrogate-based methods*. Stud. Comput. Intell. **356**(2011), 33–59 (DOI:10.1007/978-3-642-20859-1_3).

[16] Koziel S., Ogurtsov S., Leifsson L.: *Knowledge-based response correction and adaptive design specifications for microwave design optimization*. In: Procedia Comput. Sci., 2012: 764–773 (DOI:10.1016/j.procs.2012.04.082).

[17] Hsieh C.T., Jang J.Y.: *3-D thermal-hydraulic analysis for louver fin heat exchangers with variable louver angle*. Appl. Therm. Eng. **26**(2006), 1629–1639 (DOI:10.1016/j.applthermaleng.2005.11.019).

[18] Malapure V.P., Mitra S.K., Bhattacharya A.: *Numerical investigation of fluid flow and heat transfer over louvered fins in compact heat exchanger*. Int. J. Therm. Sci. **46**(2007), 199–211 (DOI:10.1016/j.ijthermalsci.2006.04.010).

[19] Ameel B., Degroote J., Huisseune H., De Jaeger P., Vierendeels J., De Paepe M.: *Numerical optimization of louvered fin heat exchanger with variable louver angles*. J. Phys. Conf. Ser. **395**(2012), 12054 (DOI:10.1088/1742-6596/395/1/012054).

[20] *Fluent*. ANSYS Fluent 12.0 user's guide, Ansys Inc. 15317 (2009) 1–2498 (DOI:10.1016/0140-3664(87)90311-2).

[21] *Matlab documentation*. Matlab. (2012) R2012b (DOI:10.1201/9781420034950).

archives
of thermodynamics
Vol. **37**(2016), No. 3, 63–78
DOI: 10.1515/aoter-2016-0020

Analytical 1D models of the wall thermal resistance of rectangular minichannels applied in heat exchangers

WITOLD RYBIŃSKI *
JAROSŁAW MIKIELEWICZ

Institute of Fluid Flow Machinery, Polish Academy of Sciences, Fiszera 14, 80-231 Gdańsk, Poland

Abstract The paper presents four 1-dimensional models of thermal resistance of walls in a heat exchanger with rectangular minichannels. The first model is the simplest one, with a single wall separating two fluids. The second model of the so called equivalent wall takes into account total volume of intermediate walls between layers of minichannels and of side walls of minichannels. The next two more complicated models take separately into account thermal resistance of these walls. In these two models side walls are treated as fins. The results of models comparison are presented. It is shown that thermal resistance may be neglected for metal walls but it should be taken into account for the walls made of plastics. For the case of non-neglected wall thermal resistance the optimum wall thickness was derived. Minichannel heat exchangers made of plastic are larger than those built of metal, but are significantly cheaper. It makes possible to use of such exchangers in inexpensive microscale ORC installations.

Keywords: Minichannel heat exchanger; Wall thermal resistance; Rectangular minichannel

Nomenclature

A	–	heat transfer area, m^2
a, b	–	sides of rectangular cross-section, m
B	–	coefficient
d	–	wall thickness, m

*Corresponding Author. E-mail: witold.rybinski@imp.gda.pl

d_h – hydraulic (and thermal) diameter, m
k – overall heat transfer coefficient, W/(m^{2}K)
Nu – Nusselt number
$\dot{Q}$ – heat flow rate, W
R – thermal resistance, K/W
r – channel's cross-section aspect ratio
T – temperature, K

Greek symbols

α – heat transfer coefficient, W/(m^{2}K)
δz – depth of the control volume (along the channel's z axis), m
λ – wall or fluid thermal conductivity, W/(mK)
η – fin efficiency
$\Delta T_{\log}$ – logarithmic mean temperature difference, K

Subscripts

c, h – cold or hot fluid
e – equivalent wall
$i, s, i+s$ – intermediate, side or total intermediate wall
w, fl – wall or fluid conductivity

1 Introduction

Small scale organic Rankine cycle (ORC) installations demand use of miniature and inexpensive heat exchangers. Minichannel heat exchangers may be made of metal, but there is a possibility to use polymers or other formable materials of small thermal conductivity [1]. At the Institute of Fluid Flow Machinery PAS the design and investigation of miniature heat exchangers for application in ORC is carried out. It is planned to test some non-metal materials for operation in ORC installation. In the paper there are presented four 1-dimensional models of the wall thermal resistance in heat exchangers with rectangular minichannels of the same size. Two of these models are presented in [2]. The models were analysed and compared. It is shown that the thermal resistance of metal walls may be neglected. For the walls made of plastics these models show that the optimal wall thickness is relatively small. The models of the wall thermal resistance are used to calculate the overall heat transfer coefficient k in heat exchangers with rectangular minichannels.

General view of a minichannel heat exchanger and considered control volume is presented in Fig. 1.
Heat transfer rate in the control volume is given by the formula:

$$\dot{Q} = \frac{1}{R}\Delta T_{\log} \, . \tag{1}$$

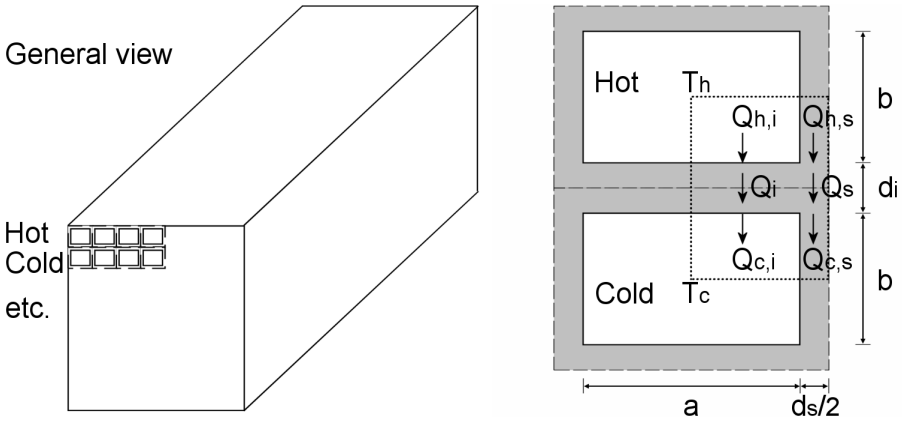

Figure 1: Schematic view of a heat exchanger's cross-section with layers of hot and cold minichannels and of the control volume (dotted line) with heat flows.

Total thermal resistance is given by the overall heat transfer coefficient and heat transfer area of the control volume (in the figure the control volume depth δz is along the channel's z-axis, perpendicular to the figure's plane):

$$R = \frac{1}{kA} \,, \tag{2}$$

where

$$A = \frac{a+b}{2}\delta z \,. \tag{3}$$

Partial thermal resistance are calculated in the same way, for example:

$$R_{h,i} = \frac{1}{\alpha_h A_{h,i}} \,, \tag{4}$$

where

$$A_{h,i} = \frac{a}{2}\delta z \,. \tag{5}$$

Channel's cross-section aspect ratio is defined as

$$r = \frac{a}{b} \,. \tag{6}$$

Hydraulic and thermal diameter is given by

$$d_h = \frac{2ab}{a+b} = \frac{2r}{r+1}b \,. \tag{7}$$

2 Model 1 – no side walls of the channels

First the simplest model is considered where side walls of the channels are removed, Fig. 2.

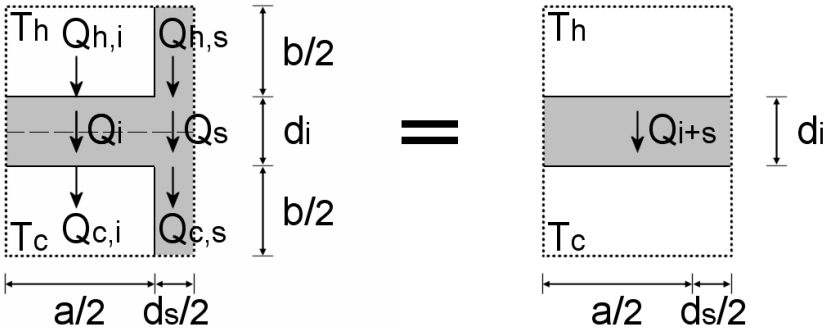

Figure 2: Model 1 – the side walls of the channels are removed.

The formula for total thermal resistance in the models 1 has the form

$$R = R_h + R_{i+s} + R_c \,. \tag{8}$$

Use of (2) and (4) leads to the equation

$$\frac{1}{k_1 \frac{a+b}{2}\delta z} = \frac{1}{\alpha_h \frac{a+d_s}{2}\delta z} + \frac{1}{\frac{\lambda_w}{d_i}\frac{a+d_s}{2}\delta z} + \frac{1}{\alpha_c \frac{a+d_s}{2}\delta z} \,, \tag{9}$$

which gives the final formula for overall heat transfer coefficient k_1:

$$\frac{1}{k_1} = \frac{r+1}{r+d_s/b}\left(\frac{1}{\alpha_c} + \frac{1}{\lambda_w/d_i} + \frac{1}{\alpha_c}\right) \,. \tag{10}$$

3 Model 2 – walls are replaced by an equivalent wall of the same volume and area

In model 2 the walls are represented by an equivalent wall of the same volume and area, Fig. 3. The formula (8), by use of (2) and (4), has the following form in this model

$$\frac{1}{k_2 \frac{a+b}{2}\delta z} = \frac{1}{\alpha_h \frac{a+b}{2}\delta z} + \frac{1}{\frac{\lambda_w}{d_e}\frac{a+b}{2}\delta z} + \frac{1}{\alpha_c \frac{a+b}{2}\delta z} \,, \tag{11}$$

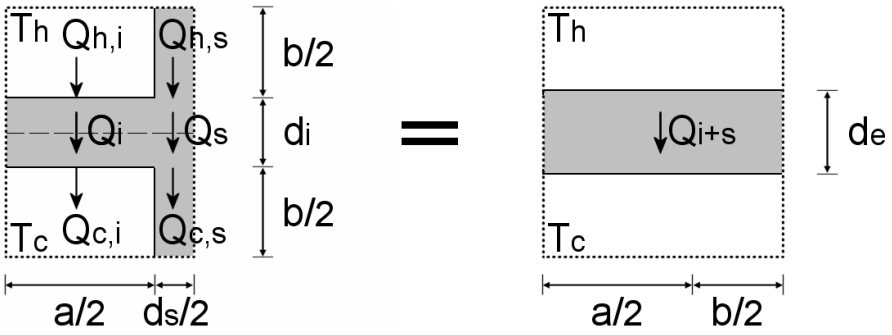

Figure 3: Model 2 – the walls are replaced by an equivalent wall of the same volume and area.

with the equivalent wall thickness

$$d_e = \left(\frac{a+d_s}{2}d_i + 2\frac{d_s}{2}\frac{b}{2}\right)/\frac{a+b}{2} = \frac{(r+d_s/b)d_i + d_s}{r+1}\,. \tag{12}$$

Simplification of (11) gives the final formula for k_2:

$$\frac{1}{k_2} = \frac{1}{\alpha_c} + \frac{1}{\lambda_w/d_e} + \frac{1}{\alpha_c}\,. \tag{13}$$

4 Model 3 – side walls as fins, one common resistance of the wall between hot and cold channels

In this model heat transfer through the intermediate and side walls of the channels are taken separately into account whereas side walls are treated as fins. However, heat flows through the wall between hot and cold channels are not separated, Fig. 4. The formula for the total thermal resistance in the model 3 has the form

$$R = (1/R_{h,i} + 1/R_{h,s})^{-1} + R_{i+s} + (1/R_{c,i} + 1/R_{c,s})^{-1}\,. \tag{14}$$

Use of (2) and (4) leads to the equation

$$\frac{1}{k_3\frac{a+b}{2}\delta z} = \frac{1}{\alpha_h\frac{a+\eta_h b}{2}\delta z} + \frac{1}{\frac{\lambda_w}{d_i}\frac{a+d_s}{2}\delta z} + \frac{1}{\alpha_c\frac{a+\eta_c b}{2}\delta z}\,, \tag{15}$$

with fin efficiency given by (B is introduced later)

$$\eta = \frac{\tanh\left(\sqrt{\frac{\alpha b}{2\lambda_w}\frac{b}{d_s}}\right)}{\sqrt{\frac{\alpha b}{2\lambda_w}\frac{b}{d_s}}} = \frac{\tanh\left(\sqrt{B\frac{b}{d_s}}\right)}{\sqrt{B\frac{b}{d_s}}}\,, \tag{16}$$

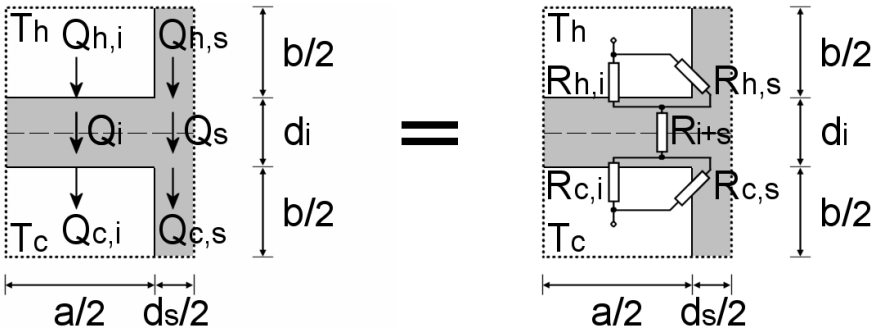

Figure 4: Model 3 – separated thermal resistances: channel side walls are treated as fins, one single common resistance of the wall between hot and cold channels.

Simplification of (15) gives the final formula for k_3:

$$\frac{1}{k_3} = \frac{1}{\alpha_h \frac{r+\eta_h}{r+1}} + \frac{1}{\frac{\lambda_w}{d_i}\frac{r+d_s/b}{r+1}} + \frac{1}{\alpha_c \frac{r+\eta_c}{r+1}} \,. \tag{17}$$

5 Model 4 – side walls as fins, two separate resistances of the wall between hot and cold channels

In this model heat flows through the intermediate and side wall of the channels are taken separately into account whereas side walls are treated as fins. Heat flows through the wall between hot and cold channels are also separated into two parts, Fig. 5. The formula for the total thermal resistance in the model 4 has the form

$$R^{-1} = (R_{h,i} + R_i + R_{c,i})^{-1} + (R_{h,s} + R_s + R_{c,s})^{-1} \,. \tag{18}$$

Use of (2) and (4) leads to the equation:

$$k_4 \frac{a+b}{2}\delta z = \left(\frac{1}{\alpha_h a/2 \cdot \delta z} + \frac{1}{\lambda_w/d_i \cdot a/2 \cdot \delta z} + \frac{1}{\alpha_c a/2 \cdot \delta z}\right)^{-1} + \\ + \left(\frac{1}{\alpha_h \eta_h b/2 \cdot \delta z} + \frac{1}{\lambda_w/d_i \cdot d_s/2 \cdot \delta z} + \frac{1}{\alpha_c \eta_c b/2 \cdot \delta z}\right)^{-1} \,. \tag{19}$$

Simplification of (19) gives the final formula for k_4:

$$k_4 = \frac{r}{r+1}\left(\frac{1}{\alpha_h} + \frac{1}{\lambda_w/d_i} + \frac{1}{\alpha_c}\right)^{-1} + \frac{1}{r+1}\left(\frac{1}{\alpha_h \eta_h} + \frac{1}{\lambda_w/d_i \cdot d_s/b} + \frac{1}{\alpha_c \eta_c}\right)^{-1} \,. \tag{20}$$

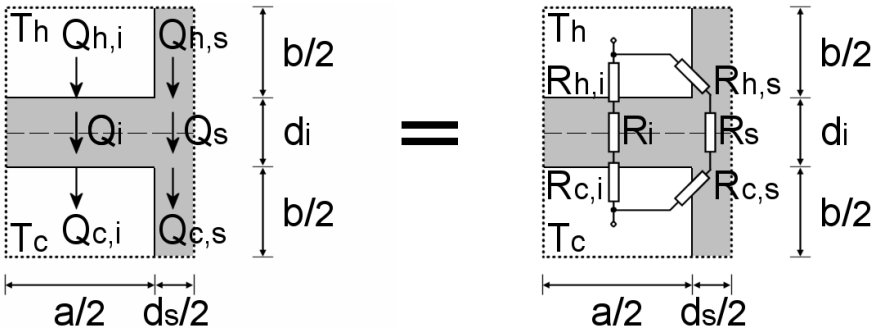

Figure 5: Model 4 – separated thermal resistances, channel side walls are treated as fins, two resistances of the intermediate and side parts of the wall between hot and cold channels.

6 Models analysis and comparison

Obtained values of the overall heat transfer coefficient k are compared to the maximum value k_{MAX} (present for wall thermal resistance equal zero):

$$\frac{1}{k_{MAX}} = \frac{1}{\alpha_h} + \frac{1}{\alpha_c} \,. \tag{21}$$

It is assumed in this analysis that the channel size and heat transfer coefficients α_h, α_c remain constant. The only change of the overall heat transfer coefficient k is caused by the changes of wall thickness d_i, d_s. The common case of equal d_i and d_s is assumed:

$$d = d_i = d_s \,. \tag{22}$$

Heat transfer coefficient α of fluid flow can be calculated from the Nusselt number:

$$\mathrm{Nu} = \frac{\alpha d_h}{\lambda_{fl}} \,. \tag{23}$$

As an example, for fully developed laminar flow Nusselt number depends on the cross-section aspect ratio only and for $r = 1$ (square minichannels) $\mathrm{Nu} = 3.608$ [3,4].

There are two limiting cases of heat transfer coefficients α_h, α_c:

- $\alpha = \alpha_h = \alpha_c$ (both the same single-phase flows), which gives $k_{MAX} = \alpha/2$,

- $\alpha = \alpha_h, \alpha_c \to \infty$ (single-phase and two-phase flow with phase change), which gives $k_{MAX} = \alpha$.

The actual value of k_{MAX} lays between these two bounds

$$\frac{\alpha}{2} \leq k_{MAX} \leq \alpha \, . \tag{24}$$

For each model the quotient k/k_{MAX} is analysed for these two limiting cases.

A dimensionless coefficient B appears in the remaining part of the analysis as

$$B = \frac{\alpha b}{2\lambda_w} = \mathrm{Nu}\frac{\lambda_{fl}}{\lambda_w}\frac{r+1}{4r} \, . \tag{25}$$

This coefficient represents properties of the wall material, fluid, channels geometry and fluid flows. For fixed cross-section aspect ratio the coefficient B depends on the ratio of fluid and wall thermal conductivities only. The examples of B are presented in Tab. 1.

Table 1: Examples of coefficient B for square minichannels ($r = 1$), laminar flow ($\mathrm{Nu} = 3.608$).

No.	Wall material	Fluid	λ_w [W/mK]	λ_{fl} [W/mK]	B [–]
1	copper	water	380	0.60	0.00285
2	copper	ethanol	380	0.17	0.000807
3	stainless steel	water	16.3	0.60	0.0664
4	stainless steel	ethanol	16.3	0.17	0.0188
5	ceramics	water	1.0	0.60	1.08
6	ceramics	ethanol	1.0	0.17	0.307
7	PE high density	water	0.45	0.60	2.41
8	PE high density	ethanol	0.45	0.17	0.682
9	PTFE (Teflon)	water	0.27	0.60	4.00
10	PTFE (Teflon)	ethanol	0.27	0.17	1.14

CASE 1 $\alpha = \alpha_H = \alpha_C$. For each model k/k_{MAX} as a function of B and relative wall thickness d/b is defined:

$$\frac{k_1}{k_{MAX}} = \frac{r + d/b}{r+1}\frac{1}{1 + Bd/b} \, , \tag{26}$$

$$\frac{k_2}{k_{MAX}} = \frac{1}{1+\frac{r+1+d/b}{r+1}Bd/b}\,, \tag{27}$$

$$\frac{k_3}{k_{MAX}} = \frac{r+\eta}{r+1}\frac{1}{1+\frac{r+\eta}{r+d/b}Bd/b}\,, \tag{28}$$

$$\frac{k_4}{k_{MAX}} = \frac{r}{r+1}\frac{1}{1+Bd/b} + \frac{\eta}{r+1}\frac{1}{1+B\eta}\,. \tag{29}$$

In Figs. 6–9 calculation results of k/k_{MAX} vs. relative wall thickness d/b for the flow in square minichannels ($r = 1$, Nu $= 3.608$) are shown.

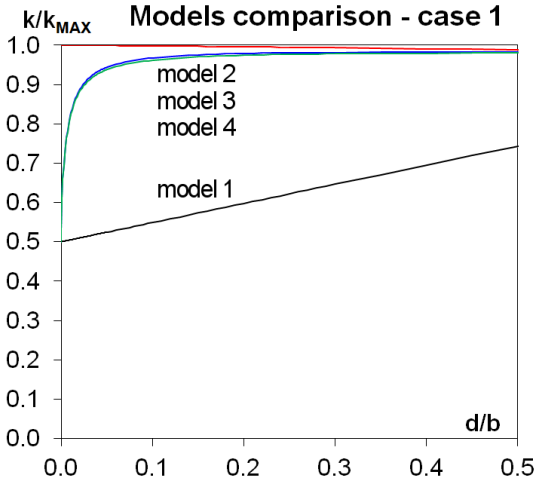

Figure 6: Models comparison for stainless steel and ethanol, $B = 0.0188$.

CASE 2 $\alpha = \alpha_H$, $\alpha_C \to \infty$

For each model k/k_{MAX} as a function of B and relative wall thickness d/b is defined:

$$\frac{k_1}{k_{MAX}} = \frac{r+d/b}{r+1}\frac{1}{1+2Bd/b}\,, \tag{30}$$

$$\frac{k_2}{k_{MAX}} = \frac{1}{1+\frac{r+1+d/b}{r+1}2Bd/b}\,, \tag{31}$$

$$\frac{k_3}{k_{MAX}} = \frac{r+\eta}{r+1}\frac{1}{1+\frac{r+\eta}{r+d/b}2Bd/b}\,, \tag{32}$$

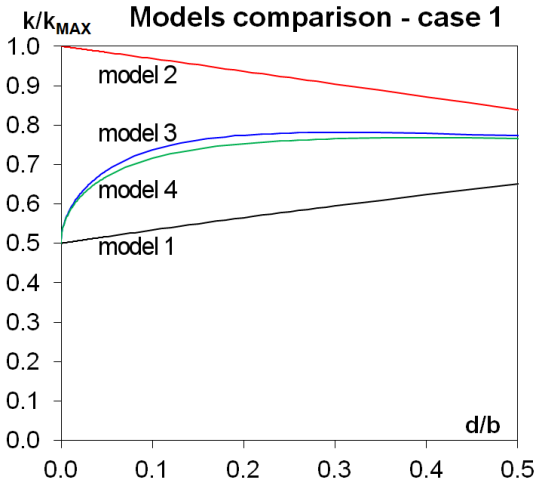

Figure 7: Models comparison for ceramics steel and ethanol, $B = 0.307$.

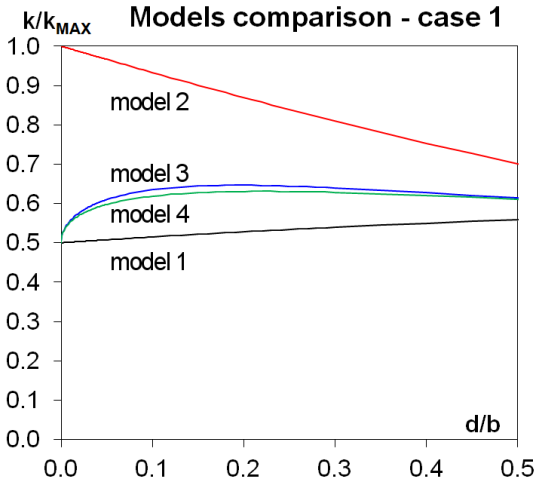

Figure 8: Models comparison for high density PE (polyethylene) and ethanol, $B = 0.682$.

$$\frac{k_4}{k_{MAX}} = \frac{r}{r+1}\frac{1}{1+2Bd/b} + \frac{\eta}{r+1}\frac{1}{1+2B\eta} \,. \tag{33}$$

It is easy to see that coefficient B is replaced by $2B$ in each formula of this case.

In Figs. 10–13 calculation results of k/k_{MAX} vs. relative wall thickness d/b for the flow in square minichannels ($r = 1$, Nu $= 3.608$) are presented.

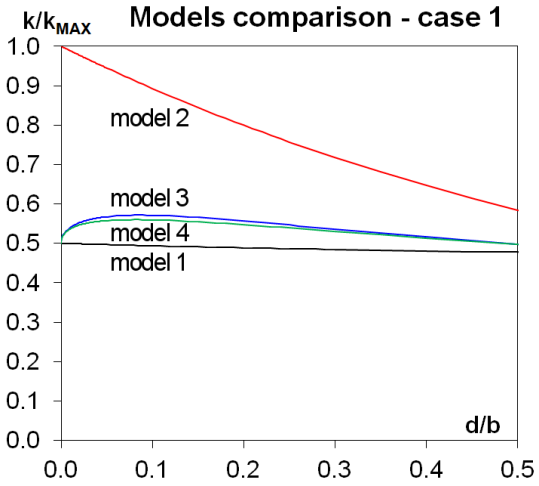

Figure 9: Models comparison for PTFE (teflon) and ethanol, $B = 1.14$.

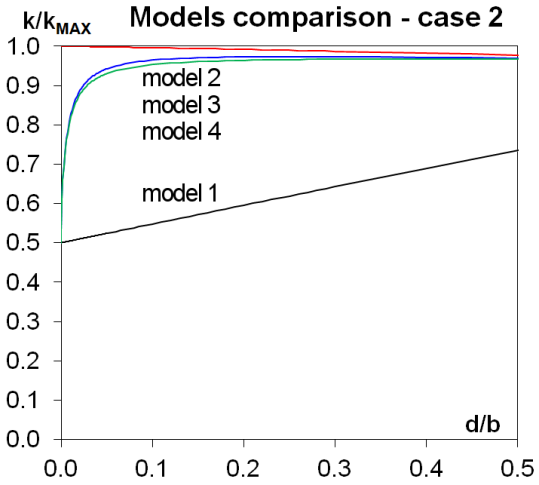

Figure 10: Models comparison for stainless steel and ethanol, $B = 0.0188$.

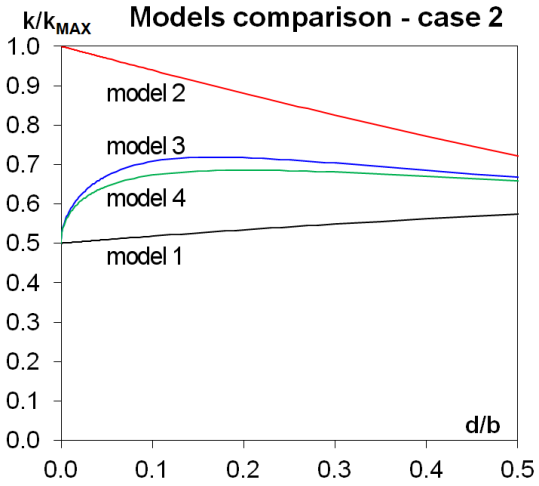

Figure 11: Models comparison for ceramics steel and ethanol, $B = 0.307$.

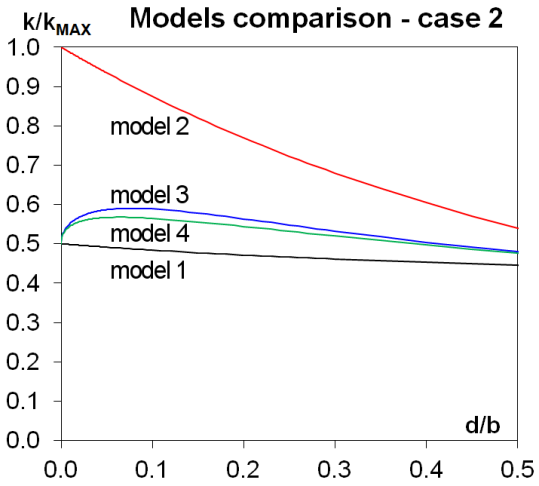

Figure 12: Models comparison for high density PE (polyethylene) and ethanol, $B = 0.682$.

7 Discussion

Among the analysed models the most advanced are the models 3 and 4 and they give the reference results. However they are still 1-dimensional, which means that from the physical point of view, the wall material has anisotropic thermal conductivity: finite in the vertical direction and infinite

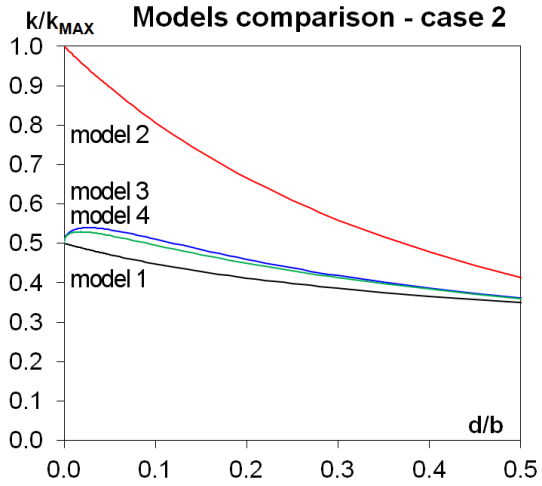

Figure 13: Models comparison for PTFE (teflon) and ethanol, $B = 1.14$.

in the horizontal one. Since this artificial material has better thermal conductivity then the real one, the 1-dimensional models overestimate values of the overall heat transfer coefficient k.

Every realistic model used for $d/b \to 0$ should give the result

$$\lim_{d/b \to 0} \frac{k}{k_{MAX}} = \frac{a}{a+b} = \frac{r}{r+1} \,. \tag{34}$$

This universal result reflects the fact that infinite thin side walls do not conduct heat. For the exemplary value $r = 1$ this limit is equal to $1/2$. Model 2 does not respect this result and does not give correct results, Figs. 6–13. Model 1 gives rough approximation of the results from models 3 and 4 for bad heat conductors like PTFE (teflon), Figs. 9 and 13, used in so called polymer heat exchangers [1]. Model 1 may be used for these materials, but the results are always slightly underestimated in comparison with models 3 and 4. Model 4 always gives lower results of the overall heat transfer coefficient then model 3. Model 3 is more flexible than model 4 because of using single common thermal resistance R_{i+s} of the wall between hot and cold minichannels instead of separate R_i and R_s in model 4. Use of single R_{i+s} makes possible generalization of model 3 to the case of nonequal size of hot and cold minichannels (nonequal heat transfer area A_h and A_c).

Metal walls give very little thermal resistance even for relatively bad conductive stainless steel, Figs. 6 and 10. Use of typical better thermal

conductors: brass, aluminium or copper makes wall thermal resistance negligible. For worse thermal conductors (plastics) the optimal wall thickness should be calculated.

Models 3 and 4 show the existence of optimal relative wall thickness d/b maximizing k/k_{MAX}. The optimal value of d/b is calculated by use of the condition

$$\frac{d}{d(d/b)}\left(\frac{k}{k_{MAX}}\right) = 0\ . \tag{35}$$

The examples of optimal values of d/b for the cases 1, 2 are presented in Tab. 2.

Table 2: Optimal relative thickness d/b and k/k_{MAX} for the cases 1 and 2 of model 3.

No.	Wall material	Fluid	B [–]	Case 1		Case 2	
				$(d/b)_{OPT}$ [–]	$(k/k_{MAX})_{OPT}$ [–]	$(d/b)_{OPT}$ [–]	$(k/k_{MAX})_{OPT}$ [–]
1	copper	water	0.00285	0.405	0.997	0.256	0.996
2	copper	ethanol	0.000807	0.406	0.9992	0.256	0.9988
3	stainless steel	water	0.0664	0.384	0.939	0.237	0.914
4	stainless steel	ethanol	0.0188	0.400	0.982	0.251	0.973
5	ceramics	water	1.08	0.0971	0.578	0.0301	0.543
6	ceramics	ethanol	0.307	0.306	0.782	0.169	0.719
7	PE high density	water	2.41	0.0141	0.520	0.00388	0.510
8	PE high density	ethanol	0.682	0.192	0.646	0.0775	0.590
9	PTFE (teflon)	water	4.00	0.00352	0.508	0.000923	0.504
10	PTFE (teflon)	ethanol	1.14	0.0869	0.571	0.0265	0.540

The optimal values of d/b are fortunately small for bad thermal conductors, and the optimal side walls may still be treated as thin fins. In practice, the relative wall thickness d/b should not be too small and should lay in the range 0.05–0.15 [1].

Worse thermal conductivity of nonmetal walls may be compensated by higher number of minichannels. In the case of PTFE – teflon and ethanol

($B = 1.14$) the optimal k/k_{MAX} is equal to 0.571 and 0.540 only, respectively in the case 1 and 2. To compensate this, the heat transfer area should be increased by $1/0.571 = 1.75$ or $1/0.540 = 1.85$ respectively. However the side of the heat exchanger's square cross-section will be increased by smaller factors: $\sqrt{1.75} = 1.32$ or $\sqrt{1.85} = 1.36$ respectively. If higher number of minichannels may be accepted, the use of plastic instead of metal significantly decreases production costs.

8 Conclusions

- Four 1-dimensional models of thermal resistance of walls in a heat exchanger with rectangular minichannels were derived and analysed.
- Model 3 is recommended. It takes side walls into account as fins and uses single thermal resistance between layers of hot and cold minichannels. This model may be easily generalized to the case of non-equal hot and cold minichannels.
- Metal minichannel walls have negligible thermal resistance.
- The simplest model 1 may be used for plastic walls of bad thermal conductivity.
- The optimal wall thickness was derived for walls made of plastics.
- Mininichannel heat exchangers made of plastics are moderately bigger. However their production costs may be significantly lower, what is important in foreseen mass production of ORC installations used in domestic combined heat and power (CHP) technologies.

Received 23 June 2015

References

[1] Cevallos J.G., Bergles A.E., Bar-Cohen A., Rodgers P., Gupta S.K.: *Polymer Heat Exchangers – History, Opportunities, and Challenges.* Heat Transfer Eng. **33**(2012), 13, 1075–1093.

[2] Mikielewicz D. et al.: *Selected topics of design and investigation of heat exchangers for ORC in a domestic CHP.* IFFM PAS Publishers, Gdańsk 2013 (in Polish).

[3] Rybiński W., Mikielewicz J.: *Analytical solutions for laminar flow exchanging heat in rectangular channels.* Arch. Thermodyn. **35**(2014), 4, 29–42.

[4] Shah R.K., London A.L.: *Laminar flow forced convection in ducts.* Academic Press, New York 1978.

archives
of thermodynamics
Vol. **37**(2016), No. 3, 79–93
DOI: 10.1515/aoter-2016-0021

Experimental investigation of domestic micro-CHP based on the gas boiler fitted with ORC module

JAN WAJS *
DARIUSZ MIKIELEWICZ
MICHAŁ BAJOR
ZBIGNIEW KNEBA

Gdansk University of Technology, Faculty of Mechanical Engineering, Department of Energy and Industrial Apparatus, Narutowicza 11/12, 80-233 Gdańsk, Poland

Abstract The results of investigations conducted on the prototype of vapour driven micro-CHP unit integrated with a gas boiler are presented. The system enables cogeneration of heat and electric energy to cover the energy demand of a household. The idea of such system is to produce electricity for own demand or for selling it to the electric grid – in such situation the system user will became the prosumer. A typical commercial gas boiler, additionally equipped with an organic Rankine cycle (ORC) module based on environmentally acceptable working fluid can be regarded as future generation unit. In the paper the prototype of innovative domestic cogenerative ORC system, consisting of a conventional gas boiler and a small size axial vapour microturbines (in-house designed for ORC and the commercially available for Rankine cycle (RC)), evaporator and condenser were scrutinised. In the course of study the fluid working temperatures, rates of heat, electricity generation and efficiency of the whole system were obtained. The tested system could produce electricity in the amount of 1 kWe. Some preliminary tests were started with water as working fluid and the results for that case are also presented. The investigations showed that domestic gas boiler was able to provide the saturated/superheated ethanol vapour (in the ORC system) and steam (in the RC system) as working fluids.

Keywords: Micro-CHP; Organic Rankine cycle; Prototype domestic unit

*Corresponding Author. E-mail: janwajs@pg.gda.pl

Nomenclature

$\dot{m}$	–	mass flux, g/s
N	–	electric power, kW
P	–	pressure, Pa
$\dot{Q}$	–	rate of heat, kW
t	–	temperature, °C
x	–	quality
CHP	–	combined heat and power
C-R	–	Clausius-Rankine cycle
kWe	–	kW of electric power
ORC	–	organic Rankine cycle
RC	–	Rankine cycle

Greek symbols

η	–	efficiency, %

Subscripts

b	–	exergy
C	–	Carnot
el	–	electric
et	–	ethanol
in	–	inlet
out	–	outlet
t	–	thermal
T	–	turbine
w	–	water

1 Introduction

In recent years there is observed a tendency to increase the importance of so called dispersed generation, based on the local energy sources and the working systems utilizing both the fossil fuels and the renewable energy resources. Generation of electricity on a small domestic scale together with production of heat can be obtained through employment of the technologies like gas engine units, gas microturbines, fuel cells with efficient electrolysis, Stirling engines or the organic Rankine cycle (ORC) systems. All of them are mentioned in the European Union directive 2012/27/EU [1] for cogenerative production of heat and electricity. It is worth noting that practical realization of the Rankine cycle (RC) or ORC technology in a microscale (the electrical power production below 10 kWe) is kind of technical challenge. Such unit must be equipped with small size turbine (expansion machine) and highly efficient and compact heat exchangers.

With an increase in demand for various energy carriers, there arises a noticeable trend in the search for new forms of electricity production. In recent years, energy production tends to the distributed energy based on local energy sources and technologies using fossil fuels and renewable energy sources. One way to improve the efficiency of these sources usage is an autonomous energy production in the form of electricity and heat in individual households. Such a solution could also increase energy security for households due to the generation of electricity at the point of consumption. The cogeneration ORC technology is promoted by the legislative bodies of the European Union what could be found in Directive [1], which is also consistent with the national strategy of sustainable development [2].

In general, the operation of system implementing ORC follows the fundamental principles of the classic Clausius-Rankine (C-R) cycle. The main difference between these two cycles is in the working fluid. In the case of ORC the working fluid is an organic compound instead of water which is used in the classical Rankine cycle. In combined heat and power (CHP) systems based on organic fluids, their operating temperatures and pressures are lower than in the case of conventional steam C-R systems. Therefore, from the thermal point of view, the ORC technology is more safe for users than C-R systems, especially in the light of households' applications. These systems will be also able to partially cover the residential buildings demand for electricity. Moreover, it will allow better utilization of the fuel, reduction of the emissions. Examples of microcogeneration solutions are a gas engine [3], gas microturbine [4], fuel cells with efficient electrolysis [5], Stirling engine [6], or a system with the use of ORC technology [7–11].

To meet the expectations posed by the energy future of small-scale applications, authors attempted to dedvelop a prototype unit for the cogeneration of electricity and heat to cover the needs of individual households. The idea of this system operation was based on the ORC (with ethanol as working fluid) cooperating with a gas boiler with a thermal power of 25 kW as an autonomous source of heat [12]. The experimental investigations of the precursory version of such unit with ethanol and HFE-7100 (methoxynonafluorobutane, $C_4F_9OCH_3$) as the working fluids were reported in [13].

This paper provides a summary of the construction and commissioning of the demonstration prototype of micro-CHP. In the authors opinion the prototype bears the signs of innovation due to the compactness of the unit, its mobility and dedicated solutions of heat exchangers such as evaporator and condenser. Additionally, the authors attempted to modify the micro-

CHP that it can operate as a low-temperature Rankine cycle. In this paper some preliminary results are also presented.

2 Prototype domestic CHP

For the prototype of domestic CHP, the ORC system is a kind of the add-on module for a gas boiler DTG X 23 N [12], which in the commercial version is offered by De Dietrich company to the domestic market. This kind of boiler has been modified by the authors to operate with thermal oil as heat carrier and subsequently tested at the high temperatures [12]. The schematic of a laboratory facility is shown in Fig. 1. Axonometric view of the micro demonstration ORC installation with the gas boiler is shown in Fig. 2a. The overall view of the facility is presented in the photograph in Fig. 2b.

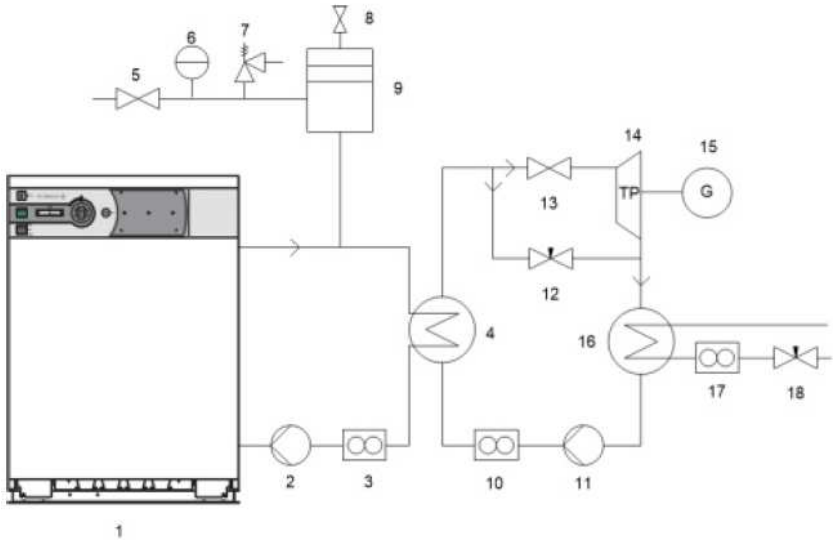

Figure 1: Schematic of the laboratory installation: 1 – gas boiler, 2 – oil circulation pump, 3 – oil flow meter, 4 – evaporator, 5,8,13,18 – ball valve, 6 – manometer, 7 – safety valve, 9 – compensation vessel, 10 – mass flow meter, 11 – pump of working fluid, 12 – throttle valve, 14 – expander, 15 – alternator, 16 – condenser, 17 – water flow meter.

Following, a brief description of the facility operational principles are presented – notation used in the description corresponds to the indicators marked in Fig. 1. As previously mentioned, an autonomous source of heat

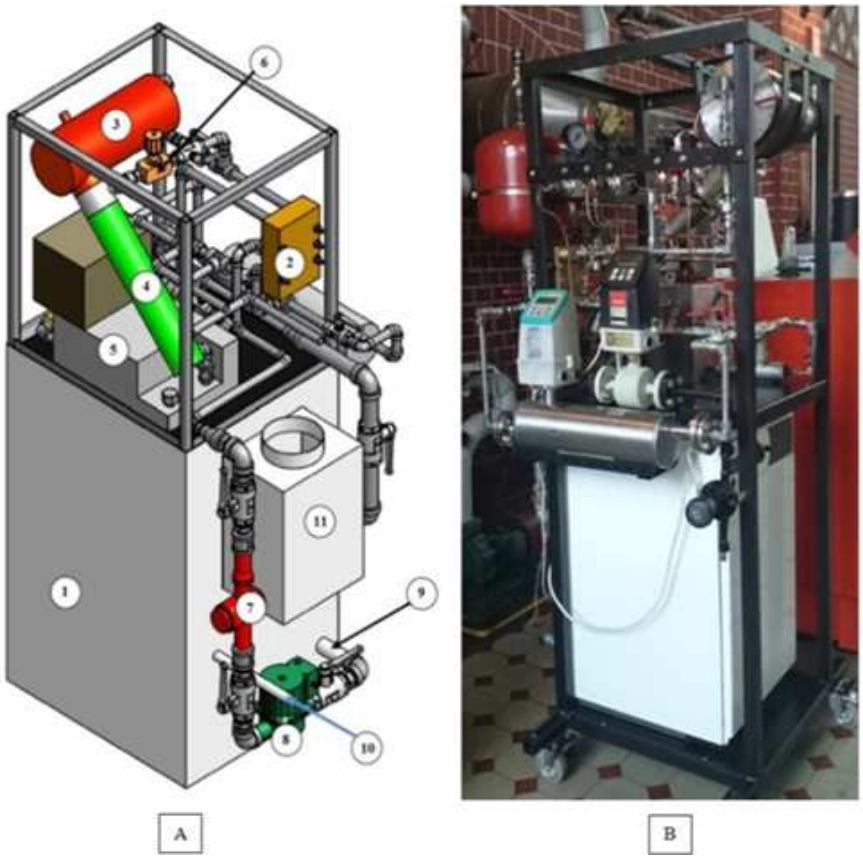

Figure 2: (A) Micro-CHP – axonometric view: 1- gas boiler, 2 – evaporator, 3 – turbo-generator, 4 – condenser, 5 – tank with ethanol, 6 – throttle valve, 7 – oil flow meter, 8 – oil circulating pump, 9 – inlet oil, 10 – gas connector, 11 – exhaust; (B) overview of micro-CHP with gas boiler.

for the ORC was the domestic gas boiler (1) in which the chemical energy of the fuel (natural gas) was converted into thermal energy received by thermal oil. Oil is an intermediate heat transfer medium circulating in a closed loop between the boiler and evaporator (2) of vapour cycle with working fluid (ethanol-ORC, H_2O-RC). Oil circulation in the loop was ensured by the circulation pump (8) with a maximum capacity of 3.5 m^3/h and a maximum head of 6 m. Vane flow meter (7) was used to measure the volumetric flow of oil. Circulation of ethyl alcohol/H_2O in a closed loop of ORC/RC module was provided by a hermetic gear pump with magnetic

coupling of a nominal capacity of 0.4 m^3/h at a differential pressure of 1.03 MPa. The adjustment of the pump's efficiency was possible by changing the frequency, or by using a manually operated throttle valve - installed in the form of 'by-pass'. Coriolis mass flow meter with signal converter was used to measure the flow of ethanol/H_2O. Working fluid passing through the evaporator received heat energy from the thermal oil and evaporated to reach the state of superheated vapour with applied appropriate heat flux. Saturated/superheated vapour was ultimately directed to the turbine (3), where it expanded and then flowed to the condenser (4). During the facility start-up phase the turbine was bypassed by the throttling valve (6) to obtain required vapour parameters. After that the valve was closed. The condenser was cooled by tap water. After the condensation process, the condensate was turned back to the reservoir (5).

De Dietrich gas boiler DTG X 23 N featured the open combustion chamber, electronic ignition with ionisation flame control, atmospheric burner able to burn all kinds of natural gas and liquefied petroleum gas. In addition to the main burner, boiler was also equipped with an ignition burner, which enabled 'soft' (inexplosive) start of the main burner. The boiler's body was made of thermally shocked and corrosion-resistant eutectic cast iron.

During the test stage of assembled facility, function of the evaporator was performed by the in-house design and manufacture of the shell and tube heat exchanger, with circular minitubes [14]. The function of condenser was also performed by the shell and tube heat exchanger with minitubes – the mirror structure of the evaporator.

ORC turbine was connected with the condenser by means of a flexible compensator providing the damping in the system. The vapour microturbine equipped with the alternator was designed and constructed for the needs of prototype micro-CHP, with ethanol as the working fluid. The electric generator was mounted on the turbine shaft, directly behind its low pressure part. The turbine and generator had then the common casing, Fig. 3. The rotor disk is shown in Fig. 4.

Described micro-turbogenerator had following features:

- electrical power output 1.8–1.9 kW,
- rotational speed of rotor $n \approx 36000$ rpm,
- mass flow rate of ethanol 24 g/s,
- vapour pressure at the turbine inlet, 0.7 MPa,
- the Mach number at the blade cascade output, Ma ≈ 2.4,

- oil-free technology for the bearing system design.

Figure 3: View of vapour ORC microturbine.

Figure 4: Turbine rotor disk with generator rotor.

In the next step of studies the authors challenged to create the domestic CHP cooperated with the classical steam cycle (Rankine Cycle) with water as the working fluid. This required the replacement of the turbogenerator. A unit available on the market, dedicated to a steam at low temperature was used. The turbine with generator is presented in Fig. 5. Applied steam turbine had two stages with separate generators. The nozzle disk of microturbine 1st stage is shown in Fig. 6. Nominal operating parameters of turbine were [15]:

- inlet steam pressure: 0.052 MPa,
- inlet steam temperature: 200 °C,
- outlet steam pressure: 0.01 MPa,
- nominal power: 1.2 kW,
- steam consumption: 5 g/s,

- design rotational speed: 30 000 rpm.

Figure 5: View of microturbine in RC application.

Figure 6: Nozzle disc of microturbine 1st stage.

3 Experimental analysis

3.1 Ethanol system

On the basis of theoretical analysis and previous experimental studies the dehydrated ethyl alcohol was selected as a working fluid for the ORC module [16]. Its physical properties necessary for the thermal calculations, were taken from REFPROP 9.0 [17].

In the first stage of experimental analysis the cooperation of a gas boiler with the ORC module, supporting the start-up of the demonstrative station was verified. It was followed by the studies of installed in the ORC module heat exchangers (evaporator and condenser) performance. In this case, the expansion valve was simulating the action of the expander. The results of this stage investigations were reported by authors in [18]. For better transparency they are also recalled below. Thus the results of measurements and calculations for the evaporator in Tab. 1 and results for the condenser are summarized in Tab. 2. In addition to the list of mass flow rate, temperature and pressure, in the tables are also presented the heat exchanger performance and quality of ethanol, x, at the outlet of the evaporator (Tab. 1) and at the inlet to the condenser, i.e., after the throttle valve (Tab. 2).

Table 1: Micro-ORC evaporator energy balance.

No.	Thermal oil				Ethanol				
Parameter	$\dot{m}_{oil}$	t_{in}	t_{out}	$\dot{Q}_{oil}$	$\dot{m}_{et}$	t_{in}	t_{out}	P	x
Units	g/s	°C	°C	kW	g/s	°C	°C	MPa	–
1	297	167.0	142.0	17.66	20	42.4	119.0	0.415	0.858
2	267	164.5	138.5	16.41	20	38.1	116.4	0.380	0.835
3	369	159.0	139.0	17.43	20	49.8	116.1	0.386	0.847
4	352	159.0	138.6	16.97	16	53.3	115.1	0.370	0.998
5	287	162.0	137.7	16.47	17	51.7	114.8	0.359	0.974
6	258	165.5	138.2	16.66	18	49.8	115.0	0.365	0.910
7	201	173.5	139.1	16.45	18	50.4	115.0	0.370	0.921
8	171	178.5	140.3	15.81	18	51.3	115.2	0.372	0.884
9	151	183.8	140.9	15.50	18	51.4	114.8	0.363	0.894
10	146	187.4	145.1	14.95	15	50.2	120.6	0.440	0.997
11	141	193.5	149.5	15.14	15	46.6	126.1	0.511	0.998

At this stage of study it was demonstrated that the adapted boiler could produce saturated vapour of ethyl alcohol with a dryness factor (quality) close to unity, when the mass flow was in the range from 15 to 20 g/s and a pressure in the range 0.36–0.51 MPa, which corresponded to the saturation temperature in the range 115–126 °C. These results served as the basis for the experiment second stage – system operation with microturbine

Table 2: Micro-ORC condenser energy balance.

No.	Ethanol					Water			
Parameter	$\dot{m}_{et}$	t_{in}	P	x	t_{out}	$\dot{m}_w$	t_{in}	t_{out}	$\dot{Q}_w$
Units	g/s	°C	MPa	–	°C	g/s	°C	°C	kW
1	20	86.2	0.135	0.846	38.7	100	12.4	52.8	16.98
2	20	85.4	0.133	0.804	39.4	91	12.4	55.0	16.22
3	20	88.6	0.151	0.811	50.4	70	12.8	68.7	16.35
4	16	88.6	0.149	0.985	45.0	70	13.1	66.9	15.80
5	17	88.2	0.149	0.943	44.3	71	13.2	66.2	15.63
6	18	88.2	0.149	0.871	45.9	70	13.5	66.1	15.39
7	18	88.5	0.149	0.899	46.8	70	13.6	67.5	15.76
8	18	88.6	0.151	0.876	46.5	70	13.7	66.7	15.44
9	18	88.4	0.149	0.868	45.5	70	13.7	66.2	15.36
10	15	87.6	0.144	0.981	39.9	70	13.7	63.3	14.58
11	15	87.0	0.142	0.976	40.1	70	13.7	62.5	14.34

instead of the expansion valve. All components of the system remaining in high-temperature area were covered with thermal insulation to reduce heat losses.

Measurements of physical quantities done during the ORC module working, allowed the calculations of following parameters: rate of heat received by the working medium (ethanol) in the evaporator, $\dot{Q}_{in}$, rate of heat in the cooling water in the condenser, $\dot{Q}_{out}$, generation of electric power, N_{el}, internal efficiency of the turbine, η_{iT}, theoretical efficiency of implemented thermodynamic cycle, η_t, maximum efficiency, i.e., Carnot cycle efficiency in the min/max working temperature, η_C, and exergy efficiency, η_b. The results of measurements and calculations are summarized in Tab. 3. The table additionally features: the mass flow rates of ethanol, temperature and pressure, the quality of ethyl alcohol vapour, x_{T_exit}, at the turbine's outlet.

3.2 Steam system

For the modified micro-CHP adapted to work with steam as the working fluid it was demonstrated that the gas boiler could produce superheated steam within the temperature range of 165–200 °C in the pressure range

Table 3: Measurements and calculations results of ORC module.

$\dot{Q}_{in}$	$\dot{Q}_{out}$	N_{el}	$\dot{m}_{et}$	P_{T_in}	t_{T_in}	P_{T_exit}	x_{T_exit}	η_{iT}	η_t	η_c	η_b
kW	kW	kW	g/s	MPa	°C	MPa	–	%	%	%	%
21.26	19.63	0.66	20	0.573	130.4	1.59	0.98	86.0	6,65	22.53	29,52
21.29	19.19	0.71	20	0.529	129.6	1.53	0.99	82.3	6,10	20.66	29,51
21.48	18.84	0.76	19	0.604	143.2	1.56	– *	81.8	6.40	23.54	27.21

* superheated vapour ($\Delta t_{superheat}$= 4.7 K)

0.45–0.57 MPa, when the mass flow was in the range 4.4–5.8 g/s. For the preliminary test of RC module the following parameters were determined: rate of heat received by steam in the evaporator ($\dot{Q}_{in}$), rate of heat transferred to the cooling water in the condenser ($\dot{Q}_{out}$), generated electric power (N_{el}), internal efficiency of the turbine (η_{iT}), theoretical efficiency of implemented thermodynamic cycle (η_t), maximum efficiency (η_C), and exergy efficiency (η_b). The results of measurements and calculations are summarized in Tab. 4. In that table there are also included: the mass flow rates of steam, the temperature and pressure before/behind the turbine, the quality of steam at the turbine's outlet.

Table 4: Measurements and calculations results of RC module.

$\dot{Q}_{in}$	$\dot{Q}_{out}$	N_{el}	$\dot{m}_{et}$	P_{T_in}	t_{T_in}	P_{T_exit}	x_{T_exit}	η_{iT}	η_t	η_c	η_b
kW	kW	kW	g/s	MPa	°C	MPa	–	%	%	%	%
14.58	12.39	0.92	5.31	0.520	180.6	0.036	0.96	61.9	9.66	36.34	26.59
13.43	10.89	0.84	4.85	0.489	190.4	0.035	0.97	62.1	9.59	37.62	25.49
11.93	10.05	0.78	4.40	0.450	166.4	0.027	0.95	62.2	10.04	33.85	29.67
12.39	10.55	0.88	4.52	0.456	179.3	0.021	0.96	59.8	10.88	35.81	30.38
14.92	12.90	1.00	5.40	0.535	190.8	0.022	0.97	56.2	10.30	37.50	27.47
15.53	13.23	1.04	5.60	0.540	195.4	0.023	0.98	53.4	10.31	38.14	27.04
15.97	14.07	1.08	5.75	0.570	198.4	0.023	0.98	53.4	10.42	38.53	27.05

During the test of RC module the power characteristics of two generators with constant load resistance were determined. The characteristic of attained power versus 1st generator's rotational speed for the applied load resistance of 60 Ω is shown in Fig. 7. The 2nd generator's with load resis-

tance of 131 Ω corresponding characteristic is presented in Fig. 8.

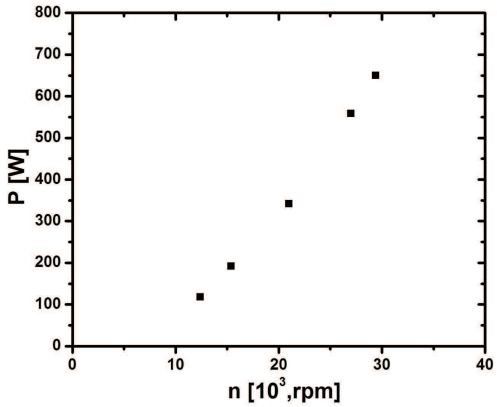

Figure 7: Power characteristics of turbogenerator 1st stage with load resistance of 60 Ω.

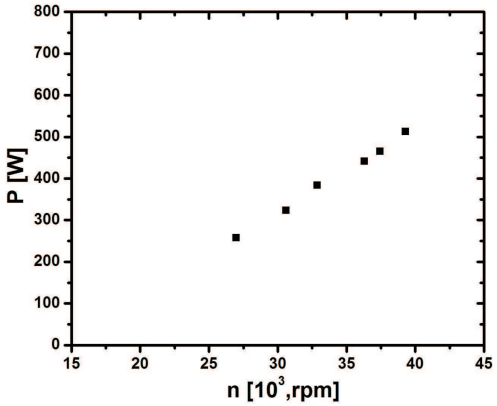

Figure 8: Power characteristics of turbogenerator 2nd stage with load resistance of 131 Ω.

4 Conclusions

This paper presents the prototype of a domestic ORC micropower plant with a gas boiler as an autonomous source of heat. It allows the cogenerative production of thermal energy and electricity in terms of covering the needs for the individual household. The design is innovative due to the

compactness, mobility and original solutions of the evaporator and condenser.

In the course of studies it was demonstrated that the De Dietrich gas boiler allowed generation of ethyl alcohol saturated/superheated vapour of a mass flow rate at the level of 20 g/s at the pressure of 0.6 MPa. Obtained thermal parameters of vapour allowed to run a prototype microturbine and the generation of 760 W electric power.

In addition, the preliminary test proved that the RC module in cooperation with gas boiler was able to produce superheated steam of 5 g/s mass flow rate at the pressure of 0.5 MPa with temperature of about 200 °C. These parameters were sufficient to generate about 1 kW of electric power by the steam turbine. In the authors opinion the commonly available gas boiler is suitable for ORC or RC modules in terms of cogeneration.

Due to the absence of ORC/RC modules casing in micro-CHP unit, the noise analysis was not yet conducted during the turbogenerators operation. This issue will be undertaken, when the prototypes are equipped with soundproof casing. The results will be then compared with European Union directives, dedicated to an evaluation of the heating devices energy efficiency class [19,20].

Proposed solution of combining commercial heat source, which is a gas boiler, with the ORC or RC module can be an interesting alternative for small households. This solution enables simultaneous production of electricity and heat. It should be noted that the production of electricity in the presented installation is only possible if there is demand for thermal energy. The expected period of operation for the installation is mainly the heating season, i.e., the period in which water is prepared for the central heating and for utility purposes. During summer, when the household's demand for heat is reduced, it is possible to apply different renewable energy technologies, such as photovoltaic for the support of ORC module in power generation [21]. Alternatively, in the summer period the ORC system can supply heat to the adsorption refrigeration system, extending in such way the alternativeness of the installation.

Received 2 July 2016

References

[1] *Directive of the European Parliament and of the Council*, 2012/27/UE.

[2] *Resolution of the Council of Ministers No. 202/2009 on the Polish energy policy until 2030* (in Polish).

[3] Muccillo M., Gimelli A.: *Experimental development, 1D CFD simulation and energetic analysis of a 15 kW micro-CHP unit based on reciprocating internal combustion engine*. Appl. Therm. Eng. **71**(2014), 2, 760–770.

[4] Al-attab K.A., Zainal Z.A.: *Performance of a biomass fueled two-stage micro gas turbine (MGT) system with hot air production heat recovery unit*. Appl. Therm. Eng. **70**(2014), 1, 61–70.

[5] Arsalis A., Nielsen M.P., Kaer S.K.: *Modeling and parametric study of a 1 kWe HT-PEMFC-based residential micro-CHP system*. Int. J. Hydrogen Energ. **36**(2011), 8, 5010–5020.

[6] Li T., Tang D.W., Li Z., Du J., Zhou T., Jia Y.: *Development and test of a Stirling engine driven by waste gases for the micro-CHP system*. Appl. Therm. Eng. **33-34**(2012), 1, 119–123.

[7] Yagoub W., Doherty P., Riffat S.B.: *Solar energy-gas driven micro-CHP system for an office building*. Appl. Therm. Eng. **26**(2006), 14-15, 1604–1610.

[8] Qiu K., Hayden A.C.S.: *Integrated thermoelectric and organic Rankine cycles for micro-CHP systems*. Appl. Energ. **97**(2012), 667–672.

[9] Qiu G., Shao Y., Li J., Liu H., Riffat, S.B.: *Experimental investigation of a biomass-fired ORC-based micro-CHP for domestic applications*. Fuel **96**(2012), 374–382.

[10] Mocarski S., Borsukiewicz-Gozdur A.: *Selected aspects of operation of supercritical (transcritical) organic Rankine cycle*. Arch. Thermodyn. **36**(2015), 2, 85–103.

[11] Mikielewicz D., Mikielewicz J., Wajs J.: *Experiences from operation of different expansion devices for application in domestic micro CHP*. Arch. Thermodyn. **31**(2010), 4, 3-13.

[12] Mikielewicz D., Wajs J., Bieliński R.: *Adaptation of a gas boiler to cooperation with thermal oil*. IFFM PASci 578/11, Gdańsk 2011 (in Polish).

[13] Mikielewicz D., Wajs J., Mikielewicz J.: *Gas boiler as a heat source for a domestic micro-CHP*. J. Power Technol. **94**(2014), 4, 317–322.

[14] Wajs J., Mikielewicz, D.: *Minichannel shell and tubes heat exchanger*. Technika Chłodnicza i Klimatyzacyjna **6-7**(2010), 255-259 (in Polish).

[15] Producer data, Green Turbine.

[16] Mikielewicz D., Mikielewicz J.: *A thermodynamic criterion for selection of working fluid for subcritical and supercritical domestic micro CHP*. Appl. Therm. Eng. **30**(2010), 16, 2357-2362.

[17] *Refprop v. 9.0*, National Institute of Standards (NIST), 2010.

[18] Mikielewicz D., Wajs J., Bajor M., Mikielewicz J.: *A commercial gas boiler fitted with the ORC module as perspective solution for households*. In: Proc. XXII Int. Symp. Research-Education-Technology, 4th Int. Conf. Low Temperature and Waste Heat Use in Energy Supply Systems, Bremen, 2015.

[19] Commission Delegated Regulation (EU) No 811/2013 supplements directive 2010/30/EU.

[20] Commission Delegated Regulation (EU) No 813/2013 implements directive 2009/125/EC.

[21] Iimura K., Yamazaki M., Maeno K.: *Results of electrical system and Home Energy Management System for "Omotenashi House" in Solar Decathlon Europe 2012*. Energ. Buildings **83**(2014), 149–161.

archives
of thermodynamics
Vol. **37**(2016), No. 3, 95–108
DOI: 10.1515/aoter-2016-0022

A model of gas flow with friction in a slotted seal

DAMIAN JOACHIMIAK*
PIOTR KRZYŚLAK

Poznan University of Technology, Chair of Thermal Engineering, Piotrowo 3, 60-965 Poznań, Poland

Abstract The paper discusses thermodynamic phenomena accompanying the flow of gas in a slotted seal. The analysis of the gas flow has been described based on an irreversible adiabatic transformation. A model based on the equation of total enthalpy balance has been proposed. The iterative process of the model aims at obtaining such a gas temperature distribution that will fulfill the continuity equation. The model allows for dissipation of the kinetic energy into friction heat by making use of the Blasius equation to determine the friction coefficient. Within the works, experimental research has been performed of the gas flow in a slotted seal of slot height 2 mm. Based on the experimental data, the equation of local friction coefficient was modified with a correction parameter. This parameter was described with the function of pressure ratio to obtain a mass flow of the value from the experiment. The reason for taking up of this problem is the absence of high accuracy models for calculating the gas flow in slotted seals. The proposed model allows an accurate determination of the mass flow in a slotted seal based on the geometry and gas initial and final parameters.

Keywords: Slotted seals; Annular slot; Friction coefficient; Gas flow

Nomenclature

A – flow area, m^2
$\mathbf{B}$ – model matrix

*Corresponding Author. E-mail: damian.joachimiak@put.poznan.pl

$\mathbf{\Delta T}$ – temperature difference vector
$\Delta \dot{\mathbf{m}}$ – mass flow difference vector
C_e – correction parameter of friction coefficient c_f
c_f – friction coefficient
c_p – specific heat, J/kg K
R – gas constant, J/kg K
Re – Reynolds number
T – temperature, K
O – wetted circumference for the gas flow, m
L – length of the seal, m
h – specific enthalpy, J/kg
HS – slot height, m
Δp – pressure drop, Pa
$\dot{m}$ – mass flow, kg/s
p – pressure, Pa
q – heat of friction, J/kg
u – velocity, m/s
x – linear dimension alongside the gas flow, m

Greek symbols

δ – calculations accuracy
κ – isentropic exponent
λ – friction coefficient
Δ – increment of a given parameter
ν – gas kinematic viscosity, m^2/s
ρ – gas density, m^3/kg
τ – static tension, Pa

Subscripts and superscripts

1 – value at the inlet to the seal
2 – value at the outlet of the seal
e – value obtained in the experiment
i – value for the ith element
it – number of iterations
m – value obtained from the model
max – maximum value
n – number of elements
s – value referred to the isentropic transformation
T – transpose
x – distance from the beginning of the seal
$\bar{(\cdot)}$ – averaged value

1 Introduction

Slotted seals are applied in steam turbines to minimize steam leakage in the regulating valve spindles. They are also applied in compressors and

combustion engines in piston cylinder assemblies. Such type of seal significantly influences the efficiency of many machines. The influence of the slot height on the efficiency of a piston engine was analyzed in [6]. Presented method enable the determination of the rate of incompressible liquid leakage through a slotted seal [2,8–12]. These methods are based on the Bernoulli equation with regard to experimentally obtained coefficients of of linear and local resistance. The results of the described methods have been presented for different geometries of the seal and pressure drop for both stationary and dynamic (rotating shaft) states. Paper [7] includes the analysis of gas flow in a short labyrinth seal based on experimental research using one dimensional theory. In the description of the mass flow, the authors of this paper, using one-dimensional theory, applied the gas flow model for a short pipe. Paper [1] includes the model allowing for the influence of tangential tensions in a two disc, one-sided seal geometry. The experimental research on the determination of coefficients of friction losses for short segments of one-sided seals have been presented in [14,16].

Equations for laminar and turbulent flows of compressible and incompressible liquids in slotted seals have been described in [15]. However, they provide mass flows far from those obtained in the experiments performed by the authors. In works related to slotted seals there is a deficit of methods providing satisfactory accuracy of calculations applicable in the flow of compressible liquids.

The thermodynamic parameters of gas flowing through any type of seal change along its length [3–5], which also includes the discussed slotted seal. Pressure, temperature, density and gas velocity are changed in the first place. This paper presents a model of gas flow in a slotted seal based on the friction coefficient obtained in the experimental research.

2 Calculation model

The flow of gas in a slotted seal is triggered by the pressure gradient. The mass flow of gas is reduced by the flow resistance generated by the tangential tensions between the gas and the seal walls [7,13,15]. The relation can be described with a set of equations in which, due to the gas flow, averaged values were applied referred to the conditions at the inlet and outlet of the seal

$$\begin{cases} \Delta pA = \tau OL \\ \tau = c_f \bar{\rho} \frac{\bar{u}^2}{2} \end{cases}, \tag{1}$$

where the average value of the gas density is determined by the formula $\bar{\rho} = \frac{p_1+p_2}{R(T_1+T_2)}$. Assuming that the gas flow in the seal segment is realized according to the irreversible adiabatic process we can write the relation between kinetic energy, static enthalpy, work of friction and heat of friction [13]

$$d\left(\frac{u^2}{2}\right) + dh + dL_f - dq_f = 0 \,, \tag{2}$$

where $dL_f = \frac{c_{f,i}u_i^2}{HS}dx$, $dq_f = dT_f c_p$, $dL_f = dq_f$, and the subscript i denotes value for the ith element.

Considering Eqs. (1) and (2) for the flowing gas in ith portion of the length of $x_{i+1} - x_i$ (Fig. 1.) we can determine the increase in gas temperature by $\Delta T_{f,i}$ resulting from the friction heat generated by dissipation of kinetic energy

$$\Delta T_{f,i} = c_{f,i}\frac{u_i^2}{c_p}\frac{x_{i+1} - x_i}{HS}. \tag{3}$$

This heat leads to an increase in the temperature and a reduction of the gas density that directly influences the velocity and flow resistance. Under measurement conditions, it is difficult to exclude or estimate the flow of heat between the seal in the walls and the decompressing gas. Without a doubt it has an effect on the final temperature of gas. The said heat flow together with the kinetic energy dissipated into friction heat influence the drop of the gas pressure Δp in the segment of the seal. The model presented in the paper is based on the assumption of constant total enthalpy. In the model, a local friction coefficient was taken into account according to the Blasius equation for a turbulent gas flow over flat surface [16]

$$c_{f,i} = \frac{0.0592}{\mathrm{Re}_{x,i}^{0.2}} \,, \tag{4}$$

where $\mathrm{Re}_{x,i} = \frac{u_i x}{\nu_i}$ – local Reynolds number.

The seal of diameter D, length L and height of slot HS is divided in to n numbers of elements. We know the initial and final parameters of the medium: p_1, T_1, p_{n+1}. In the initial phase of the calculations the final temperature is assumed as $T_{n+1} = T_{2s}$, which results from the isentropic transformation and a linear temperature drop. The distribution of gas temperature in the iterative process is corrected by the increment of temperature (3) resulting from the friction work (2).

The flowing gas is decompressed and its temperature varies longitudinally. In the model, the following has been assumed:

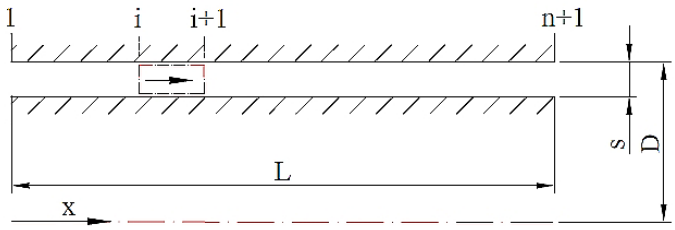

Figure 1: Geometry of the slotted seal.

- linear distribution of pressure,
- flow of gas with constant total enthalpy,
- mass flow of gas is limited by friction as per Eq. (4).

The presented model is applied in calculations of subsonic velocities of gas.

In the model, the continuity equation for the ith and $i+1$ cross-sections was taken into account

$$\dot{m}_i = A\rho_i u_i \ , \tag{5}$$

$$\dot{m}_{i+1} = A\rho_{i+1} u_{i+1} \ , \tag{6}$$

as well as the equation of state

$$\frac{p_i}{\rho_i} = RT_i \ , \tag{7}$$

$$\frac{p_{i+1}}{\rho_{i+1}} = RT_{i+1} \ , \tag{8}$$

and condition of conservation of mass flow between the calculation nodes:

$$\dot{m}_i = \dot{m}_{i+1} \ . \tag{9}$$

The equation of total enthalpy for the calculation cell between the ith and $i+1$ cross-sections has been written as follows:

$$\begin{aligned} T_i c_p + \frac{u_i^2}{2} &= T_{i+1} c_p + \Delta T_{i+1} c_p + \frac{u_{i+1}^2}{2} = \\ &= T_{i+1} c_p + \frac{u_{i+1}^2}{2}\left(1 + c_{f,i}\frac{x_{i+1} - x_i}{HS}\right) \ . \end{aligned} \tag{10}$$

In the main model described by Eq. (10) the flow resistance triggered by the friction was taken into account causing dissipation of kinetic energy

into heat dq_f (2).

Equations (5)–(10) written for $n+1$ cross-sections have an unknown mass flow, velocity in each cross-section and density as well as temperature in cross sections 2 to n. The mass flow resulting from Eqs. (5)–(10) can be written as

$$\dot{m}_i = \left[\frac{2A^2 c_p p_i^2 p_{i+1}^2 \left(T_i - T_{i+1}\right)}{R^2 \left[\left(1 + c_{f,i} \frac{x_{i+1} - x_i}{HS}\right) p_i^2 T_{i+1}^2 - p_{i+1}^2 T_i^2 \right]} \right]^{0.5} . \tag{11}$$

Assuming the constants

$$C_1 = 2A^2 c_p p_i^2 p_{i+1}^2 , \tag{12}$$

$$C_2 = R^2 \left(1 + c_{f,i} \frac{x_{i+1} - x_i}{HS}\right) p_i^2 , \tag{13}$$

$$C_3 = R^2 p_{i+1}^2 , \tag{14}$$

Eq. (11) takes the form

$$\dot{m}_i = \left[\frac{C_1 \left(T_i - T_{i+1}\right)}{C_2 T_{i+1}^2 - C_3 T_i^2} \right]^{0.5} . \tag{15}$$

Complete differential of the function of mass flow describes the change of the mass flow of gas flowing through the ith element depending on the temperature change at the beginning and end of a given element. The change was determined in the following way:

$$d\dot{m}_i = \frac{\partial \dot{m}_i}{\partial T_i} dT_i + \frac{\partial \dot{m}_i}{\partial T_{i+1}} dT_{i+1} . \tag{16}$$

The above equation transformed to finite increments can be written as follows:

$$\Delta \dot{m}_i = \frac{\partial \dot{m}_i}{\partial T_i} \Delta T_i + \frac{\partial \dot{m}_i}{\partial T_{i+1}} \Delta T_{i+1} , \tag{17}$$

adopting notation (15) of the mass flow equation, the partial derivatives in equation (17) have the following form:

$$\frac{\partial \dot{m}_i}{\partial T_i} = 0.5 \left[\frac{C_1 \left(T_i - T_{i+1}\right)}{C_2 T_{i+1}^2 - C_3 T_i^2} \right]^{-0.5} \times \frac{C_1 C_2 T_{i+1}^2 + C_1 C_3 \left(T_i^2 - 2 T_i T_{i+1}\right)}{\left(C_2 T_{i+1}^2 - C_3 T_i^2\right)^2} , \tag{18}$$

$$\frac{\partial \dot{m}_i}{\partial T_{i+1}} = 0.5 \left[\frac{C_1 (T_i - T_{i+1})}{C_2 T_{i+1}^2 - C_3 T_i^2} \right]^{-0.5} \times \frac{C_1 C_2 (T_{i+1}^2 - 2 T_i T_{i+1}) + C_1 C_3 T_i^2}{\left(C_2 T_{i+1}^2 - C_3 T_i^2 \right)^2} . \tag{19}$$

The vector of finite increments of mass flows can be described with the expression

$$\Delta \dot{m}_i - \Delta \dot{m}_{i+1} = \frac{\partial \dot{m}_i}{\partial T_i} \Delta T_i + \left(\frac{\partial \dot{m}_i}{\partial T_{i+1}} - \frac{\partial \dot{m}_{i+1}}{\partial T_{i+1}} \right) \Delta T_{i+1} - \frac{\partial \dot{m}_{i+1}}{\partial T_{i+2}} \Delta T_{i+2} \tag{20}$$

for $i = 1, \ldots, n-1$.

The presented method enables a notation of a matrix equation

$$\mathbf{B} \Delta T = \Delta \dot{m} . \tag{21}$$

Based on the right sides of the (n-1) set of Eqs. (17) matrix $\mathbf{B}$ was created

$$\mathbf{B} = \begin{bmatrix}
\left(\frac{\partial \dot{m}_1}{\partial T_2} - \frac{\partial \dot{m}_2}{\partial T_2} \right) & \frac{\partial \dot{m}_2}{\partial T_3} & 0 & \cdots & \cdots & \cdots & \cdots & 0 \\
\frac{\partial \dot{m}_2}{\partial T_2} & \left(\frac{\partial \dot{m}_2}{\partial T_3} - \frac{\partial \dot{m}_3}{\partial T_3} \right) & \frac{\partial \dot{m}_3}{\partial T_4} & 0 & \cdots & \cdots & \cdots & 0 \\
0 & \frac{\partial \dot{m}_3}{\partial T_3} & \left(\frac{\partial \dot{m}_3}{\partial T_4} - \frac{\partial \dot{m}_4}{\partial T_4} \right) & \frac{\partial \dot{m}_4}{\partial T_5} & 0 & \cdots & \cdots & 0 \\
\vdots & 0 & \ddots & \ddots & \ddots & 0 & \cdots & 0 \\
\vdots & \vdots & 0 & \ddots & \ddots & \ddots & 0 & 0 \\
\vdots & \vdots & \vdots & 0 & \ddots & \ddots & \ddots & 0 \\
0 & \vdots & \vdots & \vdots & 0 & \frac{\partial \dot{m}_{n-2}}{\partial T_{n-2}} & \left(\frac{\partial \dot{m}_{n-2}}{\partial T_{n-1}} - \frac{\partial \dot{m}_{n-1}}{\partial T_{n-1}} \right) & \frac{\partial \dot{m}_{n-2}}{\partial T_{n-1}} \\
0 & 0 & 0 & 0 & 0 & 0 & \frac{\partial \dot{m}_{n-1}}{\partial T_{n-1}} & \left(\frac{\partial \dot{m}_{n-1}}{\partial T_n} - \frac{\partial \dot{m}_n}{\partial T_n} \right)
\end{bmatrix} \tag{22}$$

and vector $\mathbf{\Delta T}$, whose elements are defined in the following manner

$$\Delta \mathbf{T} = \begin{bmatrix} \Delta T_1 & \Delta T_2 & \ldots & \Delta T_{n-1} \end{bmatrix}^T . \tag{23}$$

The vector of differences of the mass flows was obtained from Eq. (20) based on the assumed drop of pressure and calculated drop of temperature

$$\Delta \dot{\mathbf{m}} = \begin{bmatrix} \Delta \dot{m}_1 & \Delta \dot{m}_2 & \ldots & \Delta \dot{m}_{n-1} \end{bmatrix}^T , \tag{24}$$

where

$$\Delta \dot{m}_i = \dot{m}_i - \dot{m}_{i+1} = \left[\frac{C_1 (T_i - T_{i+1})}{C_2 T_{i+1}^2 - C_3 T_i^2} \right]^{0.5} - \left[\frac{C_1 (T_{i+1} - T_{i+2})}{C_2 T_{i+2}^2 - C_3 T_{i+1}^2} \right]^{0.5} \tag{25}$$

for $i = 1, \ldots, n-1$. The superscript T denotes transpose of the vector.

By multiplying Eq. (21) by the matrix inversed to matrix $\mathbf{B}$ we obtain an unknown vector of temperature changes $\Delta\mathbf{T}$. The initially assumed linear gas temperature distribution is corrected iteratively by vector $\Delta\mathbf{T}$. This gives the correction of vector $\Delta\dot{\mathbf{m}}$. This is a quickly convergent process aiming at preservation of the continuity of flow, hence obtaining very small components of the vector of mass flow differences $\Delta\dot{\mathbf{m}} \to 0$.

The end of the iterative calculations occurs when the maximum value of the component of the vector of mass flow differences, referred to the average value of the mass flow, obtained for $n+1$ cross-sections in a given iteration is smaller or equal to the assumed calculation accuracy $\delta = 10^{-5}$:

$$\frac{|\Delta\dot{\mathbf{m}}_{\max,it}|}{\bar{\dot{m}}_{it}} \leq \delta \ . \tag{26}$$

The first part of the iterative calculations was preformed for a linear distribution of gas temperature. This distribution continues from the initial temperature obtained from the measurement through the final temperature resulting from the isentropic transformation.

In the next phase of calculations, based on the obtained vectors $\mathbf{u}$, $\boldsymbol{\rho}$, $\mathbf{T}$, temperature vector $\mathbf{T}$ is enlarged by the temperature increment vector resulting from friction $\Delta\mathrm{T}_f$ as per Eq. (3)

$$\mathbf{T} = \mathbf{T} + \Delta\mathbf{T}_f \ . \tag{27}$$

Taking into account Eq. (27) results in a change of the gas temperature distribution in the cross-sections from 2 to $n+1$. Then, based on the initial temperature T_1 and corrected final temperature T_{n+1} the iterative model aims at such a temperature distribution that will ensure a continuity of flow with condition (26). The source code of the presented calculation algorithm has been written in Fortran.

3 Comparison of experimental data with the model calculation results

The experimental research was performed on a test stand described in [3]. The tests were preformed for the seal of diameter $D = 0.15$ m, length $L = 0.2$ m and slot height $HS = 0.002$ m (Fig. 1). The data obtained in the experiment have been included in Tab. 1.

Table 1: Gas thermodynamic parameters and mass flows obtained in the experimental research and in the model.

No.	p_1 [Pa]	T_1 [K]	p_1/p_2 [–]	$\dot{m}_e$[kg/s]	$\dot{m}_m$[kg/s]
1	148122	295.9	1.54	0.2554	0.1820
2	144556	295.7	1.50	0.2458	0.1676
3	139989	295.4	1.45	0.2329	0.1478
4	135842	295.2	1.40	0.2203	0.1246
5	131625	294.8	1.35	0.2073	0.0948
6	127835	294.5	1.30	0.1931	0.0466
7	123969	294.2	1.25	0.1790	–
8	119905	293.7	1.20	0.1599	–
9	115823	293.3	1.15	0.1395	–

Including the friction in the model using the Blasius Eq. (4) results in an elevated friction-based flow resistance. As an effect, a much smaller gas mass flow was obtained in the model compared to the experiment (Tab. 2, Fig. 2).

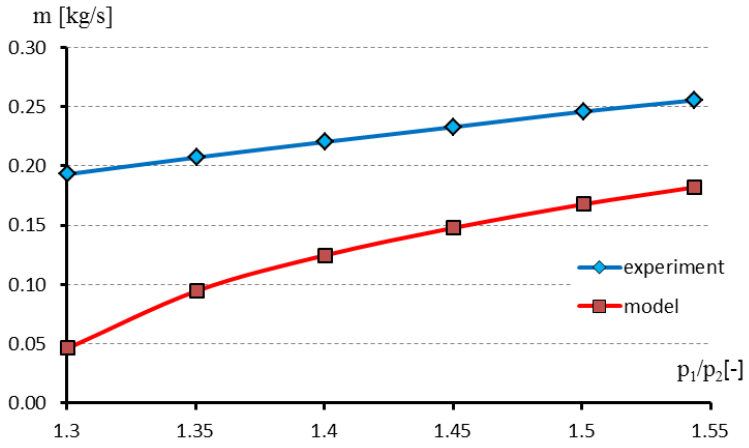

Figure 2: The mass flow obtained in the experiment and in the model including friction as in Eq. (4).

Besides, the application of Eq. (4) results in a situation when the range of applicability of the model is limited by small ratios of pressure $p_1/p_2 \geq 1.3$. This limitation results from conditions $T_i - T_{i+1} > 0$ in Eq. (11). In

order for the model to work properly, the temperature of gas flowing in the seal must be decreasing. Hence, the gas temperature drop following the decompression must be greater than the temperature increment caused by friction $\Delta T_{f,i}$.

The lines representing the values of local friction coefficients $c_{f,i}$ for different pressure ratios are similar to parallel (Fig. 3). We may, thus apply, in Eq. (4), a constant correction parameter on the entire length of the seal causing a reduction of the friction effect.

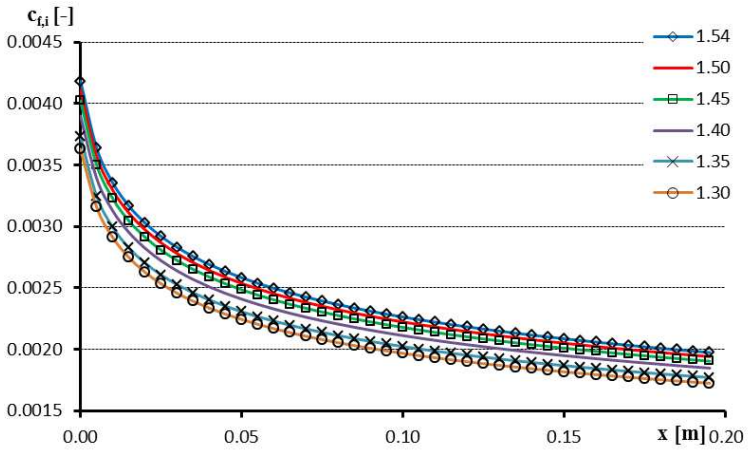

Figure 3: Local values of the friction coefficient on the seal length for the analyzed pressure drops p_1/p_2.

Based on the experimental data, the equation was corrected by friction coefficient (4) adding parameter C_e in the numerator of equation

$$c_{f,i} = \frac{0.0592 + C_e}{\mathrm{Re}_{x,i}^{0.2}} \,. \tag{28}$$

Parameter C_e was determined numerically so that the mass flow obtained from the model was equal to the value obtained in the experiment. The variability of C_e (Tab. 2.) as a function of pressure ratio has been shown in Fig. 4. The correction parameter of the local friction coefficient (28) was approximated by quadratic function

$$C_e = -0.0186 \left(\frac{p_1}{p_2}\right)^2 + 0.084 \left(\frac{p_1}{p_2}\right) - 0.105 \,. \tag{29}$$

Table 2: Values of the parameter correcting friction coefficient $c_{f,i}$ in Eq. (28) for condition $\dot{m}_{\mathrm{m}} = \dot{m}_{\mathrm{e}}$.

No.	p_1/p_2 [–]	C_e [–]
1	1.54	-1.97E-02
2	1.50	-2.07E-02
3	1.45	-2.19E-02
4	1.40	-2.34E-02
5	1.35	-2.54E-02
6	1.30	-2.68E-02
7	1.25	-2.95E-02
8	1.20	-3.09E-02
9	1.15	-3.24E-02

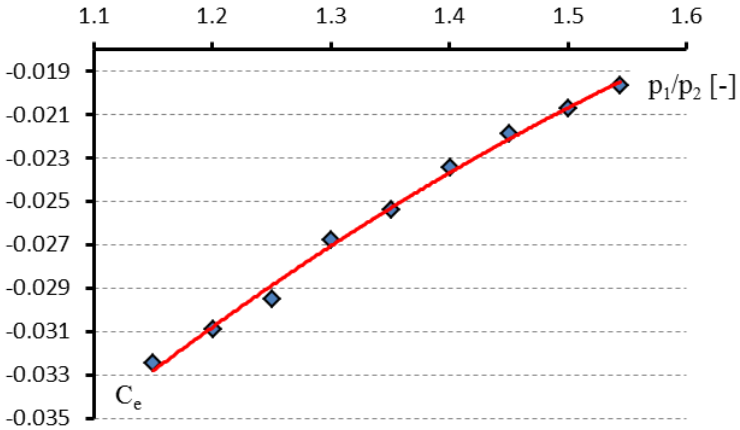

Figure 4: Parameter C_e correcting the local friction coefficient (28) as a function of pressure ratio p_1/p_2.

For selected pressure ratios p_1/p_2 in Fig. 5 a change in the gas velocity was presented as a function of length of the seal obtained from the calculation model. For the greatest pressure ratio p_1/p_2 equal to 1.54 the gas velocity clearly increases (Fig. 6.). High gas velocities in the seal may significantly intensify the heat transfer between the gas and the seal on the walls. For lower pressure ratios, the velocity increase follows the linear trend.

The change in the initial temperature of gas is a consequence of the experimental data. For parameter p_1/p_2 1.54 we can see the greatest drop of

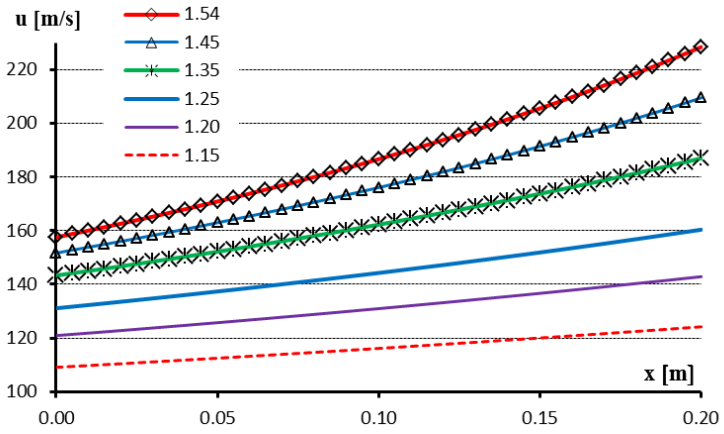

Figure 5: Distribution of the gas velocity on the length of the seal x for selected pressure ratios p_1/p_2.

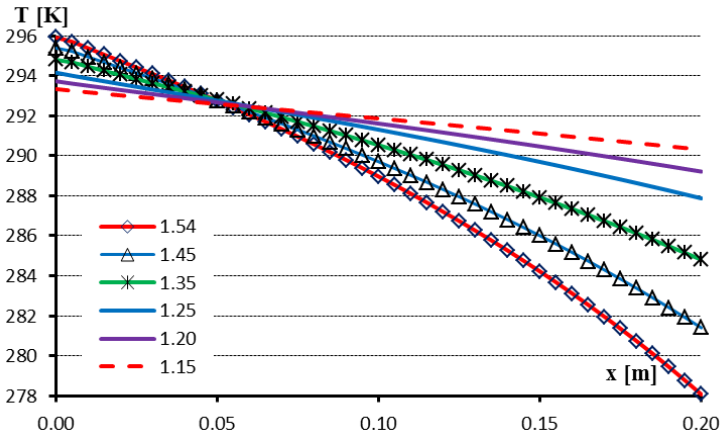

Figure 6: The change in the gas temperature on the length of the seal allowing for the friction heat according to Eqs. (10) and (28).

temperature resulting from the gas decompression. The lower the pressure ratio the lower is the drop of gas temperature (Fig. 6).

4 Conclusions

The presented calculation model based on the local friction coefficient, $c_{f,i}$, determined by the Blasius equation, gives the mass flow values that are much underestimated compared to the experimental data (Fig. 2). The introduction of the correction parameter, C_e, being a function of the pressure ratio in friction coefficient, $c_{f,i}$, enables obtaining of a accurate values of the mass flow through the model. The upper range of the pressure ratio, p_1/p_2, was limited by the measurement capability of the test facility. The proposed model allows for consideration of the kinetic energy dissipation in the form of heat, which allows the inclusion of the gas temperature increment. The model allows determining of the distributions of temperature, velocity and other gas thermodynamic parameters with a high level of accuracy. For significant differences of the seal wall and gas temperatures as well as high gas velocities, the heat transfer from the walls to the gas may significantly influence the leakage rate of the working medium in the slotted seal.

Acknowledgement This work was carried out in the framework of the research project NN513 324 740, which was financed by NCN.

Received 16 December 2015

References

[1] Childs D.W., J. K. Scharrer: *An iwatsubo-based solution for labyrinth seals: comparison to experimental results*. J. Eng. Gas Turb. Power **108**(1986), 2, 325–331.

[2] Grokhovskii D.V.: *Rational construction on slotted seals for feed pumps*. Chem. Petroleum Eng. **30**(1994), 9–10.

[3] Joachimiak D.: *The labyrinth seals research with extraction*. PhD thesis, Poznan University of Technology, Poznan 2013 (in Polish).

[4] Joachimiak D., Krzyślak P.: *Comparison of the calculation methods labyrinth seals and determination flow factor on the basis of experimental data, Machinery and equipment power*. In: Proc. 3rd Technical and Scientific Conference (S. Łopata, Ed.), Cracow 2013, 105-114, (in Polish).

[5] Joachimiak D., Krzyślak P.: *Comparison of results of experimental research with numerical calculations of a model one-sided seal*. Arch. Thermodyn. **36**(2015), 2, 61–74.

[6] Larjola J., Honkatukia J., Sallinen P., Backman J.: *Fluid dynamic modeling of a free piston engine with labyrinth seals*. Int. J. Therm. Sci. **19**(2010), 2, 141–147.

[7] Lin Z., Wang X., Yuan X., Shibukawa N., Noguchi T.: *Investigation and improvement of the staggered labyrinth seal*. Chin. J. Mech. Eng., **28**(2015), 2, 402–408.

[8] Mel'nik V.A.: *Computed universal dependence for determining leakage of media through groove seals*. Chem. Petroleum Eng. **48**(2013), 11–12.

[9] Mel'nik V.A.: *Simplified method of calculating the operating characteristics of a face seal*. Chem. Petroleum Eng. **39**(2003), 9–10.

[10] Mel'nik V.A.: *Calculating leaks in rotor-machine radial slot seals. Part 1. Method based on calculated and empirical local pressure loss coefficients*. Chem. Petroleum Eng. **45**(2009), 9–10.

[11] Mel'nik V.A.: *Calculating leaks in rotor-machine radial slot seals. Part 2. A method for integral slot flow rate constants*. Chem. Petroleum Eng. **45**(2009), 11–12.

[12] Mel'nik V.A.: *Calculating leaks in rotary machine radial slot seals. Part 3. Method for calculating leaks taking account of the inlet section*. Chem. Petroleum Eng. **46**(2010), 3–4.

[13] Prosnak W.J.: *Fluid Mechanics*. PWN, Warsaw 1971 (in Polish).

[14] Thiekle G., Stetter H.: *Identification of friction factors for modeling the exciting forces caused by flow in labyrinth seals*. Rotordynamics '92 (J. Michael, Ed.), Springer-Verlag, London 1992.

[15] Trütnovsky K.: *Berührungsfreie Dichtungen, Grundlagen und Anwendungen der Strömung durch Spalte und Labyrinthe*. VDI-Verlag bh Düsseldorf, Verlag des Vereins Deutscher Ingenieure 1964.

[16] Wiśniewski S., Wiśniewski T.S.: *Heat Transfer*. WNT, Warsaw 2012 (in Polish).

[17] Yamada Y.: *On the pressure loss of flow between rotaring co-axial cylinders with rectangular grooves*. Bull. JSME **5**(1962), 20, 642–651.

archives
of thermodynamics
Vol. **37**(2016), No. 3, 109–138
DOI: 10.1515/aoter-2016-0023

Validation of the generalized model of two-phase thermosyphon loop based on experimental measurements of volumetric flow rate

HENRYK BIELIŃSKI *

Institute of Fluid Flow Machinery, Polish Academy of Sciences, Fiszera 14, 80-231 Gdańsk, Poland

Abstract The current paper presents the experimental validation of the generalized model of the two-phase thermosyphon loop. The generalized model is based on mass, momentum, and energy balances in the evaporators, rising tube, condensers and the falling tube. The theoretical analysis and the experimental data have been obtained for a new designed variant. The variant refers to a thermosyphon loop with both minichannels and conventional tubes. The thermosyphon loop consists of an evaporator on the lower vertical section and a condenser on the upper vertical section. The one-dimensional homogeneous and separated two-phase flow models were used in calculations. The latest minichannel heat transfer correlations available in literature were applied. A numerical analysis of the volumetric flow rate in the steady-state has been done. The experiment was conducted on a specially designed test apparatus. Ultrapure water was used as a working fluid. The results show that the theoretical predictions are in good agreement with the measured volumetric flow rate at steady-state.

Keywords: Thermosyphon loop; Two-phase flow; Minichannels

Nomenclature

A	–	cross-section area of the channel, m^2
B	–	width, m
c_p	–	specific heat at constant prtessure, $J/Kg\,K$
D	–	internal diameter of the tube, m
$\dot{G}$	–	mass flux, kg/m^2s

*E-mail: hbiel@imp.gda.pl

g – acceleration, m/s^2
H – height, m
h – heat transfer coefficient, W/(m^{2}K)
L – total length of the closed loop, m
L_H – length of heated section, m
L_C – length of cooled section, m
$\dot{m}$ – mass flow rate, kg/s, $\dot{m} = \dot{V}\rho$
p – pressure, Pa
$\dot{Q}$ – heat flow rate, W
$\dot{q}$ – heat flux, W/(m^2)
s – axial coordinate around the loop, m
U – wetted perimeter, m
$\dot{V}$ – volumetric flow rate, m^3/s
x – quality of vapour

Greek symbols

α – void fraction, –
β – volumetric coefficient of thermal expansions, 1/K
ε – see Eq. (3)
ρ – mass density, kg/m^3
τ_w – wall shear stress, N/m^2
λ – thermal conductivity, W/mK

Subscripts and superscripts

C – cooler
H – heater
i, j, k, n – indices
L – liquid
V – vapour
$1P, 2P$ – single-, two-phase
$L0$ – liquid phase only
Fr – friction
LOC – local
ss – steady-state
TOT – total
0 – reference of steady state

Other symbols

$< \cdot >$ – per unit of time

1 Introduction

Trend towards the miniaturization of electronic devices creates specific heat dissipation problems. The two-phase thermosyphon loop has been extensively investigated for its possible applications in the cooling systems of electronic devices by many researchers [1–5]. In fact, there is still a need

for further studies to understand the thermosyphon cooling process.

The main purpose of this study is to present the experimental validation of the generalized model of two-phase thermosyphon loop. The generalized model of the two-phase thermosyphon loop and its different variants were demonstrated in previous papers [2,6–12]. This paper presents the theoretical analysis and the experimental data obtained for a new designed variant particularly suited for computer cooling requirements. The variant refers to a thermosyphon loop with both minichannels and conventional tubes. The thermosyphon loop consists of an evaporator on the lower vertical section and a condenser on the upper vertical section. The presented variant configuration with the evaporator (single-conventional tube) and condenser (single-minichannel tube) has not previously been experimentally investigated by other researchers. A numerical prediction of the volumetric flow rates in the steady-state has been done by examining the presented variant. The experiment was conducted on a specially designed test apparatus. Ultrapure water was used as a working fluid.

The generalized model is based on conservation equations of mass, momentum, and energy balances in the evaporators, rising tube, condensers and the falling tube. The one-dimensional homogeneous and separated two-phase flow models were used in calculations. The one-dimensional model was analyzed because the ratio of the channel loop diameter to the length of the channel was negligibly small. The results of these models were compared in terms of the volumetric flow rate. The generalized model can predict the thermosyphon loop system characteristics such as volumetric and mass flow rate, mass flux, heat transfer coefficient in flow boiling and condensation in minichannels and conventional tubes, local and friction resistance for a single- and two-phase flow in thermosyphon loop, geometrical parameters of the loop, thermal parameters of the heaters and coolers, stability of the onset of a global fluid motion in thermosyphon loop. One of the most important parameters used to describe the flow behavior and thermal performance of a natural circulation inside the thermosyphon loop is the volumetric and mass flow rate. The mass flow rate depends on properties of working fluid.

Many simulation studies have been undertaken to investigate the heat transfer behavior and two-phase fluid flow in the thermosyphon loop. Because of a lack of understanding about the dynamic nature of the flow and heat transfer in a thermosyphon, there is an increasing demand for validation experiments. Lamaison *et al.* [13] presented and validated a novel

dynamic simulation tool for predicting the behavior of a two-phase mini-thermosyphon with microchannels. Both the mini-thermosyphon and simulation tool was successfully applied for the retrofitting of a commercial server by cooling its two CPU processors. The study shows that a 30% increase in the riser diameter led to 60% increase in the mass flow rate depending on the heat flux. The multi-microchannel evaporator model was presented. The predicted mass flow rates demonstrate the gravity dominant regime (GDR) at low heat flux and the friction dominant regime (FDR) at high heat flux. Comparisons with the experimental values of mass flow rate are planned. Archana *et al.* [14] investigated the flow initiation transient and steady-state flow in the natural circulation loop. Their results were also validated by experiments. Authors suggested that the oscillations in the mass flow rate are caused by the friction force and buoyancy force. A steady state is reached when the buoyancy force is balanced by the frictional force. The mass flow rate increases with the increase in the power. They reported a very high amplitude oscillation at low power start-up. This peak of amplitude confirmed the existence of type I instability in the first unstable zone in the two-phase region. Lemos *et al.* [15] studied the correlation between two-phase flow pattern and thermal behavior of a natural circulation loop. Authors reported the results of flow rate measurements. The flow rate oscillations were identified. The oscillations exceeded a certain value (plateau) by running the experiment. The visualization of two-phase natural circulation flow was made using the high-speed camera. Vijayan *et al.* [16] studied experimentally and theoretically the effect of loop diameter on the steady-state and stability behavior of single-phase and two-phase natural circulation loops. Garrity *et al.* [17] investigated instability phenomena in a two-phase thermosyphon loop consisting of a microchannel evaporator and a condenser. The comparison between the experimental and simulation results obtained for the mass flow rate was reasonable. Franco *et al.* [18] designed an experimental test rig. They analyzed the thermodynamic behavior of a working fluid in closed loop two-phase thermosyphon. Results showed that the mass flow rate increases with growing input power ranging approximately from 0 to 1.7 kW. Higher instabilities were observed at higher heat loads. Authors presented a comprehensive review summarizing the results from many experimental studies for a small dimension two-phase closed-loop thermosyphon [19]. Khodabandeh [3,4] carried out extensive investigations on a rectangular thermosyphon loop with minichannels heated from below and cooled above with isobutane as a working fluid. The ex-

perimental results show that the heat transfer coefficient increases with increasing heat flux. Chen *et al.* [20] studied rectangular thermosyphon loops with horizontal heat transfer sections. This investigation was focused on determining the optimum configuration of the loop based on both the convection heat transfer coefficient and friction factor. Dobson *et al.* [21,22] simulated and experimentally verified the heat transfer and fluid flow in a rectangular thermosyphon loop with conventional channels and suggested that the proposed concepts for cooling can be used in the cooling system of the reactor cavity. Agostini *et al.* [1,23] proposed a solution of two-phase thermosyphon loop for the cooling of power electronics semiconductor modules. Their study shows potential use of the two-phase flow in the domain of electronic cooling and high-efficiency heat transfer from a source to a final cooling media. Cieśliński and Fiuk [24] studied experimentally the two-phase thermosyphon loop with horizontal evaporator and horizontal condenser using water, methanol and refrigerant R-141b as working fluids. Cieśliński [25] measured also the effect of concentration of the water-based Al_2O_3-nanofluid on thermal performance of the two-phase thermosyphon heat exchanger.

A natural circulation occurs in the thermosyphon loop. During the natural convection the heat is transported in the thermosyphon loop from a source to a sink. Fluid flow in a thermosyphon loop is created by the buoyancy force that evolves from the density gradients induced by temperature differences in the heating and cooling sections of the loop. An advanced two-phase thermosyphon loop consists of an evaporator, where the liquid boils; and a condenser, where the vapour condenses back to liquid; a riser and a downcomer connect these parts. Heat is transferred as the vaporization heat from the evaporator to the condenser. The thermosyphon is a passive heat transfer device, which makes use of gravity for returning the liquid to the evaporator. The thermosyphon loops are by far better solution than other cooling systems because they are pumpless. The closed loop thermosyphon is also known as a 'liquid fin' [26] (Fig. 1).

The single- and two-phase thermosyphon loops find many industrial applications [27,28], such as, for example: distillation process, steam generators, thermosyphon reboilers, chemical reactors, emergency cooling systems in nuclear reactor cores and reflux boiling systems in light water reactor cores, solar heating and cooling systems, geothermal energy generation and thermal diodes [6,7]. The thermal diode is a device, which allows the heat to be transferred in one direction, and blocks the heat flow in the opposite

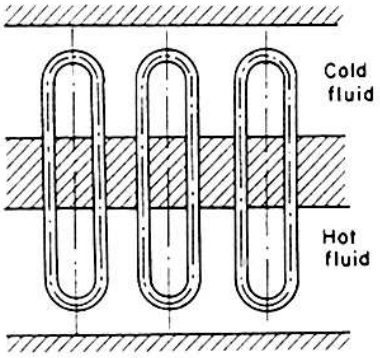

Figure 1: Schematic illustration of the liquid fin heated from below and cooled from above.

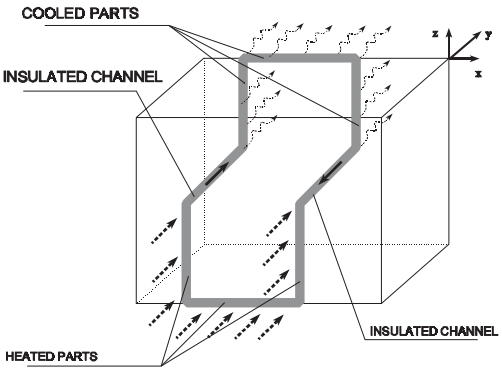

Figure 2: Schematic illustration of the thermal diode heated simultaneously from below and symmetrically from the sides.

direction (Fig. 2).

The thermosyphon effect is observed in loop heat pipe (LHP) if the evaporator is located below the condenser. A loop heat pipe is a completely passive heat transfer device, and consists of an evaporator, condenser, compensation chamber and some smooth transport lines for the vapour and liquid flows as shown in Fig. 3. The thermosyphon effect for cooling electronic devices can be applied in innovative miniature loop heat pipe (mLHP) with the evaporator located on the loop below the condenser.

The prototype of mLHP consists of a flat minievaporator and capillary pump. The porous wick material is placed inside capillary pump. The complete condensation of the medium takes place in a minicondenser. Both the mini-evaporator and mini-cooler are connected to the separate liquid and vapour channels. The high friction losses in mLHP can be reduced because the liquid/vapour phase flow in the separated channels and the porous wick is only present in minievaporator. The flat-shaped minievaporator is integrated with a capillary pump. The wicks generate the capillary pumping pressure, which is required to transport a working fluid along mLHP. The thermosyphon effect can also be applied in concept presented by Mikielewicz *et al.* [29] of micro-CHP-cogeneration where evaporator is located below condenser. The use of capillary forces for pumping of the working fluid in the Clausius–Rankine cycle is a new idea that allows the reduction or even the elimination of the pumping device in such cycles. It is also possible to exploit the gravity force to support the operation of a cir-

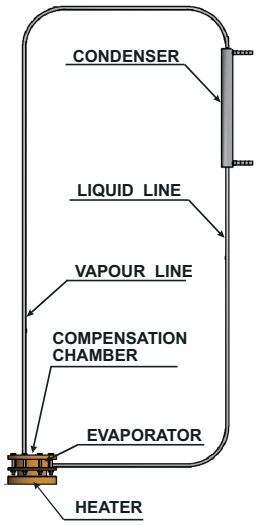

Figure 3: Idea scheme of miniature loop heat pipe (mLHP) with thermosyphon loop.

culation pump by placing the evaporator below the condenser and creating the thermosyphon loop.

In this study the presented variant of the rectangular thermosyphon loop with minichannels can be applied to describe the computer cooling system. The lower horizontal heater can be treated as a CPU processor located on the motherboard of personal computer and the lower vertical heater can simulate a chip located on vertical graphic card. The cooler must be placed above the heaters on the computer chassis. Heat exchangers are connected by minichannels filled with the liquid refrigerant.

2 Theoretical investigations

2.1 The generalized model of two-phase thermosyphon loop

A schematic diagram of the generalized model of two-phase thermosyphon loop is shown in Fig. 4. The thermosyphon loop is heated by three heaters in section: H1($s_0 \leq s \leq s_1$), H2($s_3 \leq s \leq s_4$), and H3($s_6 \leq s \leq s_7$) by a constant heat flux: $\dot{q}_{H_1}$, $\dot{q}_{H_2}$, $\dot{q}_{H_3}$, respectively and cooled from three coolers in section C1($s_8 \leq s \leq s_9$), C2($s_{11} \leq s \leq s_{12}$), and C3($s_{14} \leq s \leq s_{15}$) by a constant heat flux $\dot{q}_{C_1}$, $\dot{q}_{C_2}$, $\dot{q}_{C_3}$, respectively. The heated

and cooled regions of the thermosyphon loop are connected by perfectly insulated channels. The coordinate s along the loop and the characteristic geometrical points on the loop are marked with s_n, as shown in Fig. 4. The total length of the loop is denoted by L, the internal diameter of the channel of the individual region is denoted by D_k, the cross-sectional area of the individual channel is denoted by A_k and the wetted perimeter by U_k. Thermophysical properties of fluid: ρ – density, c_p – specific heat at constant pressure, λ – thermal conductivity.

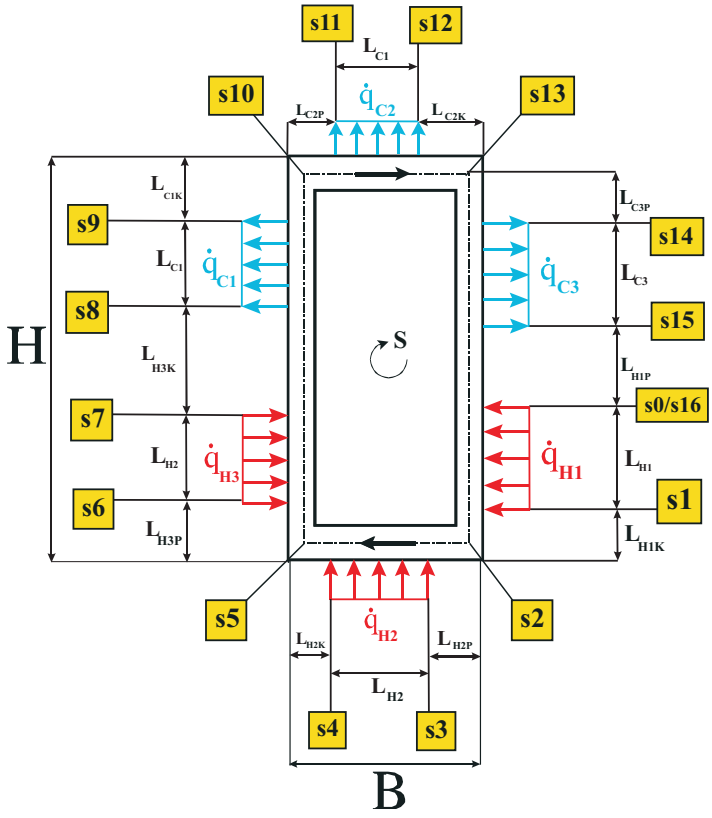

Figure 4: Schematic diagram of the generalized model of thermosyphon loop.

Using the generalized model it is possible to apply a different number of heaters and coolers. These heat exchangers can be placed at different locations on the loop. For example, the heat sources can be sitted at the bottom horizontal pipe or on the right/left vertical channels; similarly, the heat sinks can be chosen at the top horizontal pipe or on the right/left verti-

cal channels. It is shown that this generalized model can be used to describe any possible individual variants of thermosyphon loop including the earlier variants developed by the author [2, 8–12]. Fluid flow in a thermosyphon loop is created by the buoyancy force that evolves from the density gradients induced by temperature differences in the heating and cooling sections of the loop.

The following assumptions are made in this study:

1. Thermal equilibrium exists at any location of the loop.
2. Incompressibility, because the flow velocity in the natural circulation loop is relatively low compared with the acoustic speed of the fluid under current model conditions.
3. Viscous dissipation in the fluid is neglected in the energy equations.
4. $(D/L) \ll 1$; one-dimensional model is applied for the heat transfer and fluid flow in both single- and two-phase regions.
5. Fluid properties are constant, except density in the gravity term.
6. A linearly varying quality function $x(s)$ is assumed according to the study published in [27,30,31].
7. Single-phase fluid and two-phase mixture can be selected as the working fluid:
   (a) if the Boussinesq approximation is valid for a single-phase system, then density is assumed to vary as $\rho = \rho_0 [1 - \beta (T - T_0)]$ in the gravity term where $\beta = \frac{1}{v}\left(\frac{\partial v}{\partial T}\right)_p$, ($v$ – specific volume, '0' is the reference steady state),
   (b) two-phase friction factor multiplier R_{2P} is used to calculate the frictional pressure loss in heated, cooled and adiabatic two-phase sections in the two-phase system: $\Delta p_{2P,\,Fr} = R_{2P} \times \Delta p_{L0,\,Fr}$;
   (c) homogeneous or separated model of two-phase flow can be used to evaluate the friction pressure drop.
8. Two-phase mixture density ρ is given by the weighting of void fraction [17]

$$\rho = \begin{cases} \rho_L & \text{for liquid} \\ \rho_V & \text{for vapour} \end{cases} \qquad (1)$$

$$\rho = (1 - \alpha)\,\rho_L + \alpha \rho_V \;\; ; \qquad \text{for two-phase mixture}$$

9. Friction coefficient is constant in each region of the loop.
10. Changes of the potential energy in energy equation are neglected.
11. According to the model shown in Fig. 4 the incomplete evaporation and condensation of working fluid occurs in the heaters (H1), (H2), and (H3), and in the coolers (C1) and (C2), respectively. It was assumed that the working fluid is treated as the two-phase medium in the region ($s_0 \leq s \leq s_{15}$).
12. It was assumed that the sections $\langle s_1\,;\ s_3\rangle$, $\langle s_4\,;\ s_6\rangle$, $\langle s_7\,;\ s_8\rangle$, $\langle s_9\,;\ s_{11}\rangle$ and $\langle s_{12}\,;\ s_{14}\rangle$ are the adiabatic sections.

Due to the symmetry of the heating and cooling sections to the vertical axis, as shown in Fig. 4, the working fluid can flow incidentally in clockwise or counter clockwise direction. In case of the flow in clockwise direction two heaters (H2, H3) force the circulation of fluid around the loop and the third heater (H1) prevents the circulation. In case of the flow in counter-clockwise direction, two heaters (H2, H1) support the fluid circulation around the loop whereas the third one (H3) prevents the circulation. A good example for the technical solution responding to discussed cases can be the 'liquid fin' [26] or the 'thermal diode' [6,7].

2.2 The governing equations

Under the above assumptions, the single-dimensional, steady-state governing equations for natural circulation in two-phase thermosyphon loop can be written as follows [2,8–12]:

- conservation of mass:

$$\frac{\partial \rho}{\partial \tau} + \frac{\partial}{\partial s}(\rho w) = 0\,, \tag{2}$$

  where ρ – mass density, s – axial coordinate, τ – time, w – velocity;

- conservation of momentum:

$$\rho\left(\frac{\partial w}{\partial \tau} + w\frac{\partial w}{\partial s}\right) = -\frac{\partial p}{\partial s} + \varepsilon\rho\tilde{g} - \tau_w\frac{U}{A}\,, \tag{3}$$

  where $\varepsilon = 0$ for $\vec{e}\perp\vec{g}$, $\varepsilon = (+1)$ for $\vec{e}\uparrow \wedge\ \vec{g}\downarrow$, and $\varepsilon = (-1)$ for $\vec{e}\downarrow \wedge\ \vec{g}\downarrow$; $\tilde{g} = \vec{e}\cdot\vec{g} = g\,\cos(\vec{e},\vec{g})$; $|\vec{g}| = g$; $|\vec{e}| = 1$; $\vec{g}$ is an acceleration vector, $\vec{e}$ is a versor of the coordinate around the loop, $\uparrow$ – sense of a vector and τ_w – wall shear stress;

- conservation of energy:

$$\frac{\partial T}{\partial \tau} + w\frac{\partial T}{\partial s} = a\frac{\partial^2 T}{\partial s^2} + \left\{ \begin{array}{lll} 0 & \text{for} & \text{adiabatic section} \\ -\frac{q_C U}{c_p \rho A} & \text{for} & \text{cooled section} \\ +\frac{\dot{q}_H U}{c_p \rho A} & \text{for} & \text{heated section} \end{array} \right\} , \quad (4)$$

where $a = \frac{\lambda}{\rho c_p}$ – thermal diffusivity, c_p – specific heat at constant pressure, U is the wetted perimeter.

Fluid flow and heat transfer can be considered in a steady-state analysis

$$\frac{\partial}{\partial \tau} = 0 \, . \quad (5)$$

In order to eliminate the pressure gradient, the momentum term in Eq. (3) is integrated around the loop:

$$\oint \left(\frac{dp}{ds}\right) ds = 0 \ , \ \ p(0) = p(L) \, . \quad (6)$$

2.3 Case for validation of the generalized model of two-phase thermosyphon loop

The experimental measurements have been made for the case of the generalized model presented in Fig. 5. This two-phase thermosyphon loop consists of minichannels and conventional tubes. The thermosyphon loop is heated from the lower vertical section ($s_3 \leq s \leq s_4$) by a constant heat flux $\dot{q}_H$, and cooled in the upper vertical section ($s_7 \leq s \leq s_8$) by a constant heat flux, $\dot{q}_C$. The heated and cooled parts of the thermosyphon loop are connected by perfectly insulated channels.

As shown in Fig. 5 the space coordinate s circulates around the loop. The following parameters of the lop are known: the coordinates of the characteristic points s_i, the internal diameter D_j, the cross-section area A_j, the wetted perimeter U_j and the total length L. A linearly varying quality function $x(s)$ are assumed according to the study published in [27,30,31].

The sum of acceleration pressure drops is neglected, because of the acceleration of the evaporating liquid in the evaporator is balanced by the deacceleration of the condensing vapour in the condenser in the thermposyphon loop [31]. Thus, by integrating around the loop, the momentum equation in (3) can be reduced to the form

$$\oint_{LOOP} \left(\tau_w \frac{U}{A}\right) ds + \oint_{LOOP} (\varepsilon \rho \tilde{g}) ds = 0 \, . \quad (7)$$

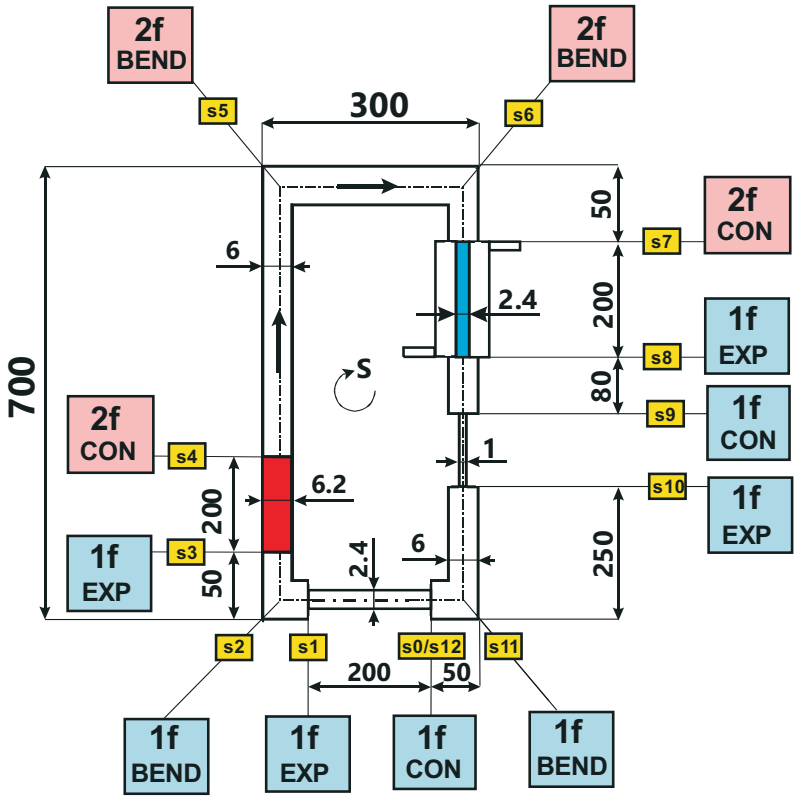

Figure 5: Theoretical model of the two-phase thermosyphon loop with minichannels and conventional tubes (BEND; EXP: sudden expansion; CON: sudden contraction.

2.4 Gravitational term in the momentum equation

The gravity term in the momentum Eq. (7) can be expressed as

$$\oint_{LOOP} (\varepsilon\,\rho\,\tilde{g})\;ds = g\;(\rho_V - \rho_L)\;\Big\{(s_4 - s_3)\;\bar{\alpha}_{\langle s_3;s_4\rangle} + \\ + \left[(s_5 - s_4) - (s_7 - s_6)\right]\;\bar{\alpha}_{\langle s_4;s_7\rangle} - (s_8 - s_7)\;\bar{\alpha}_{\langle s_7;s_8\rangle}\Big\}\;, \tag{8}$$

where

$$\bar{\alpha}_{\langle s_i;s_j\rangle} = \frac{1}{(s_j - s_i)} \int_{s_i}^{s_j} \alpha_{\langle s_i;s_j\rangle}\,(s)\;ds\,. \tag{9}$$

2.5 Frictional term in the momentum equation

In the thermosyphon loop during the fluid circulation, the following pressure losses $\Delta p_{TOT,\,Fr}$ can be recognized: the pressure loss for overcoming the friction resistance in the pipes Δp_{Fr} and the pressure losses for overcoming the local resistance Δp_{LOC} (bend, sudden expansion, sudden contraction).

$$\Delta p_{TOT,\,Fr} = \Delta p_{Fr} + \Delta p_{LOC}\,. \tag{10}$$

Two phase local pressure drop is calculated with

$$\Delta p_{2P,\,LOC} = \Psi^{2P}_{L0,\,LOC} \times \Delta p_{L0,\,LOC}\,, \tag{11}$$

where $\Psi^{2P}_{L0,\,LOC}$ is a two-phase local loss multiplier and $\Delta p_{L0,\,LOC}$ is a local pressure loss when all the mixture is liquid.

The frictional component of the pressure gradient in two-phase regions was calculated using the two-phase separated model. Due to friction of fluid, the pressure gradient in two-phase regions can be written as follows [10,21]:

$$\left(\frac{-dp}{ds}\right)_{2P,\,Fr} = R_{2P}\left(\frac{-dp}{ds}\right)_{L0,\,Fr} \tag{12}$$

where R_{2P} is the local two-phase friction factor, $\left(\frac{dp}{ds}\right)_{L0,\,Fr}$ is only the liquid frictional pressure gradient calculated for the liquid total volumetric flow rate. After integrating the friction term around the loop, we obtain

$$\begin{aligned}
&\oint \left(\frac{dp}{ds}\right)_{Fr,2P} ds = \\
&= \left\{ \left(\frac{dp}{ds}\right)^{\langle s_3;s_4\rangle}_{L0,\,Fr} (s_4 - s_3)\,\bar{R}_{\langle s_3;s_4\rangle} + \left(\frac{dp}{ds}\right)^{\langle s_4;s_7\rangle}_{L0,\,Fr} (s_7 - s_4)\,\bar{R}_{\langle s_4;s_7\rangle} + \right. \\
&+ \left(\frac{dp}{ds}\right)^{\langle s_7;s_8\rangle}_{L0,\,Fr} (s_8 - s_7)\,\bar{R}_{\langle s_7;s_8\rangle} + \left(\frac{dp}{ds}\right)^{\langle s_0;s_1\rangle}_{L0,\,Fr} (s_1 - s_0) + \\
&+ \left(\frac{dp}{ds}\right)^{\langle s_8;s_9\rangle}_{L0,\,Fr} [(s_9 - s_8) + (s_{12} - s_{10}) + (s_3 - s_1)] + \\
&\left. + \left(\frac{dp}{ds}\right)^{\langle s_9;s_{10}\rangle}_{L0,\,Fr} (s_{10} - s_9) \right\}\,,
\end{aligned} \tag{13}$$

where

$$\bar{R}_{\langle s_i;s_j\rangle} = \frac{1}{(s_j - s_i)} \int_{s_i}^{s_j} R\,(s)\; ds\,. \tag{14}$$

Substituting Eqs.(8) and (13) and the sum of local resistance into the momentum Eq. (7) gives

$$\left\{\left(\frac{dp}{ds}\right)_{L0,\,Fr}^{\langle s_3;s_4\rangle}(s_4-s_3)\,\bar{R}_{\langle s_3;s_4\rangle}+\left(\frac{dp}{ds}\right)_{L0,\,Fr}^{\langle s_4;s_7\rangle}(s_7-s_4)\,\bar{R}_{\langle s_4;s_7\rangle}+\right.$$
$$+\left(\frac{dp}{ds}\right)_{L0,\,Fr}^{\langle s_7;s_8\rangle}(s_8-s_7)\,\bar{R}_{\langle s_7;s_8\rangle}+\left(\frac{dp}{ds}\right)_{L0,\,Fr}^{\langle s_0;s_1\rangle}(s_1-s_0)+$$
$$+\left(\frac{dp}{ds}\right)_{L0,\,Fr}^{\langle s_8;s_9\rangle}[(s_9-s_8)+(s_{12}-s_{10})+(s_3-s_1)]+$$
$$\left.+\left(\frac{dp}{ds}\right)_{L0,\,Fr}^{\langle s_9;s_{10}\rangle}(s_{10}-s_9)\right\}+\sum_{i=1}^{12}\Delta p_{LOC_i}+g\,(\rho_V-\rho_L)\left\{(s_4-s_3)\,\bar{\alpha}_{\langle s_3;s_4\rangle}+\right.$$
$$\left.+\left[(s_5-s_4)-(s_7-s_6)\right]\,\bar{\alpha}_{\langle s_4;s_7\rangle}-(s_8-s_7)\,\bar{\alpha}_{\langle s_7;s_8\rangle}\right\}=0\,. \tag{15}$$

In the case of minichannels, it is necessary to use new correlations for void fraction and the local two-phase friction coefficient in the two-phase region. The following correlations have been used to calculate the two-phase flow in the thermosyphon loop with minichannel:

- the El-Hajal *et al.* [33] correlation for void fraction,
- the Tran *et al.* [34] correlation for the friction pressure drop of two-phase flow for $\langle s_7; s_8\rangle$ the diabatic section and minichannels.

The following correlations have been used to calculate the two-phase flow in the thermosyphon loop with conventional tubes:

- the standard Zuber-Findlay [35] drift flux model of two-phase flow for void fraction,
- the Müller-Steinhagen and Heck [36] correlation for the friction pressure drop in two-phase flow for $\langle s_3; s_4\rangle$ the diabatic region and conventional tube, and for $\langle s_4; s_7\rangle$ the adiabatic region and conventional tube.

The following correlations have been used to calculate the local resistance of two-phase flow in the thermosyphon loop:

Table 1: Correlations for the void fraction and the friction pressure drop of two-phase flow in minichannel.

Researcher	Correlations for minichannel
El-Hajal *et al.* [33]	$\alpha_{HAJAL} = \frac{\alpha_{HOM} - \alpha_{STEINER}}{\ln\left(\frac{\alpha_{HOM}}{\alpha_{STEINER}}\right)}$; $\alpha_{HOM} = \frac{1}{1+\frac{1-x}{x}\left(\frac{\rho_V}{\rho_L}\right)}$; $\alpha_{STEINER} = \left(\frac{x}{\rho_V}\right) \times$ $\times \left\{[1+0.12\,(1-x)] \times \left[\frac{x}{\rho_V} + \frac{1-x}{\rho_L}\right] + \frac{1.18\,(1-x)[g\sigma(\rho_L-\rho_V)]^{0.25}}{G(\rho_L)^{0.5}}\right\}^{(-1)}$; (16)
Tran *et al.* [34]	$\left(\frac{dp}{dl}\right)^{TRAN}_{2P,\,Fr} = R^{TRAN}_{L0,\,2P} \times \left(\frac{dp}{dz}\right)_{Fr,\,L0}$; $R^{TRAN}_{2P,\,L0} = 1 + \left(4.3\,Y^2 - 1\right) \times \left[N_{CONF}\,(x)^{0.875}\,(1-x)^{0.875} + (x)^{1.75}\right]$; (17) $N_{CONF} = \frac{\left[\frac{\sigma}{g(\rho_L-\rho_V)}\right]^{0.5}}{D}$; $Y = \sqrt{\left(\frac{dp}{dz}\right)_{V0} \Big/ \left(\frac{dp}{dz}\right)_{L0}}$;

Table 2: Correlations for the void fraction and the friction pressure drop of two-phase flow in conventional tubes.

Researcher	Correlations for conventional tube
Zuber-Findlay [35]	$\bar{\alpha}_{2P} = \frac{1}{\left\{C_0\left[1+\left(\frac{1-x}{x}\right)\left(\frac{\rho_V}{\rho_L}\right)\right]+\frac{\rho_V}{G\,x}\,V_{vj}\right\}}$; $C_0 = 1.2$; $V_{vj} = 1.53\left[g\,\sigma\,\frac{(\rho_L-\rho_V)}{(\rho_L)^2}\right]^{(\frac{1}{4})}$; (18)
Müller-Steinhagen and Heck [36]	$\left(\frac{dp}{ds}\right)^{M-S}_{2P,\,Fr} = F\,(1-x)^{\frac{1}{3}} + B\,x^3$; $F = A + 2\,x\,(B-A)$; $A = \left(\frac{dp}{ds}\right)_{L0}$; $B = \left(\frac{dp}{ds}\right)_{V0}$; (19)

2.6 Simulation results

A set of the enhanced procedures written in MATHCAD was developed for providing a simulation of a range of applications of the generalized model of the two-phase thermosyphon loop. A simulation code created for the presented experimental variant of the generalized model was used to solve

Table 3: Correlations for the local resistance of two-phase flow.

Fitting	Correlations for local resistance
Sudden contraction [37]	$\Delta p_{2P,\,CON} = \Psi^{2P}_{L0,\,CON} \times \left\{ \frac{(\dot{G}_1)^2}{2\,\rho_L} \times \left[\left(\frac{1}{C_C} - 1 \right)^2 + 1 - \frac{1}{(\zeta_{CON})^2} \right] \right\}$; $\zeta_{CON} = \left(\frac{A_{LARGE}}{A_{SMALL}} \right) = \left(\frac{A_1}{A_2} \right)$; $C_C = \left[\frac{1}{\left[0.639 \left(1 - \frac{1}{\zeta_{CON}} \right)^{0.5} + 1 \right]} \right]$; $\Psi^{2P}_{L0,\,CON} = \left[1 + x_{in} \left(\frac{\rho_L}{\rho_V} - 1 \right) \right]$; (20)
Bend [38,39]	$\Delta p_{2P,\,BEND} = \Psi^{2P}_{L0,\,BEND} \times \Delta p_{L0,\,BEND} = \Psi^{2P}_{L0,\,BEND} \times \left[K_{L0,\,BEND} \frac{(\dot{G}_1)^2}{2\,\rho_L} \right]$ $K_{L0,\,BEND} = 1.14$; $B_{90} = 1 + \frac{2.2}{k^{90}_{L0}\,[2 + (\frac{R}{D})]}$; $\Psi^{2P}_{L0,\,BEND} = \left\{ 1 + \left[\left(\frac{\rho_L}{\rho_V} - 1 \right) \times \left[B_{90}\, x_{in}\, (1 - x_{in}) + (x_{in})^2 \right] \right] \right\}$; (21)

the conservation equations of mass, momentum, and energy taking into account the measurement conditions in the experiment.

Further the effective procedures developed in this study were used to determine as follows:

- the characteristic geometrical points on the loop s_n;
- the void fraction of two-phase fluid in heater with conventional tubes and adiabatic section using the Zuber-Findlay [35] correlation and cooler with minichannel using the El-Hajal *et al.* [33] correlation;
- the local friction coefficient of two-phase flow in the selected circulation sections $\langle s_3; s_4 \rangle$ and $\langle s_4; s_7 \rangle$ of the thermosyphon loop using the Müller-Steinhagen and Heck [36] correlation for conventional tubes, the Tran *et al.* [34] correlation for minichannel $\langle s_7; s_8 \rangle$;
- the local flow resistance at characteristic points of the loop for a single- and two-phase flow in conventional diameter channel and minichannels.

Moreover, the code includes the iterative procedures for determination of the value of individual components of the of the momentum equation (16), e.g., the buoyancy term, local resistance and friction force of a single- and two-phase fluid flow in adiabatic and diabatic sections of the thermosyphon loop.

The results achieved by the use of the advanced analytical methods

and numerical calculations are the predicted distribution of values for the volumetric flow rate due to the thermal power supplied to the heater. These calculations were performed assuming the same experimental conditions. Additionally, the comparisons are made between the results of homogeneous and separate flow models of two-phase flow formulation.

3 Experimental investigations

3.1 Experimental setup

The experiments described in this paper were undertaken using the experimental setup presented in Fig. 6. Photo of the experimental setup is shown in Fig. 7. This experimental setup was prepared for performing the validation of the generalized model using its new variant configuration analyzed in this study. The measurements were carried out on a two-phase thermosyphon loop with minichannels and conventional tubes. The termosyphon loop consists of an evaporator (single-conventional tube) on the lower vertical section and a condenser (single-minichannel tube) on the upper vertical section. Experimental apparatus consists of a thermosyphon loop device including evaporator, condenser, vertical tubes (riser and downcomer), horizontal connecting tubes, expansion tank and a set of instruments such as ultrasonic flow meter, power supply, ultra-thermostat, temperature acquisition instruments data acquisition system personal computer. The test loop of rectangular shape is 700 mm high and 300 mm width. The other geometrical dimensions of the loop are shown in Fig. 5.

The evaporator consisting of one conventional channel is located on the lower left part of the vertical section of the loop. The heater is made of a silver (AG935) tube of 200 mm length and 6.2 mm internal diameter. Silver has the best thermal conductivity of 429 W/mK. The silver tube of a heater is connected to a high-current electric circuit for a heating power supplier with autotransformer M10-522 and a high current shunt. The heating tube generates heat due to Joule heat. The amount of heat generated is regulated by the use of the variable M10-522 autotransformer. The voltage and current were measured by the AX8450 digital multimeters with the AC voltage measuring accuracy of $\pm 0.5\%$.

The cooler consisting of a minichannel is located on the upper right part of the vertical section of the loop. The cooler is designed as a type of tube-in-tube heat exchanger. The inner tube of the cooler is made of a silver tube of 200 mm length and 2.4 mm internal diameter. The outer tube of

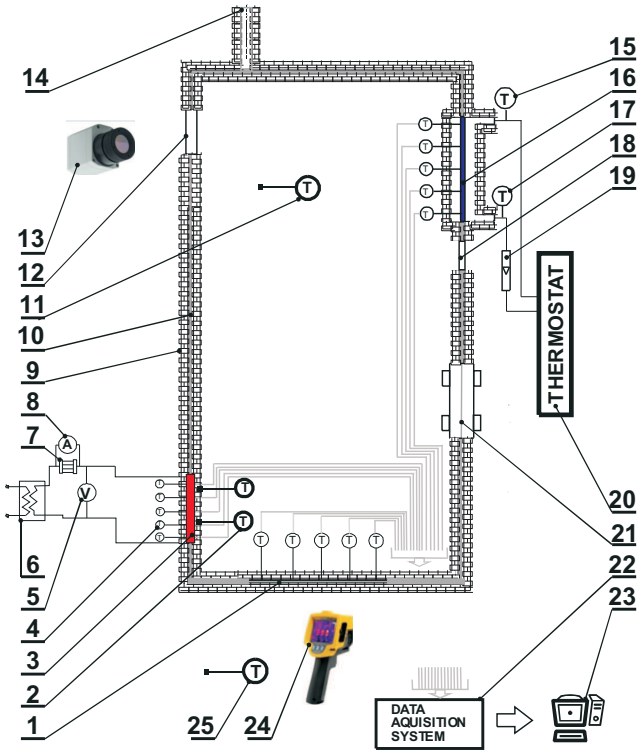

Figure 6: Schematic view of the experimental setup; 1 – minichannel, 2 – thermocouple (outer surface of insulation material), 3 – heater (conventional tube), 4 – thermocouple (outer surface of heater tube), 5 – voltmeter digital multimeter, 6 – autotransformer, 7 – high current shunt, 8 – ampmeter digital multimeter, 9 – insulation, 10 – loop pipe, 11 – thermocouple (inside box), 12 – sight glass (left), 13 – camera, 14 – expansion tank, 15 – thermocouple (outlet of cooler), 16 – minichannel cooler tube, 17 – thermocouple (inlet of cooler), 18 – sight glass (right), 19 – rotameter, 20 – ultrathermostat, 21 – ultrasonic flow meter, 22 – data acquisition system, 23 – personal computer, 24 – infrared camera, 25 – thermocouple (ambient temperature).

the cooler is transparent and made of a plexiglass with an internal diameter of 40 mm. The cooling fluid in the cooler flows in a countercurrent. The flow of coolant (distilled water) was forced by a pump ultra-thermostat MX07R-20-A12E PolyScience Refrigerated/Heated Circulating Bath with temperature stability of ± 0.07 °C. The pump flow rate was 11.9 l/min.

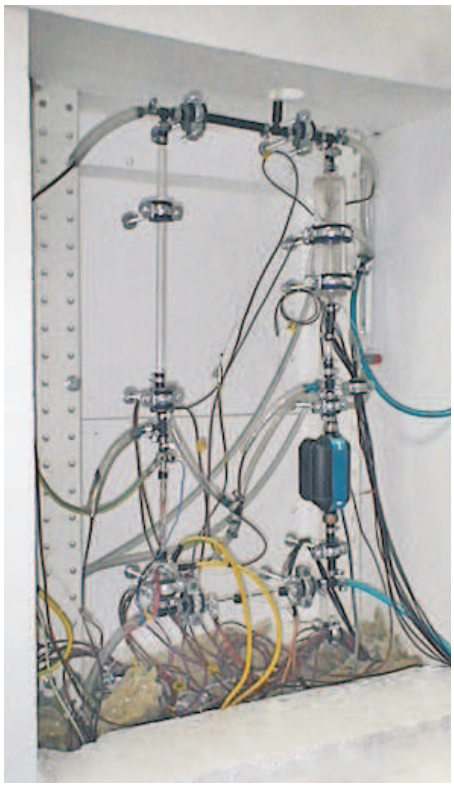

Figure 7: Photography of the experimental setup.

The flow rate for cooling fluid were adjusted by YOKOGAWA Rotameter RAGL53 with a high degree accuracy readings of ±2.5%. The T type thermocouples with 0.5 mm diameter and a measurement accuracy of ±0.5 °C were used for temperature measurements. The thermocouples measured the temperature of the cooling fluid at the inlet and outlet of the condenser.

The test loop is thermally insulated using a high-temperature insulation material made of the ceramic mineral wool insulation blankets faced outwards with aluminum foil. The thickness and thermal conductivity of the insulation material are 30 mm and $\lambda = 0.034$ W/mK, respectively. The thermocouples measured the temperature of the outer surface of the insulated evaporator. The measurement setup is also thermally isulated in order to minimize the heat losses from the setup into the ambient. The whole measurement setup is covered by large solid box made of styrofoam

with a thickness of 70 mm and a thermal conductivity of $\lambda = 0.034$ W/mK. The heat losses were determined using thermocouples located on the inner and outer walls of the insulated box. Moreover, the quality of insulation was controlled and monitored using FLIR A325sc infrared camera. It was found that the heat losses to the environment were negligible. The noncontact temperature measurements were curried out with accuracy of ± 2.0 °C and $\pm 2.0\%$ of reading. The thermal fluid flow was photographed and filmed through the sight glass of the loop tube with aid of the video camera JVC GC PX100BU.

An ultrasonic flow meter type Titan-Atrato AT710 was attached to the loop and connected directly to the data acquisition system (Model OMEGA USB-DAQ-2416-4AO). The calibrated flow meter was used for measuring and monitoring the volumetric flow rate of the circulating working fluid. This noninvasive flow meter detects changes in the flow of liquid through the small-bore tube and measures a small velocity of a fluid. The Titan-Atrato AT710 ultrasonic flow meter uses the time-of-flight measuring method. The important features of the Atrato ultrasonic flow meter are as follows: the operating capability up to 110 °C, a high measurement dynamics (200:1 turndown and remote inputs), the measurement accuracy of $< \pm 1.5\%$, and the excellent measuring repeatability of 0.1%.

The data acquisition system type and the expansion module AI-EXP-32 with a resolution of 24 bit were used for recording the measured voltage from the thermocouples, flow meter and digital multimeter. The experimental loop has a small thermal expansion tank which was opened to the atmosphere. An ultrapure water as a working fluid was used in the experimental thermosyphon loop. The water was distilled, degassed, deionized and demineralized using Milli-Q Ultrapure Water Solutions Type 1.

The experimental test setup was configured for the presented variant. In fact, the experimental setup is designed and constructed for investigating the performance of any variants of the generalized model developed for the two-phase thermosyphon loop. This test station can be used to investigate the single- and two-phase flow circulation using different types of heat exchangers: minichannels, conventional tubes and a combination of minichannels and conventional tubes. It can be also applied for testing the thermosyphon effect in loop heat pipe. The presented model of the thermosyphon loop provides a basis for further experimental investigations and other parameters validation.

3.2 Experimental procedures

First, after filling the thermosyphon with ultrapure water, the device was left out for approximately 24 hours in order to release possible bubbles in the loop. Then, the temperature of the cooling water was determined in the operating thermostat MX07R-20-A12E. The flow rate for cooling water was adjusted by Yokogawa Rotameter RAGL53.

Next, the recording device OMEGA USB-DAQ-2416-4AO, expansion module AI-EXP-32 and computer software for data logging were launched. The heating system was started up. The amount of generated heat was regulated by the variable output voltage of M10-522 autotransformer.

Finally, the measured data of volumetric flow rate and the temperature of all used thermocouples were recorded during transient and steady-state flow. The averaged value of volumetric flow rate was determined when the measured distribution of volumetric flow rate at steady-state reached a plateau. This procedure was repeated at successively higher values of heat power between 14 W–38 W. The upper limit of the heat power was not exceeded to avoid the occurrence of the dry-out phenomenon and destruction of the silver tube heater due to overheating. A large number of the volumetric flow rate measurements were made throughout this work. The obtained results were replicable.

3.3 Uncertainty analysis

The experimental errors were determined according to the ISO GUM [40] uncertainty methods of type A and B. The experimental measurements were influenced by the statistical, standard deviations (type A) and the nonstatistical, expected uncertainty of the measuring system (type B).

An estimation of the square of the overall combined uncertainty is achieved by summing the squares of the type A and B uncertainties:

$$u_C(y) = \sqrt{u_A^2(y) + u_B^2(y)}\,, \tag{22}$$

where $u_A(y)$ is the uncertainty of type A

$$u_A(y) = \sqrt{\frac{1}{N(N-1)}\sum_{i=1}^{N}(x_i - \bar{x})^2}\;;\;\text{ and }\;\bar{x} = \sqrt{\frac{1}{N}\sum_{i=1}^{N}x_i}\,, \tag{23}$$

where x_i is the ith individual value, and N is the number of observations. The expected uncertainty of the measuring system (type B) was based on

the principle of uncertainties propagation. The uncertainty of a function f of several independent variables x_i provided all errors associated with these independent variables and is given by formula

$$u_B(y) = \sqrt{\left[\sum_{i=1}^{N}\left(\frac{\partial f}{\partial x_i}\right) u(x_i)\right]^2}\,, \tag{24}$$

where $y = f(x_1, x_2, ..., x_N)$ and $u(x_i)$ is the uncertainty of variable x_i. The expanded uncertainty of measurement U was obtained by multiplying the standard uncertainty $u_C(y)$ by a coverage factor k as follows:

$$U(y) = k\, u_C(y)\ . \tag{25}$$

The standard coverage factor was used. The assigned expanded uncertainty corresponds to a coverage probability of approximately 95%.

The uncertainties in the experimental results were associated with direct measurements. Table 4 presents the uncertainty values of instruments used in the present work.

Table 4: Uncertainty of instruments used in this research.

Parameter	Instrument	Uncertainty
Voltage U [V]	Multimeter AX8450	± 0.6
Current I [A]	Multimeter AX8450	± 0.002
Volumetric flow rate	Atrato AT710	< ± 1.5 % of reading
Temperature [°C]	thermocouples type T/0.5	±0.5

The heating power input $\dot{Q}$ can be computed by Eq. (26) as follows:

$$\dot{Q} = U\, I\,, \tag{26}$$

where I is the current, U is the voltage. The uncertainty of the heating power input $\dot{Q}$ was obtained by the following equation:

$$u_B\left(\dot{Q}\right) = \sqrt{\left[\left(\frac{\partial \dot{Q}}{\partial U}\right) u_B(U)\right]^2 + \left[\left(\frac{\partial \dot{Q}}{\partial I}\right) u_B(I)\right]^2}\,. \tag{27}$$

The expanded uncertainty for the volumetric flow rate and the heat power in the evaporator were determined as $U(\dot{V}) = \pm 0.17$ mL/min and $U(\dot{Q}) = \pm 1$ W, respectively.

4 Experimental results

Figure 8 presents the experimental results for five measuring series of the volumetric flow. The results were obtained for five values of heat power (19 W, 22 W, 26 W, 31 W, 35 W) in one experimental session. The applied heating loads were set without interrupting fluid circulation. Thus, the separate series of measurements in terms of heat power can be analyzed.

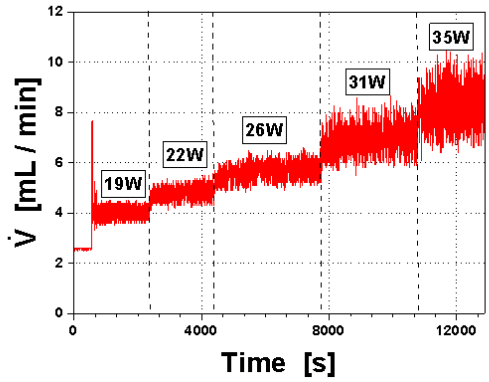

Figure 8: Experimental volumetric flow rates vs. time of recording for tested range of hear power.

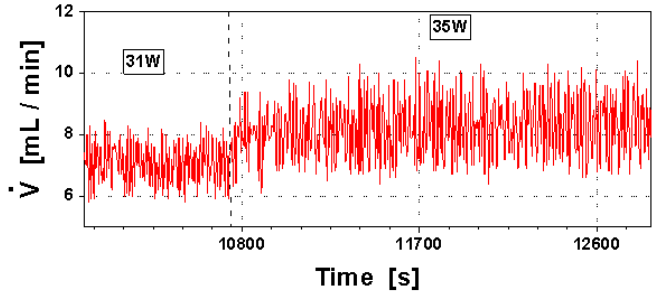

Figure 9: Measured volumetric flow rates vs. time of recording for two values of heating loads (31 W, 35 W).

Figure 9 shows the measured volumetric flow rate for the cases of applied power equal to 31 W and 35 W heating loads with zooming the time scale. The transient and steady-state sectors are clearly seen.

The oscillations in frequency and amplitude of the volumetric flow rate were observed across the full measurement range of the heating load. The relatively small amplitude values of the volumetric flow rate were observed by lower settings of the heat rate (19 W, 22 W, 26 W) applied to the evaporator of the thermosyphon loop. The relatively larger amplitude of the volumetric flow rate was observed with the increasing the heating loads (31 W, 35 W). The average value of volumetric flow rate were calculated individually for each series of measurements. The calculations were based on the instantaneous values of volumetric flow rate measured by the ultrasonic flow meter. It was found that during power start-up for each series of measurements the average value of the volumetric flow rate was increasing with time. But after this initial transient flow the average value of the volumetric flow rate reached a plateau. The values of the volumetric flow rate remain constant under steady-state conditions. Both transient and steady-state flows can be identified by each series of measurements. In fact, the steady-state played a dominant role during the measurements of the volumetric flow rate of the two-phase flow in the thermosyphon loop. Furthermore, it was observed that there is a large instantaneous value of the volumetric flow rate at low power start-up (19 W). The phenomenon of very high amplitude oscillation of flow rate was also observed and reported by Archana *et. al* [14] and Vijayan *et al.* [16]. The authors concluded that the high peak of amplitude occurs in the first unstable zone.

Results obtained for a set of the average values of the volumetric flow rate at the steady-state for all series of experimental data are presented in Fig. 10. Additionally, figure demonstrates the comparison between the results of homogeneous and separated two-phase flow models.

The experimental values of the volumetric flow rate and those obtained with the generalized model of two phase flow in thermosyphon loop using in calculations the homogenous and separated two-phase flow models are of the same order of magnitude. A good agreement can be seen by comparing the experimental values of the volumetric flow rate to the theoretical values using the separated two-phase flow model.

Moreover, the thermal behavior of the two-phase flow was photographed and filmed through the sight glass of the loop tube. Figure 11 presents photos of the two-phase flow structure observed after the fluid left the heater. In Figs. 11 (a) and (b) are shown the bubble flow at 19 W and 22 W, respectively. But the plug flow pattern was observed at 31 W.

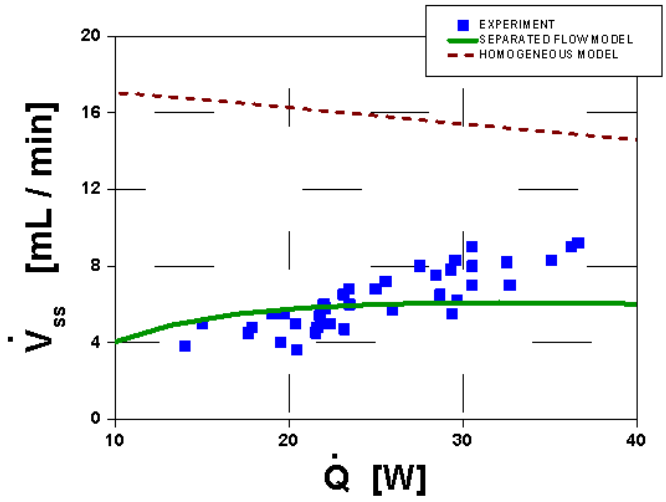

Figure 10: Comparison of the experimental average volumetric flow rate and values predicted by the homogeneous and separated two-phase flow model formulations.

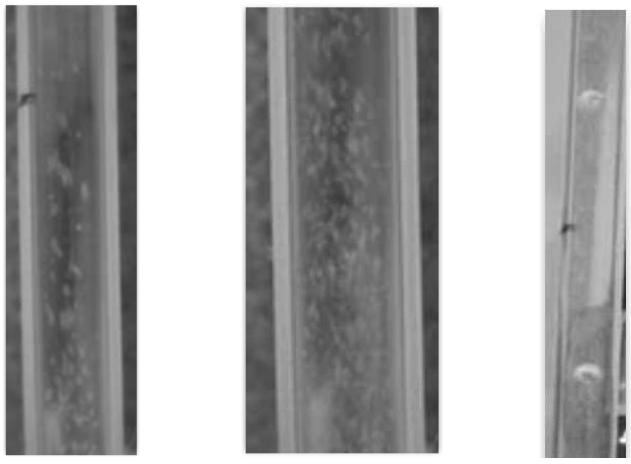

Figure 11: The flow boiling patterns observed through the evaporator transparent wall: (a) and (b) – bubble flow at 19 W and 22 W, respectively; (c) – plug flow at 31 W.

5 Conclusions

Both theoretical and experimental investigations have been carried out to study the heat transfer and fluid flow in two-phase thermosyphon loop with minichannels and conventional tubes. The goal of this research was to provide an experimental validation of the generalized theoretical model of the two-phase thermosyphon loop. A new variant of the generalized model was investigated for the purpose of improving agreement with experimental data. The model refers to a thermosyphon loop with minichannels and conventional tubes. The thermosyphon loop consists of the evaporator on the lower vertical section and the condenser on the upper vertical section. The presented thermosyphon loop configuration with the evaporator (single-conventional tube) and condenser (single-minichannel tube) was not experimentally investigated by other researchers.

The heat transfer characteristics of the thermosyphon loop with minichannels and conventional tubes based on the one-dimensional two-phase separated flow model can be predicted using the following correlations: in case of minichannels – the El-Hajal [33] correlation for void fraction, the Tran [34] correlation for the friction pressure drop of two-phase flow in the cooling region; in the case of conventional tubes – the standard Zuber-Findlay [35] drift flux model of two-phase flow correlation for void fraction, the Müller-Steinhagen and Heck [36] correlation for the friction pressure drop in two-phase flow for $\langle s_3; s_4 \rangle$ the heating region, and for $\langle s_4; s_7 \rangle$ the adiabatic region.

The oscillations in frequency and amplitude of the volumetric flow rate were observed across the full measurement range of the heating load. It was found that after this initial transient flow the average value of the volumetric flow rate reached a plateau. The values of the volumetric flow rate remain constant under steady-state conditions. The steady-state conditions played a dominant role during the two-phase flow in thermosyphon loop. The flow rate oscillations in two-phase thermosyphon loops and the constant value of the volumetric and mass flow rate under steady-state conditions were also identified and reported by Archana *et al.* [14], Vijayan *et al.* [16], Lemos *et al.* [15].

It is found that the values of the volumetric flow rate obtained experimentally and those obtained with the generalized model of two-phase flow in thermosyphon loop using in calculations the homogenous and separated two-phase flow models are of the same order of magnitude. A good agreement is observed between the experimental results and the theoretical

predictions using the separated two-phase flow model. The values of volumetric flow rate derived from the homogenous model of two-phase flow are higher than those obtained by experiment. This means that the homogeneous model of two-phase flow is too rough and does not reflect the nature of the circulation of fluid in the two-phase thermosyphon loop.

The presented results provide the experimental evidence for the validity of the proposed concept of the generalized model of two-phase thermosyphon loop. The results from the study show that this generalized model can be used to describe any possible individual variants of thermosyphon loop with minichannels including the earlier variants developed by authors [2, 8-12]. The best choice of the variant is dependent on specific conditions of cooling needs.

The presented experimental setup offers various technical solutions which provide a basis for further experimental investigations and other parameters validation. Further studies are required, for example, to verify the other variants of the generalized model previously analyzed by author and to gain knowledge about the effect of a working fluid and the geometrical parameters on the thermal performance of the thermosyphon loop. These parameters are important and practical for electronic cooling applications. The results obtained from the generalized model of two-phase thermosyphon loop can form the basis for further investigations.

Acknowledgement The work presented in the paper was funded from the National Science Centre Poland: project No: NCN-UMO-2011/01/B/ST8/06856.

Received 22 November 2016

References

[1] Agostini F., Gradinger T., Cottet D.: *Compact gravity driven and capillary-sized thermosyphon loop for power electronics cooling.* J. Thermal Sci. Eng. Appl. **6**(2014), 3, 031003-1.

[2] Bieliński H., Mikielewicz J.: *Computer cooling using a two phase minichannel thermosyphon loop heated from horizontal and vertical sides and cooled from vertical side.* Arch. Thermodyn. **31**(2010), 4, (2010), 51–59.

[3] Khodabandeh R.: *Heat transfer in the evaporator of an advanced two-phase thermosyphon loop.* Int. J. Refrig. **28**(2005), 2, 190–202.

[4] Khodabandeh R.: *Pressure drop in riser and evaporator in an advanced two-phase thermosyphon loop.* Int. J. Refrig. **28**(2005), 725–734.

[5] Kumar K.K., Gopal M.R.: *Experimental studies on CO2 based single and two-phase natural circulation loops*. Appl. Therm. Eng. **31**(2011), 16, 3437–3443.

[6] Bieliński H., Mikielewicz J.: *Natural convection of thermal diode*. Arch. Thermodyn.**16**(1995), 3-4, 177–196.

[7] Bieliński H., Mikielewicz J.: *New solutions of thermal diode with natural laminar circulation*. Arch. Thermodyn. **22**(2001), 1-2, 89–106.

[8] Bieliński H., Mikielewicz J.: *The effect of geometrical parameters on the mass flux in a two phase thermosyphon loop heated from one side*. Arch. Thermodyn. **29**(2004), 1, 59–68.

[9] Bieliński H., Mikielewicz J.: *A two phase thermosyphon loop with minichannels heated from vertical side and cooled from horizontal side*. Chem. Process Eng. **31**(2010), 4, 535–551.

[10] Bieliński H., Mikielewicz J.: *Natural circulation in single and two phase thermosyphon loop with conventional tubes and minichannels*. In: 'Heat Transfer. Mathematical Modeling, Numerical Methods and Information Technology' (A. Belmiloudi, Ed.), InTech , 2011, 475–496.

[11] Bieliński H.: *New variants to theoretical investigations of thermosyphon loop*. In: 'Two Phase Flow, Phase Change And Numerical Modeling' (A. Ahsan, Ed.) InTech (ISBN 978-953-307-584-6), Chap. 16, 2011, 365–386.

[12] Bieliński H., Mikielewicz J., Mikielewicz, D.: *A closed loop thermosyphon with conventional or minichannel based condenser and evaporator*. 16th Int. Heat Pipe Conf. (16th IHPC), Lyon, May 20-24, (2012).

[13] Lamaison N., Ong C.L., Marcinichen J.B., Thome J.R.: *Two-phase mini-thermosyphon electronics cooling: Dynamic modeling, experimental validation and application to 2U servers*. Appl. Therm. Eng. **110**(2017), 481–494.

[14] Archana V., Vaidya A.M., Vijayan P.K.: *Flow transients in supercritical CO_2 natural circulation loop*. Procedia Eng. **127**(2015). 1189–1196.

[15] Lemos W.L., Faccini H.L.H., Sul J.: *Flow Visualization Of Bubble Behavior Under Two-Phase Natural Circulation Flow Conditions Using High Speed Digital Camera*. 2013 Int. Nuclear Atlantic Conf. – INAC 2013, Recife, PE, November 24–29, 2013, Associao Brasileira De Energia Nuclear – ABEN.

[16] Vijayan P.K., Nayak A. K., Saha D., and Gartia M.R.: *Effect of loop diameter on the steady state and stability behaviour of single-phase and two-phase natural circulation loops*. Hindawi Publ. Corp. Sci. Technol. of Nuclear Installations, 2008, ID 672704, 17.

[17] Garrity P.T., Klausner J.F., Mei R.: *Instability phenomena in a two-phase microchannel thermosyphon*. Int. J. Heat Mass Tran. **52**(2009), 7–8, 1701–1708.

[18] Franco A., Filippeschi S.: *Closed loop two-phase thermosyphon of small dimensions: A Review of the experimental results*. Microgravity Sci. Tec. **24**(2012), 3, 165–179.

[19] Franco A., Filippeschi S.: *Experimental analysis of closed loop two phase thermosyphon (CLTPT) for energy systems*. Exp. Therm. Fluid Sci. **51**(2013), 302–311.

[20] Chen L., Deng Bi-Li, Zhang Xin-Rong: *Experimental study of trans-critical and supercritical CO2 natural circulation flow in a closed loop.* Appl. Thermal Eng. **59**(2013), 1–2, 1–13.

[21] Dobson R.T., Ruppersberg J.C.: *Flow and heat transfer in a closed loop thermosyphon. Part I –Theoretical simulation.* J.Energ. South. Africa **18**(2007), 4, 32–40.

[22] Dobson R.T., Ruppersberg J.C.: *Flow and heat transfer in a closed loop thermosyphon Part II – experimental simulation.* J. Energ. South. Africa **18**(2007), 3, 41–48.

[23] Agostini F., Ferreira E.: *Non intrusive measurement of the mass flow rate inside a closed loop two-phase thermosyphon.* In: Proc. 8th Minsk Int. Seminar 'Heat Pipes, Heat Pumps, Refrigerators, Power Sources', Minsk, Belarus, Sept. 12–15, 2011.

[24] Cieśliński J.T., Fiuk A.: *Heat transfer characteristics of a two-phase thermosyphon heat exchanger.* Appl. Thermal Eng. **51**(2013), 1–2, 112–118.

[25] Cieśliński J.T.: *Effect of nanofluid concentration on two-phase thermosyphon heat exchanger performance.* Arch. Thermodyn. **37**(2016), 2, 23–40, DOI: 10.1515/aoter-2016-0011.

[26] Madejski J., Mikielewicz J.: *Liquid fin a new device for heat transfer equipment.* Int. J. Heat Mass Tran. **14**(1971), 357–363.

[27] Won Tae Kim, Kwang Soo Kim, Young Lee: *Design of a two-phase loop thermosyphon for telecommunications system (II). Analysis and simulation.* KSME Int. J. **12**(1998), 5, 942–955.

[28] Mertol A., Greif R.: *A review of natural circulation loops.* In Natural Convection: Fundamentals and Applications (1985), 1033–1071.

[29] Mikielewicz D., Szymański P., Błauciak K., Wajs J., Mikielewicz J., Ihnatowicz E.: *The new concept of capillary forces aided evaporator for application in domestic organic Rankine cycle.* Heat Pipe Sci. Technol., Int. J. **1**(2010), 4, 359–373.

[30] Rao N.M., Sekhar Ch., Maiti B., Das P.D.: *Steady-state performance of a two-phase natural circulation loop.* Int. Commun. Heat Mass Trans. **33** (2006), 1042–1052.

[31] Hartenstine J.R., Bonner R.W., Montgomery J. R., Semenic S.: *LOOP Thermosyphon design for cooling of large area, high heat flux sources.* In: Proc. IPACK2007 ASME InterPACK '07, July 8-12, 2007, Vancouver, British Columbia, Canada, IPACK2007-33993.

[32] Ghiaasiaan S.M.: *Two-Phase Flow, Boiling and Condensation in Conventional and Miniature Systems.*Cambridge University Press, 2008, ISBN 978-0-521-88276-7.

[33] El-Hajal J., Thome J.R., Cavallini A.: *Condensation in horizontal tubes. Part 1: Two-phase flow pattern map.* Int. J. Heat Mass Tran.**46**(2003), 18, 3349–3363.

[34] Tran T.N., Chyu M.C., Wambsganss M.W., France D.M.: *Two-phase pressure drop of refrigerants during flow boiling in small channels: An experimental investigations and correlation development.* Int. J. Multiphase Flow, **26**(2000), 11, 1739–1754.

[35] Zuber N., Findlay J.A.: *Average volumetric concentration in two-phase flow systems.* J. Heat Trans. **87**(1965), 4, 453–468.

[36] Müller-Steinhagen H., Heck K.: *A simple friction pressure drop correlation for two-phase flow in pipes*. Chem. Eng. Processes **20**(1986), 6, 297–308.

[37] Hewitt G.F.: *Two-phase flow through orifices, valves, bends and other singularities*. In: Proc. 9th Lecture Series on Two-Phase Flow, Norwegian Institute of Technology, Trondheim (1984), 163.

[38] Chisholm D.: *Two-phase flow in bends*. Int. J. Multiphase Flow **6**(1979), 4, 363–367.

[39] Idelchik I.E.: *Handbook of Hydraulic Resistance*. 2nd Edn. New York: Hemisphere, 1986.

[40] ISO GUM EA-4/02 Evaluation of the Uncertainty of Measurement in Calibration., EA Laboratory Committee.

Notes for Contributors

ARCHIVES OF THERMODYNAMICS publishes original papers which have not previously appeared in other journals. The journal does not have article processing charges (APCs) nor article submission charges. The language of the papers is English. The paper should not exceed the length of 25 pages. All pages should be numbered. The plan and form of the papers should be as follows:

1. The heading should specify the title (as short as possible), author, his/her complete affiliation, town, zip code, country and e-mail. Please indicate the corresponding author. The heading should be followed by *Abstract* of maximum 15 typewritten lines and *Keywords*.
2. More important symbols used in the paper can be listed in *Nomenclature*, placed below *Abstract* and arranged in a column, e.g.:
   u – velocity, m/s
   v – specific volume, m/kg
   etc.
   The list should begin with Latin symbols in alphabetical order followed by Greek symbols also in alphabetical order and with a separate heading. Subscripts and superscripts should follow Greek symbols and should be identified with separate headings. Physical quantities should be expressed in SI units (*Système International d'Unités*).
3. All abbreviations should be spelled out first time they are introduced in the text.
4. The equations should be each in a separate line. Standard mathematical notation should be used. All symbols used in equations must be clearly defined. The numbers of equations should run consecutively, irrespective of the division of the paper into sections. The numbers should be given in round brackets on the right-hand side of the page.
5. Particular attention should be paid to the differentiation between capital and small letters. If there is a risk of confusion, the symbols should be explained (for example *small c*) in the margins. Indices of more than one level (such as B_{f_a}) should be avoided wherever possible.
6. Computer-generated figures should be produced using **bold lines and characters**. No remarks should be written directly on the figures, except numerals or letter symbols only. Figures should be as small as possible while displaying clearly all the information requires, and with all lettering readable. The relevant explanations can be given in the caption.
7. The figures, including photographs, diagrams, etc., should be numbered with Arabic numerals in the same order in which they appear in the text. Each figure should have its own caption explaining the content without reference to the text.
8. Computer files on an enclosed disc or sent by e-mail to the Editorial Office are welcome. The manuscript should be written as a MS Word file – $*.doc$, $*.docx$ or LaTeX file – $*.tex$. For revised manuscripts after peer review process, figures should be submitted as separate graphic files in either vector formats (PostScript (PS),

Encapsulated PostScript (EPS), preferable, CorelDraw (CDR), etc.) or bitmap formats (Tagged Image File Format (TIFF), Joint Photographic Experts Group (JPEG), etc.), with the resolution not lower than 300 dpi, preferably 600 dpi. These resolutions refer to images sized at dimensions comparable to those of figures in the print journal. Therefore, electronic figures should be sized to fit on single printed page and can have maximum 120 mm x 170 mm. Figures created in MS World, Exel, or PowerPoint will not be accepted. The quality of images downloaded from websites and the Internet are also not acceptable, because of their low resolution (usually only 72 dpi), inadequate for print reproduction.

9. The references for the paper should be numbered in the order in which they are called in the text. Calling the references is by giving the appropriate numbers in square brackets. The references should be listed with the following information provided: the author's surname and the initials of his/her names, the complete title of the work (in English translation) and, in addition:

   (a) for books: the publishing house and the place and year of publication, for example:
   [1] Holman J.P.: *Heat Transfer*. McGraw-Hill, New York 1968.

   (b) for journals: the name of the journal, volume (Arabic numerals in bold), year of publication (in round brackets), number and, if appropriate, numbers of relevant pages, for example:
   [2] Rizzo F.I., Shippy D.I.: *A method of solution for certain problems of transient heat conduction*. AIAA J. **8**(1970), No. 11, 2004–2009.

   For works originally published in a language other than English, the language should be indicated in parentheses at the end of the reference.

   Authors are responsible for ensuring that the information in each reference is complete and accurate.

10. As the papers are published in English, the authors who are not native speakers of English are obliged to have the paper thoroughly reviewed language-wise before submitting for publication.

Manuscript submission Manuscripts to be considered for publication should be electronically submitted to the Editorial Office via the online submission and reviewing system, the Editorial System, at http://www.editorialsystem.com/aot. Submission to the journal proceeds totally on line and you will be guided stepwise throughout the process of the creation and uploading of your files. The body of the text, tables and figures, along with captions for figures and tables should be submitted separately. The system automatically converts source files to a single PDF file article, for subsequent approval by the corresponding Author, which is then used in the peer-review process. All correspondence, including notification confirming the submission of the manuscripts to the Editorial Office, notification of the Editorsñs decision and requests for revision, takes place by e-mails. Authors should designate the corresponding author, whose responsibility is to represent the Authors in contacts with the Editorial Office. Authors are requested not to submit the manuscripts by post or e-mail.

The illustrations may be submitted in color, however they will be printed in black and white in the journal, so the grayscale contributions are preferable. Therefore, the figure

caption and the entire text of the paper should not make any reference to color in the illustration. Moreover the illustration should effectively convey author's intended meaning when it is printed as a halftone. The illustrations will be reproduced in color in the online publication.

Further information All manuscripts will undergo some editorial modification. The paper proofs (as PDF file) will be sent by e-mail to the corresponding author for acceptance, and should be returned within two weeks of receipt. Within the proofs corrections of minor and typographical errors in: author names, affiliations, articles titles, abstracts and keywords, formulas, symbols, grammatical error, details in figures, etc., are only allowed, as well as necessary small additions. The changes within the text will be accepted in case of serious errors, for example with regard to scientific accuracy, or if authors reputation and that of the journal would be affected. Submitted material will not be returned to the author, unless specifically requested.
A PDF file of published paper will be supplied free of charge to the Corresponding Author.

Submission of the manuscript expresses at the same time the authors consent to its publishing in both printed and electronic versions.

Transfer of Copyright Agreement Submission of the manuscript means that the authors automatically agree to assign the copyright to the Publisher. Once a paper has been accepted for publication, as a condition of publication, the authors are asked to send by email a scanned copy of the signed original of the Transfer of Copyright Agreement, signed by the Corresponding Author on behalf of all authors to the Managing Editor of the Journal. The copyright form can be downloaded from the journal's website at http://www.imp.gda.pl/archives-of-thermodynamics/ under Notes for Contributors.

The Editorial Committee